

Thermally stimulated currents and photoconductivity in microcrystalline silicon

Von der Fakultät für
Mathematik und Naturwissenschaften der
Carl von Ossietzky Universität Oldenburg
zur Erlangung des Grades und Titels einer
Doktorin der Naturwissenschaften (Dr. rer. nat.)
angenommene Dissertation

von
Nacéra Souffi
geboren am 25.03.1969
Oran (Algerien)

Contents

Abstract

Zusammenfassung

Abbreviation and symbols

| | | |
|----------|--|-----------|
| 1 | Introduction | 1 |
| 2 | Fundamental properties of microcrystalline silicon | 5 |
| 2.1 | Structure of microcrystalline silicon..... | 5 |
| 2.2 | Optical properties..... | 8 |
| 2.3 | Electronic properties..... | 9 |
| 3 | Samples | 13 |
| 3.1 | Deposition..... | 13 |
| 3.2 | Crystalline volume fraction..... | 13 |
| 4 | Photoconductive techniques | 15 |
| 4.1 | Dark conductivity and photoconductivity techniques (SSPC)..... | 15 |
| 4.1.1 | Sample geometry..... | 15 |
| 4.1.2 | Dark conductivity..... | 15 |
| 4.1.3 | Photoconductivity..... | 16 |
| 4.2 | Steady state photocarrier grating technique (SSPG)..... | 18 |
| 4.3 | Experimental results..... | 20 |
| 4.3.1 | Mobility lifetime product obtained at room temperature..... | 20 |
| 4.3.2 | Temperature dependence of the mobility lifetime product..... | 21 |
| 4.4 | Discussion..... | 22 |
| 5 | Thermally stimulated currents (TSC) | 23 |
| 5.1 | Principle..... | 23 |
| 5.2 | Approaches for the DOS determination from TSC..... | 26 |
| 5.2.1 | Maximum TSC emission energy..... | 26 |
| 5.2.2 | Density of states..... | 28 |
| 6 | Numerical simulation of TSC | 31 |
| 6.1 | Simulation details..... | 31 |
| 6.2 | Illustration of both strong and weak retrapping..... | 33 |
| 6.2.1 | T-independent carrier lifetime..... | 33 |
| 6.2.2 | Discussion..... | 46 |
| 6.2.3 | Band tail parameter variation..... | 51 |
| 6.2.4 | Heating rate variation..... | 54 |
| 6.2.5 | Capture coefficient variation..... | 58 |
| 6.2.6 | T-dependent carrier lifetime..... | 61 |
| 6.3 | Conclusion..... | 65 |

| | | |
|-----------|---|------------|
| 7 | Experimental and simulated results of TSC for the weak retrapping regime | 67 |
| 7.1 | TSC for sample with $R_c = 34\%$ | 67 |
| 7.1.1 | Mobility-lifetime product determination..... | 68 |
| 7.1.2 | Simulation of experimental results..... | 70 |
| 7.1.3 | Application of Landweer and Bezemer approach..... | 76 |
| 7.2 | Discussion..... | 76 |
| 7.3 | Parameter variation..... | 78 |
| 7.3.1 | Heating rate variation..... | 78 |
| 7.3.2 | Initial temperature variation..... | 84 |
| 7.3.3 | Relaxation time variation..... | 88 |
| 7.3.4 | Photogeneration rate variation..... | 89 |
| 7.4 | Conclusion..... | 92 |
| 7.5 | Improvement of Landweer and Bezemer approach..... | 93 |
| 8 | Experimental and simulated results of TSC for the strong retrapping regime | 95 |
| 8.1 | TSC for the sample with $R_c = 79\%$ | 95 |
| 8.1.1 | Density of states and simulation..... | 97 |
| 8.1.2 | Discussion..... | 101 |
| 8.2 | Parameter variation..... | 103 |
| 8.2.1 | Heating rate variation..... | 103 |
| 8.2.2 | Photogeneration rate variation..... | 104 |
| 8.3 | Conclusion..... | 105 |
| 8.4 | Experimental and simulated results for $\mu\text{-Si:H}$ with $R_c = 88\%$ | 106 |
| 8.4.1 | Discussion..... | 109 |
| 9 | Density of states from other techniques | 111 |
| 9.1 | Photoconductive techniques..... | 111 |
| 9.1.1 | SSPC..... | 111 |
| 9.1.2 | SSPG..... | 112 |
| 9.1.3 | LF-MPC..... | 113 |
| 9.2 | Experimental results..... | 113 |
| 9.2.1 | Discussion..... | 116 |
| 9.3 | Conclusion..... | 117 |
| 10 | Summary and conclusion | 119 |
| | Acknowledgements | 121 |
| | References | 123 |
| | Publications related to the Ph.D. Thesis | 127 |
| | Lebenslauf | 129 |

Abstract

The thesis presents a study of the determination of the density of states (TSC-DOS) from experimental and numerically simulated thermally stimulated currents (TSC). Taking into account recombination, thermal emission and trapping, numerical simulation has been applied in order to analyze the strong and weak retrapping regimes of TSC. It should be noted that only the contribution of electrons has been considered in the simulation. The reconstruction of the DOS distribution reveals the validity of the standard procedures to calculate the DOS in the case of weak retrapping. In the case of strong retrapping, it has been shown that the quasi Fermi level E_q is a suitable parameter to establish the energy scale of the TSC-DOS. However $E_{m,a}$, the energy at which the emission rate is at a peak, is considered as the energy scale for weak retrapping. Furthermore, the retrapping has been quantified from the determination of the effective attempt to escape frequency.

In order to show the strong and weak retrapping regimes and to determine the experimental DOS from the TSC technique, TSC and photoconductivity measurements have been carried out on microcrystalline silicon ($\mu\text{c-Si:H}$) samples.

The sample series, deposited by hot wire chemical vapour deposition (HWCVD), is characterized by different structural compositions with samples with high and low crystalline volume fraction R_c . A combined experiment - simulation approach allowed to extract the DOS profile and to deduce trap parameters. For the samples, the DOS profiles emerge with conduction band tail parameters which vary between 20 meV and 24 meV. Deeper in the gap, a broad defect distribution is obtained. The capture coefficient c_n varies between $1 \times 10^{-9} \text{ cm}^3 \text{ s}^{-1}$ and $3 \times 10^{-9} \text{ cm}^3 \text{ s}^{-1}$. With increasing R_c parameter, the DOS increases in the range $E_c - E > 0.3$ eV. However, over the range of energies between $E_c - E = 0.15$ eV and $E_c - E = 0.3$ eV, the DOS of samples with high crystallinity is lower with respect to that of the samples with low R_c .

The effect of the variation of experimental parameters on the TSC-DOS as well as on the retrapping regime of the samples has also been studied. It has been shown that the TSC-DOS distributions do not vary in the exploited experimental parameter space. This result is consistent since the TSC-DOS should not depend on the experimental parameters. In addition, the results indicate that the peak of the TSC-DOS at low energy is not a real image of the DOS. This peak corresponds to the initial rise of the TSC at low temperatures. The origin of

this peak has been examined. Indeed, it has been demonstrated that the low temperature peak of the TSC is related to the shallow states of the conduction band tail distribution, which are partly occupied.

In addition, the photoconductivity measurements at room temperature reveal a change in the mobility-lifetime product when the parameter R_c increases. The Fermi level shifts to the conduction band edge. This behaviour has been related to a change of the occupancy of defects in the gap.

Zusammenfassung

In der vorliegenden Arbeit wird die Bestimmung der Zustandsdichte (TSC-DOS) aus numerisch simulierten und experimentell bestimmten thermisch stimulierten Strömen (TSC) vorgestellt. Die numerische Simulation wurde unter Berücksichtigung von Rekombination, thermischer Emission und Trapping durchgeführt, wobei nur der Beitrag von Elektronen berücksichtigt wurde. Die rekonstruierte DOS zeigt, dass die Standardprozeduren zur DOS-Bestimmung im Falle von schwachem Retrapping gute Ergebnisse liefern. In dem Fall von starkem Retrapping wurde gezeigt, dass das quasi Fermi Niveau E_q ein verwendbarer Parameter ist, um die Energieskalierung für die TSC-DOS herzustellen. Jedoch wird $E_{m,a}$, die Energie, bei der die Emission maximal ist, als Energieskalierung für das schwache Retrapping angewendet. Das Retrapping wird quantifiziert durch die Bestimmung der sog. effektiven attempt-to-escape Frequenz.

Um TSC unter den Bedingungen von starkem oder schwachem Retrapping zu demonstrieren und die experimentelle DOS aus der TSC-Methode zu bestimmen, wurden TSC und photogenerationsabhängige Photostrommessungen an mikrokristallinem Silizium ($\mu\text{c-Si:H}$) durchgeführt.

Eine Probenserie, die durch HWCVD (*hot wire chemical vapour deposition*) hergestellt wurde, ist gekennzeichnet durch eine variable strukturelle Zusammensetzung, mit Proben hoher und niedriger kristalliner Volumenanteil R_c . Eine Kombination von Experiment und Simulation ermöglichte die Bestimmung des DOS-Profiles und der Trap-Parameter. Für diese Probenserie liegt der Parameter des Leitungsbandausläufers E_0 im Bereich zwischen 20 meV und 24 meV. Tiefer in der Bandlücke wird eine breite Defektverteilung bestimmt. Der Einfangkoeffizient liegt zwischen $1 \times 10^{-9} \text{ cm}^3 \text{ s}^{-1}$ und $3 \times 10^{-9} \text{ cm}^3 \text{ s}^{-1}$. Bei Zunahme des R_c Parameter steigt der Wert der DOS im Energiebereich $E_c - E > 0.3 \text{ eV}$ an. Wenn die Energie zwischen 0.15 eV und 0.3 eV liegt, ist die DOS von Proben niedriger mit Bezug auf die DOS von Proben mit niedrigerem R_c .

Der Effekt der Veränderung der experimentellen Parameter wurde in Bezug auf die TSC-DOS sowie auf das Retrapping Regime der Proben untersucht. Es wurde gezeigt, dass die TSC-DOS Verteilung in dem ausgenutzten experimentellen Parameterraum sich nicht ändert. Dieses Ergebnis ist konsistent, weil die TSC-DOS unabhängig von den experimentellen Parametern sein sollte. Die Ergebnisse zeigen auch, dass der Peak von der TSC-DOS bei den niedrigen Energien kein reales Bild der DOS widerspiegelt. Es wurde gezeigt, dass der TSC Anstieg zu Beginn des TSC Experiment bei niedrigen Temperaturen mit

den flachen Zuständen des Leitungsbandausläufers zusammenhängt, die nicht völlig besetzt sind.

Zusätzliche Ergebnisse aus Photoleitungsmessungen bei Raumtemperatur zeigen, dass das Lebensdauer-Beweglichkeitsprodukt sich erhöht mit zunehmendem R_c . Das Fermi Niveau verschiebt auch in Richtung Leitungsband. Dieses hängt mit einer Änderung der Besetzung von Defekten in der Bandlücke zusammen.

Abbreviations and symbols

Abbreviations

| | |
|--------------------|--------------------------------------|
| TSC | Thermally stimulated currents |
| SSPG | Steady state photocarrier grating |
| SSPC | Steady state photocurrent |
| LF-MPC | Low frequency modulated photocurrent |
| $\mu\text{c-Si:H}$ | Microcrystalline silicon |
| HWCVD | Hot wire chemical vapour deposition |

Symbols

| | |
|----------------|-----------------------------|
| σ_{TSC} | TSC conductivity |
| TSC-DOS | Density of states from TSC |
| R_c | Crystalline volume fraction |
| $(\mu\tau)$ | Mobility lifetime product |
| d | Thickness of sample |
| L_d | Diffusion length |
| W | Width between electrodes |

Chapter 1

Introduction

Over the past years, a great progress has been made in the photovoltaic field (conversion of solar light to electrical energy) [1,2]. The improvement of the solar cell efficiency strongly depends on the choice of the films with which the cells are obtained.

Technologically, the most important thin film solar cells are copper-indium-diselenide (Cu_nS_{e2}), cadmium telluride (CdTe) and hydrogenated amorphous silicon (a-Si:H). These films can be advantageously deposited on large areas and on different types of substrates. Besides, they offer a great potential for a reduction of costs. The solar cells based on the amorphous silicon film can reach a conversion efficiency about 10% [3]. However, the major disadvantage of these cells is the light induced degradation known as Staebler-Wronski effect [4].

Few years ago, the microcrystalline silicon ($\mu\text{c-Si:H}$) cells technologically emerged as new cell type with high efficiency η [5-10], while the technologic advantages cited above are maintained. Indeed, the a-Si:H has been advantageously combined with $\mu\text{c-Si:H}$ to form devices so called “micromorph”. This technology has been pioneered by the group at IMT Neuchâtel [3,6,7,8] and the group in Jülich (1994) [9]. Their first p i n solar cell has been reported by Meier *et al.* with η around 4.6% [6]. Later, $\mu\text{c-Si:H}$ cells have been achieved with higher efficiencies than those obtained from a-Si:H technology [3]. In 2004, Meier *et al.* [7] published micromorph tandem with $\eta = 10.8\%$ stable.

The $\mu\text{c-Si:H}$ material was introduced by Veprek [11,12] and nowadays generally deposited by either plasma enhanced chemical vapour (PECVD) or hot wire chemical vapour deposition (HWCVD) [9,13,14,15]. This material has attracted considerable attention because of its absorption extending into the near infrared as well as its high stability against light exposure compared to amorphous silicon [7,16,17]. However, a detailed knowledge of the interrelation between the solar cell performance and the material properties of $\mu\text{c-Si:H}$ is not yet obtained.

The $\mu\text{c-Si:H}$ film is not a single material but exhibits a wide class of heterogeneous material composed of amounts of microcrystallites, hydrogenated amorphous silicon and voids [18,19]. $\mu\text{c-Si:H}$ with highest crystalline volume fraction and largest crystallite size has

been considered to yield the best solar cell performance. This has been recently repudiated, and the best conversion efficiencies are achieved for $\mu\text{c-Si:H}$ solar cells by incorporating an intrinsic (i-) layer deposited near the $\mu\text{c-Si:H/a-Si:H}$ transition [8,18]. Approaching this transition, the crystalline volume fraction decreases and the morphology of the films becomes compact. Referring to Veprek and other authors [3,11,20,21], $\mu\text{c-Si:H}$ show n-type character just after deposition. This tendency is stronger for films with high crystalline volume fraction [9]. Some authors attribute this effect to unintentional doping provoked by the oxygen diffusion via grain boundaries [3,6,17]. However a clear evidence about the role of oxygen in the film does not yet exist [22].

Unstable and metastable effects on the electronic properties of $\mu\text{c-Si:H}$ were the subject of different investigations [23-26]. Indeed, the change of the dark conductivity has been related to the adsorbates [27-28]. However, this effect is still not clearly understood.

Because of the complicated microstructure of $\mu\text{c-Si:H}$ film, only some information is available about the density of states (DOS) of this material. In the literature, some investigations suggested the existence of a conduction band tail in order to interpret the experimental results [25,29].

For this reason a study of the DOS as function of crystalline volume fraction as well as a more detailed understanding of the retrapping regime relating the transport states to the band tail states are of great interest.

Thermally stimulated current (TSC) technique is a powerful tool which allows to probe the localized states in the energy gap. This technique has been performed on thin film insulators as well as on amorphous silicon [30,31,32] in order to determine the DOS in the gap. Recently, this technique has been successfully applied on $\mu\text{c-Si:H}$ [33,34] samples and a profile of the DOS has been extracted.

The present Ph.D. thesis provides a study on electronic properties of microcrystalline silicon by the TSC technique accompanied with complementary photoconductive measurements. The aim of this investigation is the determination of the density of states in the gap for samples with different crystalline volume fraction. The combination of the numerical simulation, where the different processes such as emission, retrapping and recombination are taken into account, allowed to show the evidence of the strong and weak retrapping regime and hence to deduce the trap parameters.

The outline of the present work is as follows:

Chapter 2: A short summary of the fundamental properties of $\mu\text{-Si:H}$ film is given. More information is given essentially for both microstructure and density of states parameter of the material.

Chapter 3: Description of the samples. The technique as well as the deposition parameters with which they were prepared are presented. In addition, the crystalline volume fractions of samples are given.

Chapter 4: A brief description of SSPC and SSPG techniques. The results of the mobility lifetime product for electrons and holes ($(\mu\tau)_{n,p}$) at room temperature are presented and then discussed. The results of the temperature-dependent $(\mu\tau)_{n,p}$ are also presented and discussed as a function of the crystalline volume fraction.

Chapter 5: The first part of this chapter deals with the description of the TSC technique. Next, the most important TSC results obtained in the literature are reviewed. The second part provides the different approaches allowing to get the DOS from TSC.

Chapter 6: This chapter focuses on the illustration of the strong and weak retrapping regimes via TSC simulation. For this reason, different DOS forms as well as trap parameters are varied.

Chapter 7: In the first part of this chapter, evidence of the weak retrapping regime, relating to the sample with low crystalline volume fraction, has been provided using a combined experiment-simulation approach. The TSC-DOS and trap parameters are determined. The second part deals with the variation of experimental parameters.

Chapter 8: In this chapter evidence of the strong retrapping regime, relating to the sample with high crystalline volume fraction is provided. The corresponding DOS as well as the trap parameters are obtained. Also in this chapter different experimental parameters are varied during the TSC measurement.

Chapter 9: The DOS from TSC and other photoconductive techniques such SSPC, SSPG and LF-MPC are presented and then discussed.

Chapter 10: The results are summarized and conclusions are drawn.

Chapter 2

Fundamental properties of microcrystalline silicon

In this chapter the most important structural and optoelectronic properties of microcrystalline silicon ($\mu\text{c-Si:H}$) are presented. In addition, some knowledges regarding the crystalline (c-Si) and amorphous (a-Si) silicon have been recalled. Some attention is attributed to both microstructure as well as DOS of the $\mu\text{c-Si:H}$ film.

2.1 Structure of microcrystalline silicon

As reported in the literature [16,35], the $\mu\text{c-Si:H}$ material is heterogeneous, described by different forms of microstructure rather than by a well defined structure. In fact such film exhibits a complicated microstructure characterized by a mixture of clusters of crystalline grains, disordered regions and voids.

The microstructure depends on the deposition conditions such as silane to hydrogen ratio, substrate type as well as its temperature during the sample deposition, deposition pressure, etc. is important. We can expect a strong influence of this structural property on the electric and optical properties of the sample. Indeed, the existence of a correlation between the optoelectronic properties and the microstructure of $\mu\text{c-Si:H}$ was the subject of several recent investigations [36-43].

A wide variety of experiments like transmission electronic microscope (TEM), X-ray diffraction (XRD) have been applied on $\mu\text{c-Si:H}$ in the aim to gain more information on the microstructure. The combination of these studies allowed to get a schematic picture of the structural composition of $\mu\text{c-Si:H}$. Fig. 2.1 illustrates the important features of the structure of $\mu\text{c-Si:H}$. From left to right, Fig. 2.1 shows a wide range of material structures grown on glass and ranging from high crystalline volume fraction (left) to almost complete amorphous structure (right). The first step of the growth is the incubation region which is strongly related to the deposition conditions and the substrate type.

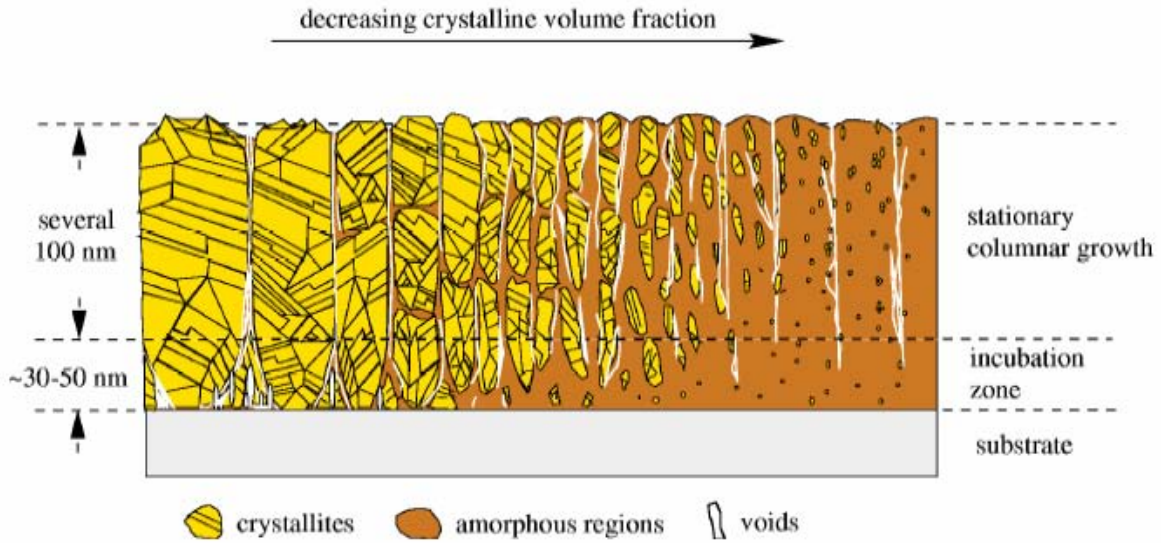


Figure 2.1: Schematic diagram showing the structure of $\mu\text{c-Si:H}$. From left to right the film composition changes from highly crystalline to predominant amorphous. The picture was taken from Finger [35].

With increasing film thickness the diameter of columnar structures, especially in the highly crystalline regime, increases leading to a conical shape as has been shown in incubation zone in Fig. 2.1. In this regime, the structure of columnar clusters (columns), having a diameter of up to 200 nm, is dominant. These columns are separated from each other by crack-like voids and disordered material. In the presence of such crack-like voids, impurities or atmospheric gas can easily diffuse along the columns boundaries. Indeed, a high concentration of oxygen has been detected from infrared spectroscopy [3,17]. In particular the material grown at high hydrogen dilution and hence characterised with high crystalline volume fraction shows a pronounced porosity.

In addition, the structure inside the columns is not monocrystalline. In fact, the columnar clusters are composed of coherent regions called “grains” whose diameter is considerably small (~ 30 nm). These regions are separated from each other by stacking fault and twin boundaries. However, these coherent regions (grains) present translation symmetry [19].

With decreasing crystalline volume fraction (see Fig. 2.1), the amorphous contribution increases. The columnar crystalline structure is interrupted and small coherent “grains” are embedded in the amorphous matrix. Such material corresponds to a transition between microcrystalline silicon and amorphous.

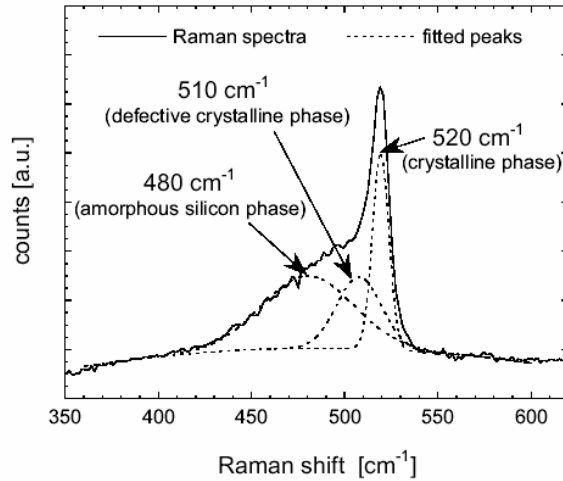


Figure 2.2: Typical Raman spectra of $\mu\text{c-Si:H}$ film [44]. The 3 different phases coexist together.

Raman spectroscopy

The information regarding the structural properties of the sample could be obtained via the Raman scattering measurements. It has already reviewed that the microstructure of $\mu\text{c-Si:H}$ sample is a mixture of crystalline silicon (c-Si), amorphous and disorder (a-Si). That means we can expect to obtain for this material similar modes to those found in (c-Si) or (a-Si). Indeed, the Fig. 2.2, showing a deconvolution of Raman spectra determined from $\mu\text{c-Si:H}$ sample, reveals 3 peaks: around 520 cm^{-1} (crystalline phase), around 510 cm^{-1} (defective crystalline phase) and around 480 cm^{-1} (amorphous silicon phase) [45,46]. The above deconvolution allows us to get the integrated Raman intensities I_c (crystalline contribution) and I_a (amorphous contribution) and then the ratio R_c defined as $R_c = I_c / (I_c + I_a)$ [47].

The Raman intensity, in the film during the matter-light interaction, decreases exponentially. This decrease is not only due to the attenuation of the excitation light but also to the attenuation of the Raman scattered light. Since the penetration depth is defined as the depth where intensity is attenuated of $1/e \approx 37\%$ of the excitation light, the Raman collection depth is equal to $1/(2\alpha)$ (α is the absorption coefficient).

The Raman collection depth, with the same excitation, differs. Bifacial depth-dependent Raman measurements (on the top side (layer side) and on the bottom (glass-side)) show that these films are inhomogeneous [44]. Raman measurements do not consider the whole volume of the sample; therefore it is difficult to attribute R_c to the real crystalline volume fraction. That means we have to keep in mind that R_c only describes a trend of the crystalline evolution in $\mu\text{c-Si:H}$ films. Thus, R_c is considered as a semi-quantitative value of the crystalline volume fraction [47].

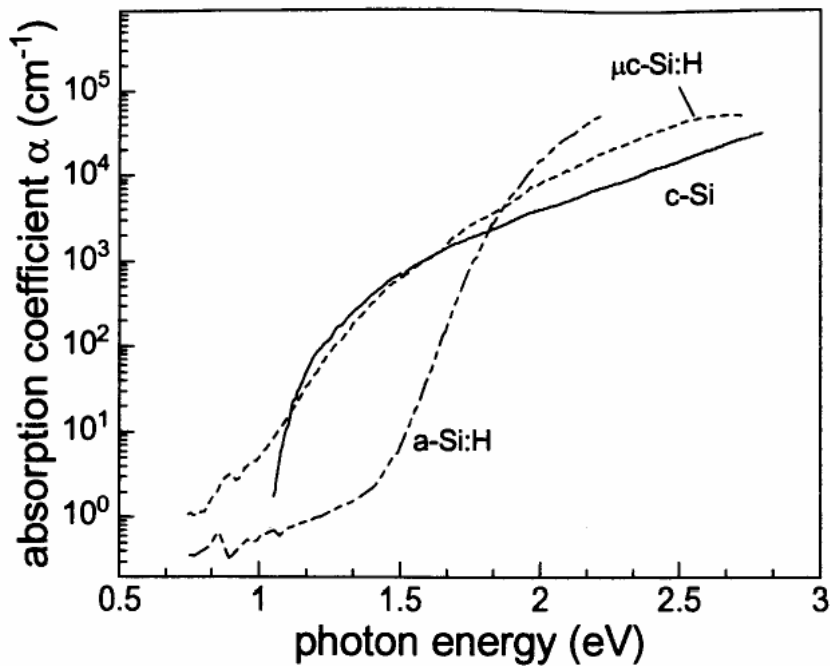


Figure 2.3: Absorption coefficient α determined for crystalline silicon (c-Si), hydrogenated amorphous silicon (a-Si:H) and microcrystalline silicon (μ c-Si:H) measured by photothermal deflection spectroscopy. The figure is taken from reference [48].

2.2 Optical properties

The absorption coefficient α is an important optical parameter which characterizes the film. Fig. 2.3 compares α measured for μ c-Si:H, a-Si:H and c-Si [48]. α has been evaluated from photothermal deflection spectroscopy (PDS) [49]. In the region where the photon energy is larger than 1.4 eV, the μ c-Si:H sample has an α -profile higher than that of c-Si. This increase has been related to the presence of a disordered phase in μ c-Si:H [50]. The α increase has also been attributed to the hydrogen content in the grain boundaries [51]. Between 1.4 eV and 1.1 eV, $\alpha(\mu$ c-Si:H) < α (c-Si). In addition, below 1.1 eV the α values of μ c-Si:H are higher than those of a-Si:H. Similar observation has been reported on polycrystalline and amorphous silicon. This behaviour has been assigned to the presence of dangling bonds [52].

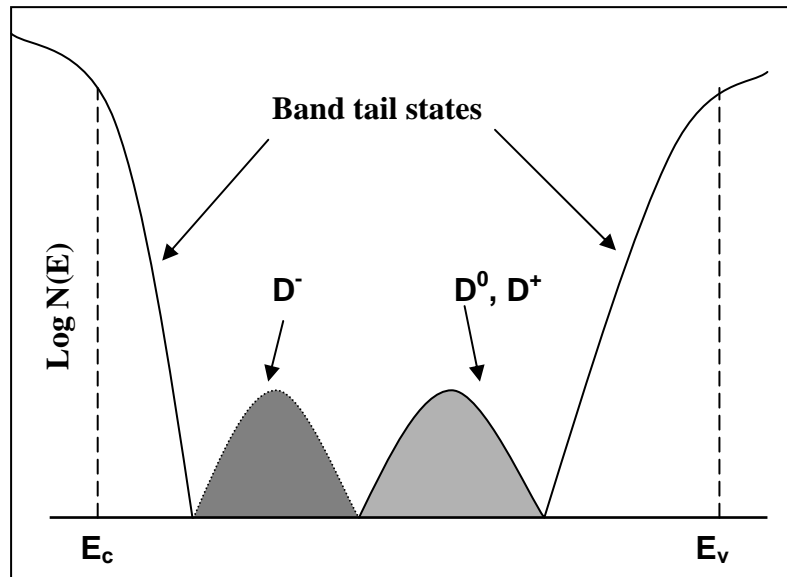


Figure 2.4: Schematic density of states diagram for a-Si:H against the energy according to [53]. Shallow (band tail states) and deep localised states (dangling bonds: D^0 , D^+ and D^-) are shown. E_c and E_v represent the mobilities edges of conduction and valence band respectively.

2.3 Electronic properties

As has been reported in section 2.2, the microstructure of $\mu\text{c-Si:H}$ is a mixture of microcrystalline phase, amorphous phase and grain boundaries. Therefore, a question arises: which part of the material controls electronic transport, and what is the impact of the $\mu\text{c-Si:H}$ microstructure on the electronic states of the material. We first recall some properties regarding hydrogenated amorphous silicon (a-Si:H) and then we start the discussion of microcrystalline silicon.

Amorphous silicon

In amorphous silicon the long range disorder is due to the local fluctuations in the interatomic distances as well as the bonding angles. The translation symmetry is broken. The energy bands are no longer described by the $E-k$ dispersion relation, but rather by a density of states $N(E)$. Figure 2.4 illustrates a diagram of the density of states $N(E)$ for a-Si:H. In the figure, E_c (or E_v) represents the energy of the mobility edge which separates localized and extended states.

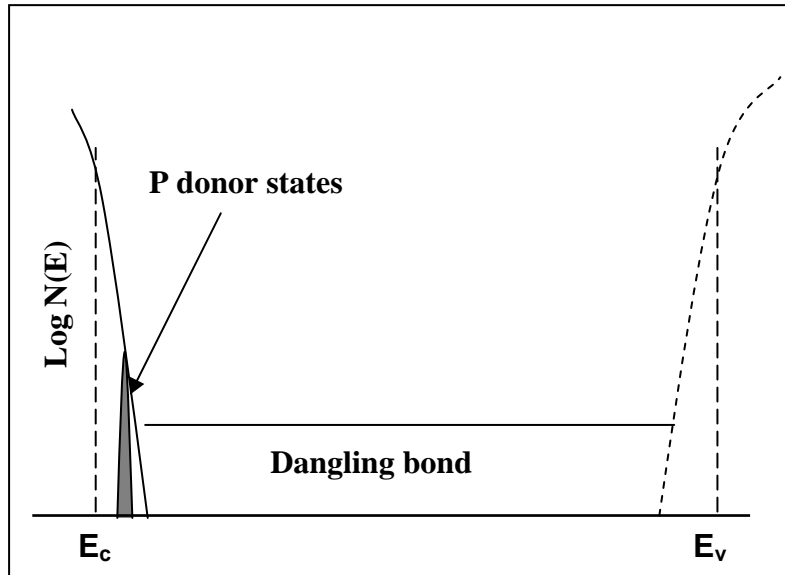


Figure 2.5: Schematic density of states diagram for P-doped microcrystalline silicon against the energy. Shallow localised states describe steep conduction and valence band tails respectively. The figure is taken from [29].

The abrupt band edges of a crystal are replaced by a broadened tail of states extending into the forbidden gap. The presence of band-tail localized states has been attributed to the disorder [54].

The conduction and valence band tail parameter deduced from the exponential form of the density of states for an optimised “standard” a-Si:H are 25 meV and 50 meV. Unsaturated silicon bonds, also known as dangling bonds, create defect states within the gap. Dangling bonds can exist in 3 different charge states D^0 , D^+ and D^- [53].

Microcrystalline silicon

The microstructure of this material strongly influences the electronic properties. Indeed materials with high crystalline fraction are characterized by a poor column boundary passivation caused by hydrogen etching or the thermal desorption of hydrogen [55]. A high spin density from electron spin resonance (ESR) measurements is shown for these materials [55]. In contrast, the spin density is lower for material grown at low hydrogen dilution and which yields a low crystalline volume fraction. These materials are prepared near the transition $\mu\text{c-Si:H/a-Si:H}$ and are characterized by a compact morphology.

Because of the heterogeneous nature of $\mu\text{c-Si:H}$, it is not easy to draw a profile of the density of states within the gap. Nevertheless, the evidence of the existence of band-tail states has been reported in several studies. The results from the measurements of

photoluminescence [56], ESR [9], PDS [45], and photoconductivity [57] support the same idea regarding the existence of the conduction and valence band tails as well as defects in the gap. In addition, on the basis of the investigation performed on poly-Si, it is stated that the band-tail states in $\mu\text{c-Si:H}$ are caused by the boundaries between grains (coherent regions) within the columns. These boundaries correspond to deviations in bond lengths and angles [58].

A schematic diagram of the density of states within the gap of $\mu\text{c-Si:H}$ in Fig. 2.5 has been reported by Finger [29]. Fig. 2.5 reveals steep conduction and valence band tails. This is consistent with the investigation made by Brüggemann [59]. Indeed, from temperature-dependent ambipolar diffusion length measurements, the valence band tail parameter is estimated around 26 meV. Recently Dylla [60] reports a value around 31 meV obtained from transient photocurrent measurements. In addition, from photoluminescence measurements [56] a conduction band tail parameter of about 22 meV is determined from an exponential distribution. Recently, thermally stimulated currents performed on $\mu\text{c-Si:H}$ have shown the existence of a conduction band tail characterized with band tail parameter of around 22 meV [33].

The link between the transport and the structure of $\mu\text{c-Si:H}$ film is still not clearly explained in spite of the various studies devoted to this purpose. However, most of the investigations support the idea that the dominant transport in $\mu\text{c-Si:H}$ takes place in the disordered tissue that encapsulates the crystallite columns [36,61].

Chapter 3

Samples

This chapter presents a description of samples, which indicates the technique as well as the different deposition parameters with which the films were deposited. During the deposition of the sample, all the deposition parameters are kept the same, only the composition of hydrogen and silane has been varied. Therefore, samples with different crystalline volume fractions are expected.

Raman spectroscopy measurement has been performed on these samples [62] in order to identify them via the crystalline volume fraction parameter R_c (defined in chapter 2 (section 2.1)).

3.1 Deposition

The undoped $\mu\text{-Si:H}$ samples in this work have been deposited by hot wire chemical vapour deposition (HWCVD) technique at the Ecole Polytechnique in Paris, on glass (Corning 7059) [62]. All films were deposited at a wire and substrate temperature of 1500 °C and 300 °C respectively, at a total pressure of 0.1mbar and with a substrate-to-wire distance of 3 cm. In addition, the total gas flow rate (silane + hydrogen) was also kept constant at 150 sccm. For the whole sample only the ratio SC , defined as the silane -to- hydrogen flux $SC = [\text{SiH}_4]/[\text{H}_2]$, has been varied between 5% and 10%.

3.2 Crystalline volume fraction

Raman measurements have been applied on these samples, more information can be found in [62]. The crystalline volume fraction R_c , defined in chapter 2 (section 2.1), has been determined [62]. The sample series is composed of 5 samples whose R_c is: 34%, 42%, 52%, 79% and 88%. The sample thickness is about 0.8 μm , except for the sample with $R_c = 79\%$ whose thickness is about 2 μm .

Chapter 4

Photoconductive techniques

The first part of this chapter focuses on the description of photoconductivity techniques such as steady state photocurrent (SSPC) and steady state photocarrier grating (SSPG) measurements. The aim of these techniques is to determine the mobility lifetime product $(\mu\tau)_{n,p}$ for majority and minority carriers respectively.

The second part deals with the investigation of the photoelectronics properties of $\mu\text{c-Si:H}$ upon change of the crystalline volume fraction R_c by determining $(\mu\tau)_{n,p}$ at room temperature and at temperatures varying between 115 K and 430 K.

4.1 Dark conductivity and photoconductivity techniques (SSPC)

4.1.1 Sample geometry

In this work, the characterisation studies by different techniques have been carried out on samples deposited on glass with coplanar contact geometry. Aluminium electrodes separated by 0.5 mm and 1 mm are deposited on the sample. A representation of the coplanar configuration of the samples is shown in Fig. 4.1.

4.1.2 Dark conductivity

The conduction in the dark occurs essentially in the extended states close to the mobility edge between E_c and $E_c + kT$ for electrons and between E_v and $E_v - kT$ for holes. The dark conductivity σ_d is given by

$$\sigma_d = e\mu_n n + e\mu_p p \quad (4.1)$$

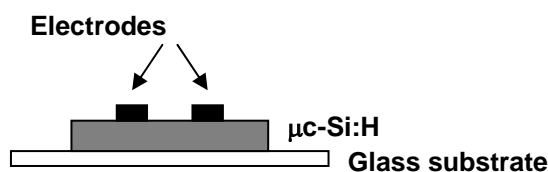


Figure 4.1: $\mu\text{c-Si:H}$ sample in coplanar configuration deposited on glass

The parameters μ_n and μ_p are the mobilities of electrons and holes. n and p denote the concentrations in the conduction and valence band for electrons and holes and e is the elementary charge. In the case where the majority carriers are electrons ($\mu_n n \gg \mu_p p$), the Fermi level position is related to the dark conductivity σ_d via the equation given by

$$E_c - E_F = kT \ln \left(\frac{\sigma_0}{\sigma_d} \right). \quad (4.2)$$

Here σ_0 the conductivity prefactor which is taken around 200 S cm^{-1} . We note that the σ_d values are obtained from the dark current I_d via the equation:

$$\sigma_d = \frac{I_d W}{V d h} \quad (4.3)$$

W is the width between the electrodes, V is the applied voltage between the electrodes, d is the sample thickness and h is the length of electrodes (see Fig. 4.2). Experimental values of σ_d obtained from $\mu\text{c-Si:H}$ sample are plotted in Fig. 4.3. According to Eq.4.2, the Fermi level $E_c - E_F$ at room temperature is equal to 0.58 eV.

4.1.3 Photoconductivity

The sample is illuminated with a continuous and monochromatic photon-flux F . The photon energy is larger than the gap of the material. The generation rate $G_x(x)$ of the created carriers at a distance x from the sample surface (see Fig. 4.2) is given by

$$G_x(x) = \eta \alpha (1 - R) F \exp(-\alpha x) \quad (4.4)$$

where α denotes the absorption coefficient corresponding to the excitation wavelength $\lambda = 633 \text{ nm}$, R is the reflection. Here η is the quantum efficiency of free carrier generation.

An average value of G is given by

$$G = \frac{1}{d} \int_0^d G_x(x) dx = \frac{1}{d} \eta (1 - R) F (1 - \exp(-\alpha d)) \quad (4.5)$$

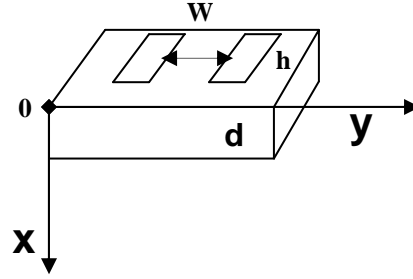


Figure 4.2: Sketch of the sample in 3 dimensions. d is the thickness, W is the width between electrodes and h the length of the electrodes.

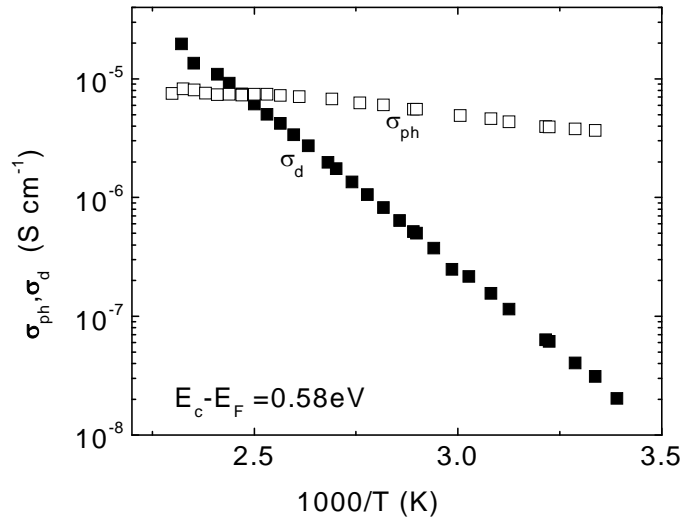


Figure 4.3: Temperature dependence of the photoconductivity (σ_{ph}) and dark conductivity (σ_d) in $\mu\text{c-Si:H}$. $E_c - E_F = 0.58 \text{ eV}$ is the Fermi level at room temperature calculated by applying Eq. 4.2.

In the whole volume, the photoconductivity σ_{ph} , due to the concentrations Δn and Δp of photo-generated carriers (electron and hole) in the conduction and valence band, is given by

$$\sigma_{ph} = e\mu_n\Delta n + e\mu_p\Delta p = eG(\mu_n\tau_n + \mu_p\tau_p) \quad (4.6)$$

with $\tau_n = \frac{\Delta n}{G}$ and $\tau_p = \frac{\Delta p}{G}$

When $(\mu\tau)_n$ is much larger than $(\mu\tau)_p$, Eq. 4.6 will be written as

$$\sigma_{ph} = eG(\mu_n\tau_n) \quad (4.7)$$

From Eqs. 4.5 and 4.7, σ_{ph} is expressed as

$$\sigma_{ph} = \eta \frac{1}{d} e (\mu\tau)_n (1-R) F(1 - \exp(-\alpha d)) \quad (4.8)$$

It should be noted that σ_{ph} is related to I_{ph} by

$$\sigma_{ph} = \frac{I_{ph} W}{V d h} \quad (4.9)$$

The photocurrent I_{ph} is obtained after subtraction of dark current I_d ($I_{tot} = I_{ph} + I_d$). I_{tot} is the measured current. Fig 4.3 shows an example of photoconductivity in $\mu\text{-Si:H}$ sample.

4.2 Steady state photocarrier grating technique (SSPG)

The SSPG technique allows to measure the ambipolar diffusion length L_{amb} of semiconductors for which L_{amb} lies in the sub-micrometer region ($L_{amb} \ll 1\mu\text{m}$).

This technique was first developed by Ritter *et al.* [63-65] and then applied by Balberg on amorphous silicon [66]. Later it was performed on a-Si_{1-x}Ge_x:H by Abel and Bauer [67] and on $\mu\text{-Si:H}$ by Brüggemann [59]. The principle in this technique consists of creating interference in the sample from two coherent and polarized light beams i_1 and i_2 of intensity I_1 and I_2 respectively ($I_1 \gg I_2$). The intensity I_{ph} relating I_1 to I_2 is given by

$$I_{ph}(y) = I_1 + I_2 + 2\sqrt{I_1 I_2} \cos(2\pi y / \Lambda) \quad (4.10)$$

y represents the direction perpendicular to the contacts. We note that I_1 and I_2 originate from the same monochromatic source of wavelength λ . The optical grating, is characterized with a grating period Λ given by

$$\Lambda = \frac{\lambda}{\left[2 \sin\left(\frac{\theta}{2}\right) \right]} \quad (4.11)$$

θ is the angle between i_1 and i_2 . When the grating period Λ is much longer than L_{amb} , a concentration grating of photocarriers is created in the sample. In contrast, when Λ is shorter than or the same order of magnitude as L_{amb} , the carriers diffuse and hence the photocarrier gratings disappear.

On the basis of small signal approach, Ritter [65] developed a theory which assumes ambipolar transport, where electron and holes diffuse together and local charge neutrality is

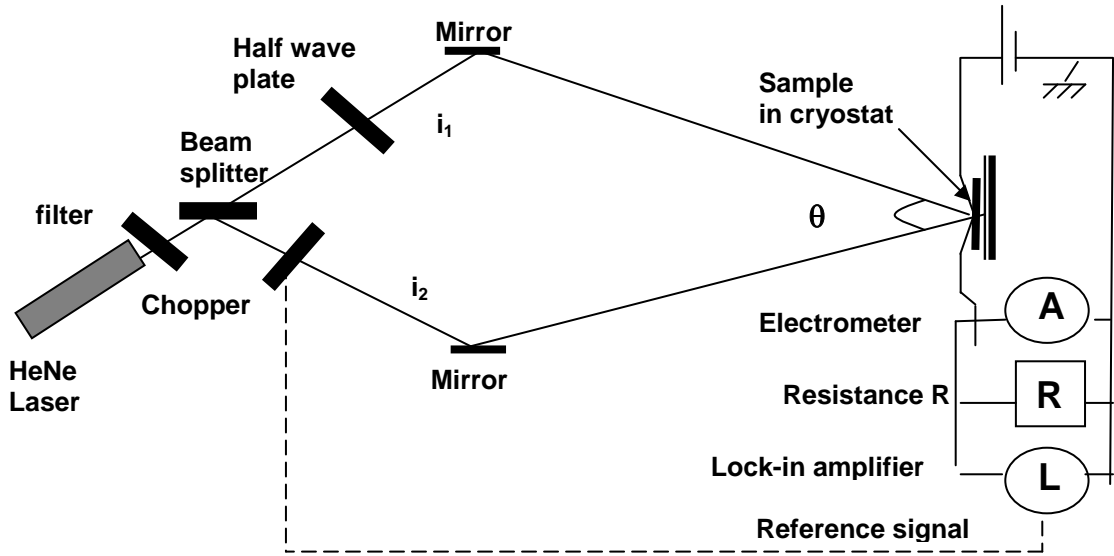


Figure 4.4: Steady-state photocarrier grating experiment: interference with grating period depending on angle θ .

maintained. Starting from the diffusion equation of carriers, Ritter derived a simple relationship relating A to the β coefficient defined by

$$\beta = \frac{u_{coh}}{u_{incoh}}. \quad (4.12)$$

Experimentally, the ratio β is obtained for each A by determining first the coherent-photocurrent signal u_{coh} measured by a lock-in amplifier in the case where i_1 and i_2 have the same polarisation (with interference). u_{incoh} is obtained by 90° rotation of the polarization of the light beam i_2 via the half wave plate (without interference).

The simple equation is expressed by

$$\beta(\Lambda) = 1 - \frac{2Z}{\left[1 + \left(\frac{2\pi L_{amb}}{\Lambda}\right)^2\right]^2} \quad (4.13)$$

Z is a parameter which is related to the grating quality.

Figure 4.4 shows the experimental setup for SSPG.

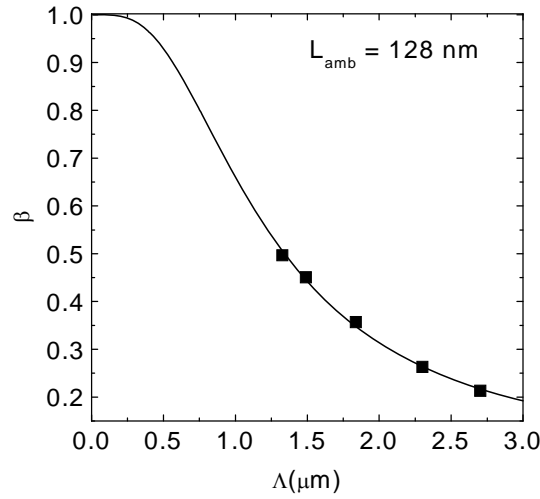


Figure 4.5: Experimental data of β (symbols) depending on the grating period Λ . According to Eq. 4.13, the fit (full line) of these data gives a value of the diffusion length $L_{amb} = 128$ nm.

The fit of experimental data, by application of Eq. 4.13, determines L_{amb} . $(\mu\tau)_{amb}$ [67] could be deduced via the equation given by

$$(\mu\tau)_{amb} = \frac{eL_{amb}^2}{2kT}. \quad (4.14)$$

The $(\mu\tau)_{amb}$ parameter is related to $(\mu\tau)_n$ and $(\mu\tau)_p$ by the relationship [67] given by

$$(\mu\tau)_{amb} = \frac{(\mu\tau)_n \times (\mu\tau)_p}{(\mu\tau)_n + (\mu\tau)_p}. \quad (4.15)$$

The knowledge of L_{amb} and σ_{ph} from SSPG and SSPC respectively allows to determine separately the parameters $(\mu\tau)_n$ and $(\mu\tau)_p$ via Eqs. (4.6) and (4.15).

Figure 4.5 shows experimental values of β against Λ for $\mu\text{-Si:H}$. Good fit is shown using Eq. 4.13 and leading to the value of $L_{amb} = 128$ nm.

4.3 Experimental results

4.3.1 Mobility lifetime product obtained at room temperature

Figure 4.6(a) shows the values of $(\mu\tau)_n$ and $(\mu\tau)_p$ against dark conductivity σ_d for 5 samples with different R_c (34%, 42%, 52%, 79% and 88%). These measurements were carried

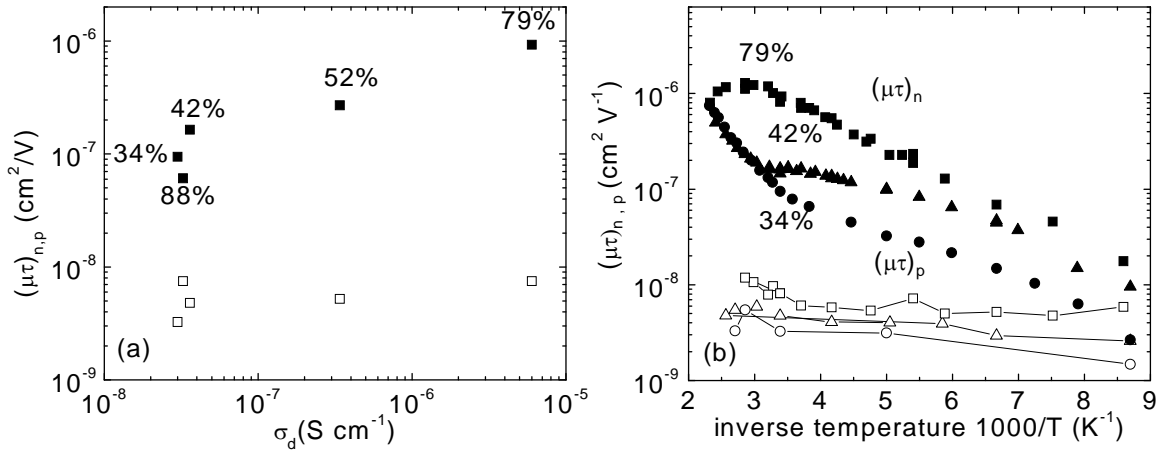


Figure 4.6: Mobility-lifetime product of electrons and hole against dark conductivity σ_d . The measurements are carried out for different samples at room temperature (a). Temperature dependence of the mobility-lifetime product for electron (full symbols) and hole (open symbols). The measurements are carried out at photon flux equals $10^{16} \text{ cm}^{-2} \text{ s}^{-1}$. Three samples with 3 different crystalline volume fractions are considered (b).

out at room temperature after annealing at about $150 \text{ }^\circ\text{C}$ for 30 min. The light source was a red He-Ne laser, with which the sample was illuminated at photon-flux around $10^{16} \text{ cm}^{-2} \text{ s}^{-1}$.

The experimental data in Fig. 4.6(a) show that $(\mu\tau)_n$ increases with increasing σ_d , except for the sample with $R_c = 88 \%$. The increase of σ_d involves also the shift of the position of Fermi level towards the conduction band edge according to Eq. 4.2. A very slight variation of $(\mu\tau)_p$ is detected with increasing R_c .

4.3.2 Temperature dependence of the mobility lifetime product

Figure 4.6(b) displays the temperature-dependent mobility-lifetime product for electrons (full symbols) and holes (open symbols) for samples with $R_c = 34 \%$, 42% and 79% . For all samples, $(\mu\tau)_n$ increases with increasing temperature between 110K and 210 K . In addition we can observe, only for the sample with $R_c = 79 \%$, a pronounced maximum around 330 K , which is accompanied with a decrease of $(\mu\tau)_n$ when the temperature increases. However, for all samples, $(\mu\tau)_p$ remains temperature independent in the whole range of the temperatures. It is noted that the γ parameter, known as the power dependence of the

photoconductivity ($\sigma_{ph} \approx F^\gamma$) decreases when R_c increases. For example for the sample with $R_c = 79\%$, γ is around 1.1 when $110\text{ K} < T < 350\text{ K}$, while for $R_c = 34\%$, γ is around 0.6 when $115\text{ K} < T < 350\text{ K}$.

4.4 Discussion

The increase of the mobility lifetime product as well as the shift of the Fermi level at room temperature (Fig. 4.6(a)), are related, by many authors, to a change of the occupancy of dangling bonds in the gap of the material [68-70]. This shift involves also a reduction in the parameter γ if we consider the samples $R_c = 79\%$ and 34% . This trend has been also observed in amorphous silicon [68,69].

The increase in the $(\mu\tau)_n$ with increasing the temperature (Fig. 4.6(b)) is due to the decrease of the number of recombination centres. Similar behaviour has been reported by Vomvas and Fritzsche [71] on the n-type amorphous silicon. In addition it has been also reported that, the thermal quenching, characterised by a decrease or saturation of the photoconductivity, has not been observed in this sample [71]. This agrees well with the results of $(\mu\tau)_n$ for the sample with $R_c = 79\%$. Indeed this sample, having a character n-type more pronounced compared with the rest of the samples, does not show any thermal quenching.

As has been indicated above, the sample with $R_c = 88\%$ is an exception in the studied series. In spite of the high crystalline volume fraction of this sample, the corresponding values of the Fermi level E_F and $(\mu\tau)_n$ are similar to that of the sample with low R_c (see Fig. 4.6(a)). This may be due to the distribution of the amorphous layer of the sample which is inhomogeneous. This leads to regions purely crystalline which have been explored by Raman measurements.

In addition for all samples, $(\mu\tau)_p$ hardly changes with the temperature (see Fig. 4.6(b)). Referring to [60], it has been shown that, from TOF experiment, the mobility of holes in extended states is around $1\text{ cm}^2\text{V}^{-1}\text{ s}^{-1}$. This value is one order of magnitude smaller compared to that of electrons which is supposed to be $10\text{ cm}^2\text{V}^{-1}\text{ s}^{-1}$. Also Fig. 4.6(b) shows that $(\mu\tau)_n > (\mu\tau)_p$. All these indications show that the contribution of the holes in the transport could be neglected. Brüggemann *et al.* related $(\mu\tau)_p$ changes to a steeper distribution of valence band tail compared to a-Si:H [59].

Chapter 5

Thermally stimulated currents (TSC)

5.1 Principle

The thermally stimulated current technique is a quantitative spectroscopic tool which allows to probe the states in the energy gap. A sketch of TSC is shown in Fig. 5.1. It illustrates the different steps carried out during the TSC measurement. The figure indicates three different parameters against the time: the photon-flux rate ϕ , the temperature T and a semi-logarithmical scale of conductivity σ . The experimental procedure consists of cooling the sample to a low temperature T_0 at which the sample is illuminated with ϕ for a time t_{ill} in order to fill the traps. The light is switched off and the sample is kept in darkness at T_0 during a relaxation time t_{rel} . In this step σ rapidly and then slowly decreases.

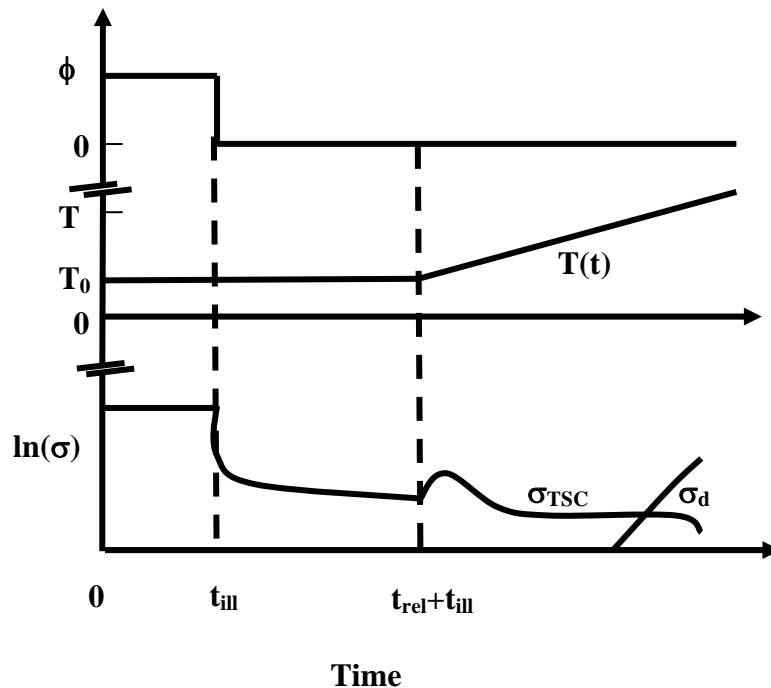


Figure 5.1: TSC sketch illustrating different steps during measurement.

According to a variation $T(t)$, usually supposed linear, the sample is progressively heated to the temperature T . The trapped carriers are released. These released carriers contribute to an excess conductivity measured as an excess current in the presence of an

electrical field. The excess conductivity after subtraction of the conductivity (σ_d) is the TSC conductivity σ_{TSC} .

More than 40 years ago, TSC was proposed [72] as a potential technique for trap level spectroscopy. For many years this technique motivated extensive research, while using a discrete trap model [73-81]. Simmons *et al.* [30,82-85] suggested a theory in which they considered a system with a continuous energy distribution of localized states below the conduction band edge. In this work, a sufficiently high field was applied in order to remove the released carriers without recombining and retrapping. Simmons showed that the electrons contributing to the current come from an energy interval located around E_m which is the energy of the peak net emission rate.

Fritzsche and Ibaraki [31,86] applied the theory on amorphous semiconductors and proposed an analysis of TSC based on the multiple trapping model. Quasi-equilibrium conditions are assumed in which the rate of change of excess free carriers is small.

TSC arises from a ‘balance’ between the net thermal emission rate (re-emission minus retrapping) and recombination. There is thus an important distinction also recognised in the discrete trap models [72], between the ‘weak’ retrapping case, where released charge carriers simply recombine, and the ‘strong’ retrapping, where released carriers may be retrapped many times before recombining.

The approach adopted by Fritzsche *et al.* [31,32,86-90] takes into account only the recombination and the emission rate without retrapping. To describe empirically the effects of strong retrapping, Fritzsche and Ibaraki introduced an ‘effective attempt-to-escape frequency’ ν_{eff} . In practice, retrapping into states around E_m plays the most significant role during TSC and leads to a slowing in the descent of E_m toward the Fermi level. Consequently, ν_{eff} is smaller than the actual attempt-to-escape frequency ν_0 . It is noted that ν_0 , taken between 10^{11} s⁻¹ and 10^{12} s⁻¹, is in most cases energy independent [83,87]. At a temperature where TSC approaches the dark conductivity, ν_{eff} is experimentally calculated under the condition in which σ_{TSC} equals σ_d .

Fritzsche and Ibaraki also considered the effect of variations in carrier lifetime which occur as the TSC temperature increases, and which affect the emission-recombination ‘balance’. By combining separate photoconductivity measurements with TSC taken over the same temperature range to reveal the mobility lifetime-product, their approach has been successfully applied in order to obtain the density of states (DOS) of hydrogenated

amorphous silicon alloys (a-Si:H and a-SiN_x:H). Good agreement has been shown between the DOS from TSC and from other experimental techniques as space-charge-limited currents. However, the physical TSC interpretation at a low temperature has stimulated some controversy [91-94]. For example, Fritzsche and Ibaraki concluded that the peak observed in the TSC spectra at low temperature is not correlated to a DOS structure [32,86]. Indeed, they suggested that the low temperature peak of TSC is due to the product between the increase of the occupation function $f_0(E)$ at T_0 and the decrease of the term composed of the density of states multiplied by the mobility lifetime product.

Misra [96,97] proposed a TSC model based on the strong retrapping formalism. He showed a good agreement of DOS results from TSC measurements performed on a-Si:H compared with those from the field-effect experiment. Later, Landweer and Bezemer [98] developed an approach similar to that of Fritzsche. In addition, they proposed a new experimental method in which the sample is exposed to low intensity light pulses during the TSC experiment in order to obtain the mobility lifetime product.

Gu *et al.* [99] developed a model where all processes as thermal emission, trapping and recombination are taken into account. They found that the structure in the TSC spectra is related to that of the DOS. At a temperature below 120 K, Baranovskii *et al.* [100,101] described a new theory where the transport properties are due to the hopping of electrons via localized band tail states.

Over the past few years, Smail *et al.* [102] presented a complete numerical simulation of TSC applied to a-Si:H taking into account all the possible transitions for both electrons and holes. They concluded that it is difficult to interpret experimental results from TSC measurements. Schmidt *et al.* [103] also developed a numerical simulation of TSC. As a result, a very simple empirical formula was provided in order to evaluate the DOS in the gap.

Recently Souffi *et al.* [33] applied TSC on microcrystalline silicon. Also, C. Main *et al.* [104, 105] have developed a simulation on TSC where all processes such as recombination, retrapping and emission are taken into account. The strong and weak retrapping regimes have been investigated using a flat distribution of the DOS.

In this work, a simulation of TSC is applied in order to investigate strong and weak retrapping regimes by considering different forms of the DOS. Also, the simulation has allowed to check the validity of the various published approaches. Some suggestions about the strong retrapping have been underlined. Furthermore, TSC is performed on $\mu\text{c-Si:H}$ samples having different crystalline volume fraction. A combined experiment – simulation approach allowed to provide the evidence of the strong and weak retrapping regimes and

hence to get the DOS as well as trap parameters.

5.2 Approaches for the determination of the density of states from TSC

The purpose of this section is to describe some approaches adapted to the TSC technique. We start with the illustration of the origin of the maximum TSC emission energy which has been firstly reported by Simmons in order to get $E_c - E_m(T)$ [83,84]. In addition, we will address the different approximations which have been suggested by Fritzsche and Ibaraki [31,32] in order to get quantitatively the density of states $g(E_m)$ in the gap from the TSC. Besides, the Landweer and Bezemer approach [98] will also be presented. It will be indicated that they have again calculated analytically $E_c - E_m(T)$ and $g(E_m)$ at another starting temperature T_0 applying a similar procedure to that of Fritzsche's. Furthermore, the numerical approach of Schmidt *et al.* [103] will also be reported.

5.2.1 Maximum TSC emission energy

By considering a continuous distribution of traps in the gap, Simmons *et al.* [30,83-84] analytically described the current I_n by applying a high electrical field:

$$I_n = (1/2) eL \int_{E_F}^{E_c} e_n(E_c - E) f(E_c - E) g(E_c - E) dE \quad (5.1)$$

L is the thickness of the sample, e is the elementary charge, $g(E_c - E)$ is the trap density of states in the gap, E_F is the Fermi level, and $e_n(E_c - E)$ is the thermal emission coefficient for electrons out of the trap at temperature T and E is the energy of the trap. $e_n(E_c - E, T)$ is related to the attempt-to-escape frequency ν_0 by: $e_n(E_c - E, T) = \nu_0 \exp(-(E_c - E)/kT)$. $f(E_c - E, T)$ denotes the occupation function given by:

$$f(E_c - E, T) = f_0(E_c - E, T_0) e^{-\frac{1}{b} \int_{T_0}^T e_n(E_c - E, T) dT} \quad (5.2)$$

b is the heating rate, T_0 is the initial temperature at which the sample is illuminated and f_0 is the initial occupation function.

Simmons defined the function $P(E_c - E)$ by

$$P(E_c - E, T) = e_n(E_c - E, T) e^{-\frac{1}{b} \int_{T_0}^T e_n(E_c - E, T) dT} \quad (5.3)$$

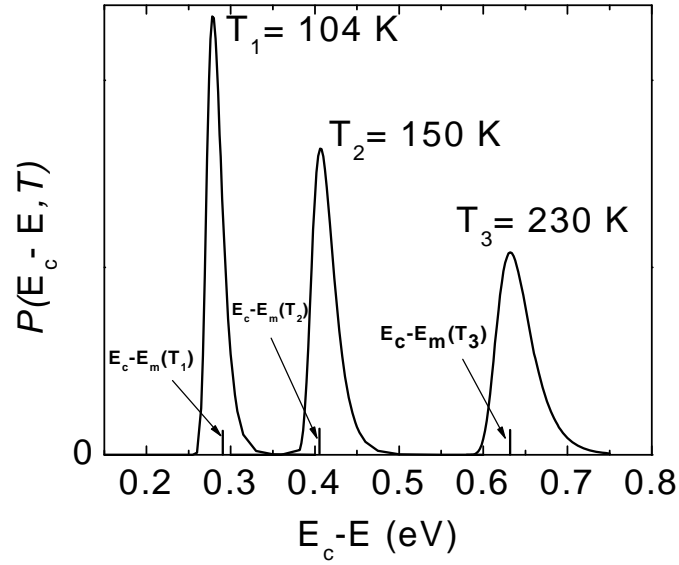


Figure 5.2: Distribution of energetic probability for emission from traps $P(E_c - E, T)$ for 3 different temperatures 104 K, 150 K and 230 K.

After calculations of the function $P(E_c - E)$ at several temperatures, Simmons *et al.* showed that the plot of $P(E_c - E)$ against the energy for different temperatures exhibits a pronounced peak at the energy $E_c - E_m$. $E_c - E_m$ indicates the trap position which contributes most significantly to the current.

We have also numerically solved Eq. (5.3) using Fortran. $P(E_c - E)$ is plotted in Fig. 5.2 for different temperatures: 104 K, 150 K and 230 K. Figure 5.2 exhibits a pronounced peak at $E_c - E_m$ that has a half width of $3kT$, region in which $P(E_c - E)$ presents a maximum. This means a very large contribution of current comes from traps located within the energy $3kT$ of $E_c - E_m$. We can then easily understand that to obtain $E_c - E_m(T)$, which will later be used as an energy scale to get the DOS, we have to solve the equation given by

$$\left. \frac{\partial P(E_c - E, T)}{\partial E} \right|_{E=E_m} = 0 \quad (5.4)$$

Using the Eq. (5.4), Simmons *et al.* found for $E_c - E_m \gg kT$:

$$kT^2 e_n (E_c - E_m) / (b \times (E_c - E_m)) = 1, \quad (5.5)$$

To a good approximation where $E_c - E_m$ depends linearly on T , Simmons used Eq. 5.5 and then

gave an analytical expression relating $E_c - E_m$ to T , that we can find in the references [83,84]. It is important to point out that the energy scale provides values of $E_c - E_m$ which are accurate to within 2% of the values obtained from numerical solution of Eq. (5.5) [84].

By adopting the same procedure, Fritzsche *et al.* [31,86] as well as Landweer and Bezemer [98] calculated E_m and they obtained:

$$\text{from Fritzsche} \quad E_c - E_{m,a}(T) = kT \ln(41K\nu_0/b) - 0.015\text{eV}, \quad (5.6)$$

$$\text{from Landweer} \quad E_c - E_{m,a}(T) = 0.97kT \ln(52K\nu_0/b) - 0.017\text{eV}, \quad (5.7)$$

Index a indicates that $E_c - E_{m,a}$ is described by an analytical function and ν_0 is the attempt-to-escape frequency. The difference between Eqs. (5.6) and (5.7) is that these equations are obtained at 2 different initial temperatures T_0 , 130 K and 85 K respectively.

It should be noted that in this work Landweer and Bezemer approach is applied although T_0 at which the sample is illuminated is around 90K. We checked that the obtained DOS from T_0 equals 90 K or 85 K are very similar.

5.2.2 Density of states

Fritzsche and Landweer approaches

In reality, σ_{TSC} arises from a balance between thermal emission from the trap to the transport states, retrapping and recombination. The rate equation dn/dt for free electrons is given by

$$\frac{dn}{dt} = \underbrace{\int_{E_F}^{E_c} e_n(E) f(E, T) g(E) dE}_{\text{emission rate}} - \underbrace{\int_{E_F}^{E_c} n c_n (1 - f(E, T)) g(E) dE}_{\text{retrapping rate}} - \underbrace{\frac{n - n_0}{\tau_r}}_{\text{recombination rate}} \quad (5.8)$$

n is the concentration of free electrons in the conduction band, τ_r is the carrier lifetime and c_n is the capture coefficient.

It is difficult to get an analytical solution of Eq. (5.8). For this reason, Fritzsche *et al.* [31,86] have considered several approximations to solve Eq. (5.8):

- A quasi steady states condition during TSC is assumed leading to $dn/dt \approx 0$
- The retrapping rate is neglected
- To take into account the retrapping rate, Fritzsche proposed to substitute the attempt-to-escape frequency ν_0 in Eq. (5.6) by an effective attempt-to-escape frequency ν_{eff} . In addition, in the case of strong retrapping, he suggested to calculate the value of ν_{eff} via Eq. (5.6) at the temperature where $\sigma_{TSC} = \sigma_d$.

From the above approximations, Fritzsche easily solved the Eq. (5.8). Indeed, we can observe that the emission rate is balanced by the recombination rate leading to:

$$\sigma_{TSC}(T) = e(\mu\tau)_n g(E_{m,a}) f_0(E_{m,a}) 1.2b |E_{m,a}| / T, \quad (5.9)$$

Fritzsche suggested to determine the mobility lifetime product $(\mu\tau)_n$ from separated photoconductivity measurements. $(\mu\tau)_n$ is given by

$$(\mu\tau)_n = \frac{\sigma_{ph}}{eG} \quad (5.10)$$

where G is the photogeneration and σ_{ph} is the photoconductivity. The latter is related to the photogeneration rate by

$$\sigma_{ph} = G^\gamma. \quad (5.11)$$

Here γ is known as the light intensity exponent of the photoconductivity [76]. The photon flux was adjusted with neutral density filters such that

$$\sigma_{ph}(T) = \sigma_{TSC}(T). \quad (5.12)$$

Equation 5.12 is used in order to extrapolate the experimental current data to the low current. The extrapolation is not needed if the measurable photocurrent range covers the TSC current.

Similar calculations have been performed by Landweer and Bezemer [98] by applying the same approximations. The density of states as well as the energy scale are given by

$$g(E_{m,a}) = \frac{\sigma_{TSC}}{e(\mu\tau)_n f_0(E_{m,a}) b \left| \frac{dE_{m,a}}{dT} \right|} \quad (5.13)$$

$$E_c - E_{m,a}(T) = 0.97kT \ln(52Kv_{eff}/b) - 0.017\text{eV} \quad (5.14)$$

It is important to point out that the term $\left| \frac{d(E_{m,a})}{dT} \right|$ is temperature independent by referring to Eq. (5.14).

Fritzsche has examined the initial rise of TSC at a low temperature. Schematically he explained that the presence of the low temperature peak of σ_{TSC} is due to the product of $f_0(E)$ and $(\mu\tau)_n g(E)$ [91,93]. However, insufficient agreement is shown between calculated and experimental σ_{TSC} at $T_0 = 130$ K [31,32]. This is because $(\mu\tau)_n$ is considered to be temperature independent during the initial rise. We will show from the simulation and experiment that the initial rise is very well reproduced taking into account the occupation function $f_0(E_m)$ as well as $(\mu\tau)_n(T)$ and $g(E_m)$.

Schmidt's approach

Schmidt *et al.* [103] carried out a numerical simulation taking into account not only all processes such as thermal emission, retrapping and recombination, but also the contributions of both electrons and holes.

To obtain $E_c - E_{m,a}(T)$, Schmidt *et al* solve numerically the function $P(E, T)$ peaked with a sharp maximum at $E_c - E_{m,a}$. The difference with Bezemer's procedure is that Schmidt provides an easy-to-use functional dependence ($E_c - E_{m,a}$) for different T_0 , while from Bezemer $E_c - E_{m,a}(T)$ is more restricted to a single T_0 . Indeed, from the simulation he obtained $E_c - E_{m,a}$ at each temperature. Several cases are examined leading to an empirical relationship given by

$$E_c - E_{m,a}(T) = C_1(T_0)k_B T \ln(C_2(T_0)v_{eff}/b) - C_3(T_0), \quad (5.15)$$

where C_1 , C_2 and C_3 are T_0 -dependent parameters.

Similar to Bezemer's approach, Schmidt found the expression of σ_{TSC} by applying $\frac{\partial n}{\partial t} \approx 0$ (quasi steady state equilibrium). $\frac{\partial n}{\partial t} \approx 0$ is checked from the simulation. Then, σ_{TSC}

from the simulation is given by

$$\sigma_{TSC}(T) = e(\mu\tau)_n \int_{E_v}^{E_c} g(E) f_0(E) W(E) \delta(E - E_m) dE \quad (5.16)$$

$W(E)$ is a weighting factor such that $P(E) = W(E) \delta(E - E_m)$. From Eq. (5.16), we get

$$\sigma_{TSC}(T) = e(\mu\tau)_n g(E_m) f_0(E_m) W(E_m) \quad (5.17)$$

He also numerically found $W(E)$ which is empirically given by

$$W(E) = b \left[0.97k \ln(v_{eff}T/b) - 7.33 \times 10^{-5} \right] \quad (5.18)$$

It has been observed that $W(E)$ is slightly temperature dependent, and $W(E) \approx b \left| \frac{dE_{m,a}}{dT} \right|$.

It is important to point out that Schmidt, in his model, supposed that $f_0(E_m, T_0) = 1$, Eq. (5.17)

is then written as:

$$g(E_m) = \frac{\sigma_{TSC}(T)}{(\mu\tau)_n(T)W(T)} \quad (5.19)$$

We note that in this work the Eqs. (5.15) and (5.19), obtained from Schmidt's approach, are frequently applied because the DOS could be calculated at different T_0 . For comparison, the Eqs. (5.12) and (5.13) from Landweer and Bezemer approach are used.

For all of the chapters, we note also that the plot of the density of state $g(E_m)$, obtained by applying either Eqs. (5.13) or (5.19), is labeled TSC-DOS.

Chapter 6

Numerical Simulation of TSC

In the present chapter, a simulation of thermally stimulated currents (TSC) is applied in order to discriminate between strong and weak retrapping regimes.

First, some details regarding the simulation are illustrated. From a given density of states (DOS) presented by a continuous distribution, the differential equations for the density of free and trapped carriers are numerically solved in order to obtain at a given temperature the density of carriers in the conduction band.

The density of states as well as the heating rate, capture coefficient, photo-generation rate, carrier lifetime and relaxation time are used as input parameters in the simulation in order to extract the thermally stimulated conductivity (σ_{TSC}).

In this chapter, Schmidt's approach [103] is chosen to reconstruct the DOS from simulated σ_{TSC} . The validity of this approach is checked in the case of weak retrapping. In contrast, in the case of strong retrapping, some suggestions made by Fritzsche *et al* [31,32] are investigated and discussed.

To identify the retrapping regime, different criteria are studied and discussed with those proposed in the literature. In addition, the knowledge of the trapped carrier density from the simulation enables us to obtain the occupation function calculated at a given temperature. As a result some features for weak and strong retrapping are detailed via the related occupation function.

6.1 Simulation details

A system with a distribution $N_t(E)$ of trap states in the upper half of the band gap, has been considered. The TSC simulation presented below only concerns electron-dominated conduction and a single trap species of monovalent states characterized by the capture coefficient c_n for electrons. The conductivity σ_{TSC} is related to $n(t)$ and to the electron concentration n_0 in the dark by

$$\sigma_{TSC} = e\mu_n (n - n_0). \quad (6.1)$$

A quasi Fermi level $E_c - E_q$ during TSC can be expressed by

$$E_c - E_q = kT \ln \left(\frac{N_c}{n} \right) \quad (6.2)$$

N_c denotes the effective density of conduction band states.

After illumination at low temperature the electron concentration $n(t)$ in extended states arises during heating from a balance between thermal emission, recombination and trapping. The kinetics during the TSC process is described by the rate equation for electrons

$$\frac{dn}{dt} = -n \int_{E_{\max}}^{E_c} c_n (N_t - n_t) dE + \int_{E_{\max}}^{E_c} e_n n_t dE - \frac{n - n_0}{\tau_r}, \quad (6.3)$$

where

$$e_n = \nu_0 e^{-\frac{(E-E_c)}{kT}}, \quad (6.4)$$

n_t is the trapped electron density, τ_r is the recombination time, and $E_c - E_{\max}$ is the maximal energy taken equal 0.7 eV. The ν_0 parameter, introduced in the thermal emission expression $e_n(E)$, is the attempt-to-escape frequency which is equal to $c_n N_c$. The difference between Eqs. (6.3) and (5.8) is that $N_t \times f$ is replaced by n_t (f is the occupation function), and E_F by E_{\max} .

Equation (6.3) is intractable to analytical solution. Therefore the numerical solution is determined by solving a set of non-linear differential equations by application of the software developed by C. Main and S. Reynolds. The integral is transformed into the sum for numerical calculation with energy steps $\Delta E = E_{\max}/N$ (N is the total number of energetic levels).

The rate equation for the trapped electron density at level i is given by

$$\frac{dn_{i_i}}{dt} = n c_n (N_{i_i} - n_{i_i}) - e_{n_i} n_{i_i}, \quad (6.5)$$

where n_{i_i} and N_{i_i} are defined respectively as $n_{i_i} = n_t / \Delta E$ and $N_{i_i} = N_t / \Delta E$. We note that the number of the non-linear differential equations is $N+1$.

The ratio r defined as retrapping rate to recombination rate is given by

$$r = \frac{\sum_i n c_n (N_{i_i} - n_{i_i})}{n / \tau_r} = \frac{\tau_r}{\tau_i}, \quad (6.6)$$

where τ_i is the retrapping time, calculated into the interval $3kT$ of E_m ($\tau_i = \sum_i c_n (N_{i_i} - n_{i_i})$), i is the energetic level number around E_m).

It is important to point out that the occupation function is deduced at a given temperature from N_i and n_i such that

$$n_i = N_i f \quad (6.7)$$

A temperature scan is described by a linear function $T = bt + T_0$, b is the heating rate and T_0 is the initial temperature.

The parameters generation rate, initial low temperature, relaxation time, carrier lifetime, heating rate, as well as capture coefficient are introduced in the simulation as input parameters.

6.2 Illustration of both strong and weak retrapping

In order to discriminate the strong and weak retrapping regimes, as well as the intermediate regime between them, different input DOS are considered and different parameters such as carrier lifetime or capture coefficient are varied.

The work in section 6.2.1 deals with the variation of the carrier lifetime for two different densities of states. A detailed discussion of retrapping regime features is followed by a summary of criteria allowing the identification of the retrapping regime. Furthermore, at a given carrier lifetime, the conduction band tail parameter, heating rate variation, and capture coefficient are also varied in sections 6.2.3, 6.2.4, 6.2.5, respectively.

It is important to point out that in the previous studies (from section 6.2.1 to section 6.2.5), the carrier lifetime is temperature-independent. In the section 6.2.6, we will examine strong and weak retrapping regime by using the same input density of states as that used in the section 6.2.1. The difference is that the carrier lifetime, in this section, is considered to be temperature dependent.

6.2.1 T-independent carrier lifetime

As has been already explained, this section deals with strong and weak retrapping regimes by varying the carrier lifetime τ_r . For a given density of states, the τ_r variation shifts σ_{TSC} between strong and weak retrapping. In order to obtain more information, two different input DOS in this section are considered where carrier lifetime parameter only is varied between 2×10^{-4} s and 2×10^{-10} s. The first DOS is the sum of conduction band tail and flat density of states, and the second one is only composed of flat density of states. In this section, it is demonstrated that, from the values of effective attempt-to-escape frequency ν_{eff} and attempt-to-escape frequency ν_0 , strong and weak retrapping can be identified. The ratio retrapping rate to recombination rate is also calculated. In addition, the knowledge of the corresponding occupation function also emphasizes the retrapping regime nature.

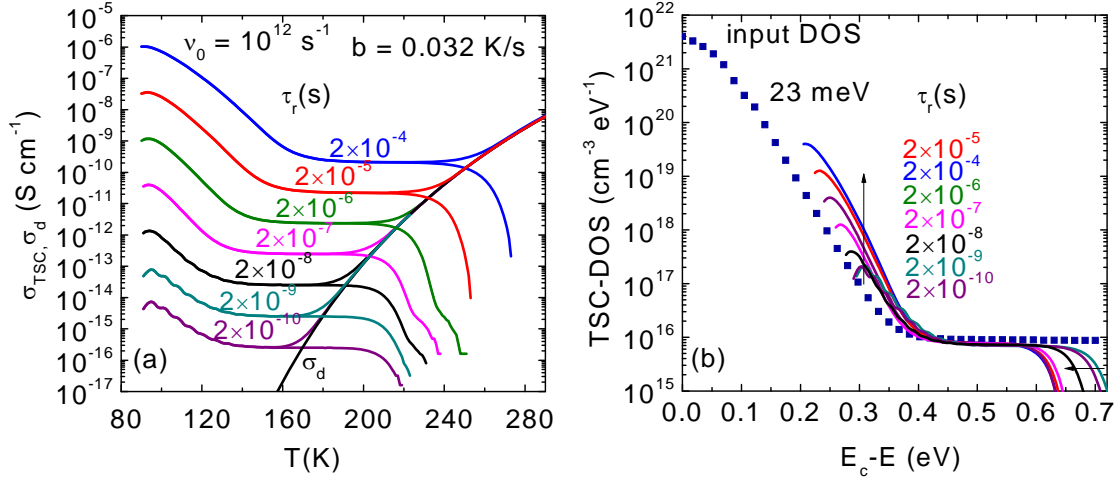


Figure 6.1: Simulated TSC and dark conductivity for varying lifetime τ_r between 2×10^{-10} s and 2×10^{-4} s at constant heating rate $b = 0.032$ K/s (a). Reconstructed TSC-DOS from (a) with ν_{eff} calculated using $\sigma_{TSC} = \sigma_d$ after Fritzsche (b). The vertical arrow shows the increase of τ_r from bottom to top. The horizontal arrow shows 3 different cut-offs (from right to left: τ_r equals 2×10^{-10} s, 2×10^{-9} s, 2×10^{-8} s. The input density of states represented by square symbols is added (b).

The main information relevant in this section is to show that the empirical energy scale where ν_0 is substituted by ν_{eff} in order to take into account strong retrapping [91,93] can not be applied for a DOS which is the sum of conduction band tail states and a flat DOS

A. Input DOS = conduction band tail + flat DOS

For an illustration of weak and strong retrapping kinetics, a continuous distribution $g(E)$ of traps in the forbidden gap extending from E_c to $E_c - E = 0.7$ eV is proposed as input parameter in the simulation. $g(E)$ is represented by square symbols in Fig. 6.1(b).

$g(E)$ here is the sum of one linear and two exponential functions. The slope of the exponential function determines the width of conduction band tail E_0 ($g(E) \propto \exp(-(E_c - E)/E_0)$).

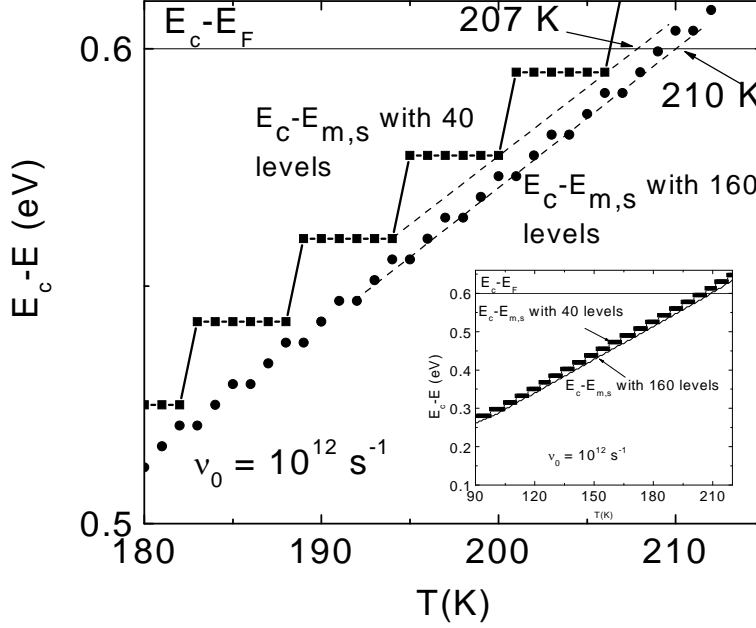


Figure 6.2: Temperature-dependent computed peak emission energy $E_c - E_{m,s}$ obtained from two distribution of trap levels composed of 40 and 160 levels respectively. The Fermi level $E_c - E_F$ is added.

Between $E_c - E = 0.105$ eV and $E_c - E = 0.35$ eV, $E_0 = 23$ meV, while a flat distribution, between $E_c - E = 0.35$ eV and $E_c - E = 0.7$ eV, corresponds to $E_0 = 5$ eV. The input parameters in the simulation are: $E_c - E_F = 0.6$ eV, $N_c = 10^{20} \text{ cm}^{-3}$, capture coefficient supposed temperature independent $c_n = 10^{-8} \text{ cm}^3 \text{ s}^{-1}$ ($v_0 = 10^{12} \text{ s}^{-1}$), $t_{rel} = 5$ min, $b = 0.032$ K/s, $T_0 = 90$ K, and $G_0 = 10^{20} \text{ cm}^{-3} \text{ s}^{-1}$ and a temperature-independent carrier lifetime τ_r or recombination time.

Fig. 6.1(a) presents simulation results showing the temperature dependence of excess (σ_{TSC}) and dark conductivity for different τ_r values, which vary between 2×10^{-4} s and 2×10^{-10} s. For a given τ_r , σ_{TSC} shows 3 different regions: initial rise at low temperature, a sharp drop at high temperature indicating that the thermal equilibrium is reached and a wide region between them which reveals a decrease and then a constant variation of σ_{TSC} . Furthermore, with τ_r increasing we observe that the different drops shift toward high temperatures.

The evaluation of the reconstructed TSC-DOS requires an effective attempt-to-escape frequency ν_{eff} according to Eq. (5.15). As a first attempt, ν_{eff} is determined after Fritzsche [31,32] under the condition $\sigma_{TSC} = \sigma_d$. Using σ_{TSC} values plotted in Fig. 6.1(a), TSC-DOS is calculated by application of Eq. (5.15) and Eq. (5.19) and plotted in Fig. 6.1(b).

The reconstructed TSC-DOS and the input-DOS in Fig. 6.1(b) reveal a discrepancy for $E_c - E < 0.4$ eV. The maximum of TSC-DOS here is significantly larger compared to the input-DOS taken at the same energy. For $E_c - E > 0.4$ eV, the TSC-DOS agree well with input one. However, for the TSC-DOS where $\tau_r \leq 2 \times 10^{-8}$ s, the energy range widely exceeds $E_c - E_F = 0.6$ eV. The corresponding ν_{eff} is 1 to 2 orders of magnitude larger than ν_0 , which corresponds to an unrealistic case.

Because of this discrepancy, ν_{eff} is determined when the simulated peak emission energy $E_{m,s}$ equals Fermi level E_F [104,105]. Using the temperature-dependent computed peak emission energy corresponding to each simulated TSC in Fig. 6.1(a), we determine the temperatures T_F such that $E_{m,s}(T_F) = E_F$.

An example is shown in Fig. 6.2 exhibiting $E_c - E_{m,s}$ and $E_c - E_F$ values over a range of temperatures from 90 K to 240 K. A distribution of trap states in the gap composed of 40 levels is used. As a result, the plot of $E_c - E_{m,s}$ against the temperature displays a steps form.

As has been already explained, from the condition $E_{m,s}(T_F) = E_F$, we graphically determine T_F in order to obtain ν_{eff} values. Because of the step form of $E_c - E_{m,s}$, the condition $E_{m,s}(T_F) = E_F$ is fulfilled with T_F variation of +3K leading to a variation of ν_{eff} between $1 \times 10^{12} \text{ s}^{-1}$ and $2 \times 10^{12} \text{ s}^{-1}$. A distribution with 160 levels allows a finer determination of T_F , with T_F variation of +1K. Therefore, the ν_{eff} value is more accurate, and is around $1 \times 10^{12} \text{ s}^{-1}$.

It is worth noting that, for each simulation in this chapter, we adopt a distribution of trap levels composed of 40 levels (because one simulation with 160 levels needs at least 5 hours).

In Fig. 6.3, the values of T_F obtained from the condition $E_{m,s}(T_F) = E_F$ are plotted with the corresponding σ_{TSC} . This plot is represented by star symbols. The figure indicates that when T_F increases, the star symbols shift progressively towards the point where σ_d and σ_{TSC} cross. Consequently two behaviours can be observed. The first, when T_F does not vary, $T_F = 210$ K, the second, when the star symbols shift progressively towards the point where σ_d crosses σ_{TSC} . T_F , here varies between 210 K and 253 K.

Figure 6.4 shows the results of ν_{eff} as a function of lifetime τ_r . The two trends are distinguished showing a constant ν_{eff} at short τ_r ($\tau_r \leq 2 \times 10^{-8}$ s) and a power law with power 1 at longer τ_r ($\tau_r \geq 2 \times 10^{-6}$ s). Consequently, two trapping regimes, weak ($\nu_{eff} \approx \nu_0$) and strong

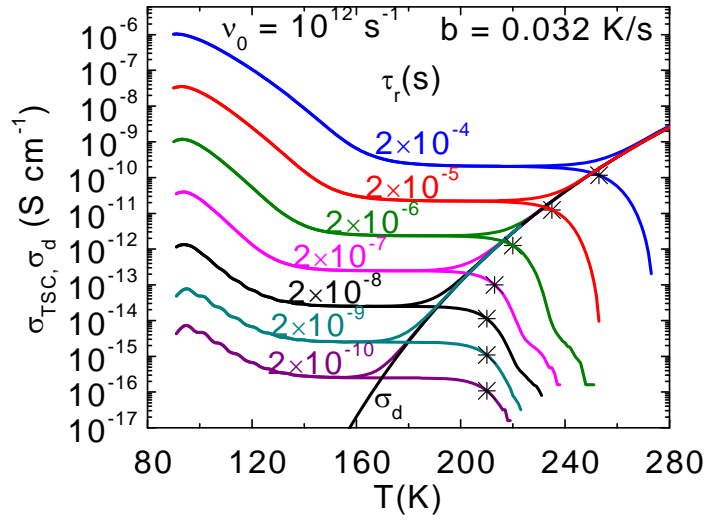


Figure 6.3: Temperature-dependent σ_{TSC} and σ_d by varying lifetime τ_r between 2×10^{-10} s and 2×10^{-4} s at constant heating rate $b = 0.032$ K/s. With star symbols, we show T_F temperatures and the corresponding σ_{TSC} , T_F is graphically obtained from $E_{m,s}(T_F) = E_F$.

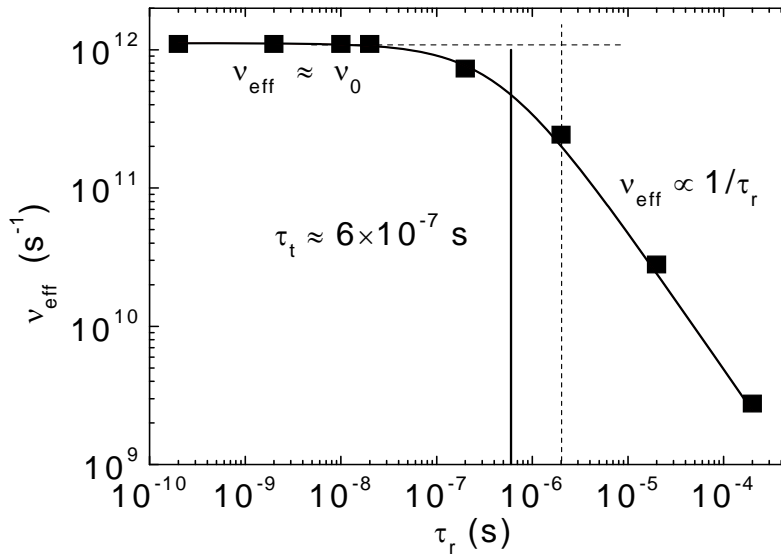


Figure 6.4: Lifetime-dependent simulated effective attempt-to-escape frequency v_{eff} exhibiting three distinct regions. Region with $\tau_r \geq 2 \times 10^{-6}$ s describes the strong retrapping regime where $v_{eff} \propto 1/\tau_r$; the region with $\tau_r \leq 2 \times 10^{-8}$ s describes the weak retrapping regime where $v_{eff} \approx \nu_0$. The intermediate region between them (2×10^{-8} s $< \tau_r < 2 \times 10^{-6}$ s), limited with dashed lines, describes the intermediate retrapping regime. It is noted that v_{eff} is calculated from Eq. 5.15. Good fit of v_{eff} values is shown with full line using Eq. (6.8). Consequently, τ_t is estimated around 6×10^{-7} s.

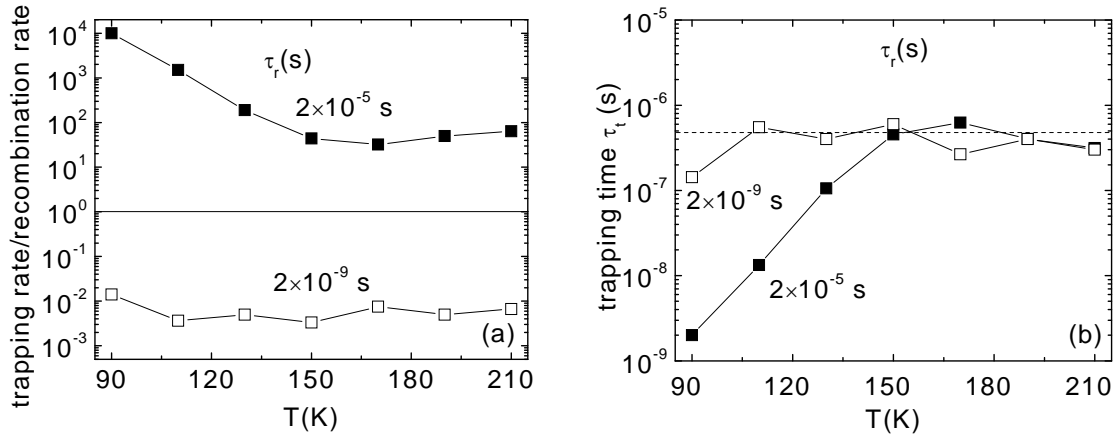


Figure 6.5: Retrapping rate to recombination rate for both cases where $\tau_r = 2 \times 10^{-5}$ s (strong retrapping) and $\tau_r = 2 \times 10^{-9}$ s (weak retrapping) (a). Corresponding retrapping time τ_t . The average value of $\tau_t = 5 \times 10^{-7}$ s is shown with the dashed line (b).

($v_{eff} < v_0$), are demonstrated. In addition, the region limited by 2×10^{-8} s and 2×10^{-6} s corresponds certainly to an intermediate retrapping regime between both regimes.

The ratio, recombination rate to the sum of retrapping rate and recombination rate informs us about the extent of strong retrapping regime. For this reason, the Equation (6.8) is suggested to quantify v_{eff} values

$$v_{eff} = v_0 \frac{\frac{1}{\tau_r}}{\frac{1}{\tau_t} + \frac{1}{\tau_r}} = v_0 \frac{\tau_t}{\tau_t + \tau_r} \quad (6.8)$$

The values of v_{eff} have been fitted using Eq. (6.8). The fit shown in Fig. 6.4 was obtained with $\tau_t = 6 \times 10^{-7}$ s. It should be mentioned that v_{eff} values are obtained at $T = T_F$, therefore the deduced fit parameter (τ_t) is also obtained at T_F .

The knowledge of the ratio $r(T)$ (retrapping rate to the recombination rate (Eq. 6.6)), allows the identification of the retrapping regime (strong or weak).

Using data simulation, temperature-dependent r and τ_t are evaluated into states within interval $3kT$ of $E_c - E_{m,s}$, and then plotted in Fig. 6.5 against the temperature for both cases : $\tau_r = 2 \times 10^{-5}$ s and $\tau_r = 2 \times 10^{-9}$ s.

In the case where $\tau_r = 2 \times 10^{-5}$ s, as illustrated in Fig. 6.5(a), r varies between 1×10^2 and 1×10^4 clearly showing the strong retrapping regime. However, strong variation in r is

observed at low temperatures below 150 K. This indicates that the carriers undergo the effect of release and trapping more strongly at low temperature. In addition, Fig. 6.5(b) shows that the retrapping time τ_t decreases rapidly when the temperature decreases. This is due to the presence of the conduction band tail in the input DOS. For $T > 150$ K, τ_t values vary slightly; therefore τ_t can be estimated around 5×10^{-7} s.

In contrast, in the case where $\tau_r = 2 \times 10^{-9}$ s, the ratio $r \ll 1$ varies between 1×10^{-3} and 7×10^{-3} over the whole range of temperatures showing clearly weak retrapping. In spite of the presence of conduction band tail, high values of r are not detected at low temperature. τ_t in Fig. 6.5(b) is around 5×10^{-7} s.

To get more information about strong and weak retrapping regimes, it is illustrative to know the occupation functions for both strong and weak retrapping regimes. By using Eq. (6.7), $f(E)$ is calculated and then plotted in Fig. 6.6.

Figure 6.6 displays the occupation functions f for the strong and weak retrapping regimes calculated for different temperatures between 90 K and at 230 K at 20 K intervals. Fig. 6.6(a) shows f in the case of weak retrapping where $\tau_r = 2 \times 10^{-9}$ s. At given temperature and at high energy, f drops sharply. Closer to E_c , the distribution is Boltzmann-like and proportional to $\exp(E_c - E/kT)$. The dashed lines indicate the extrapolations if the occupation functions were in quasi-equilibrium. The derived values of $E_c - E_q$, according to Eq. 6.2, are larger than $E_c - E_{m,s}$. The difference between them becomes progressively smaller when the temperature increases to T_F for which the thermal equilibrium is reached. For $T = 130$ K, the quasi-Fermi level $E_c - E_q = 0.43$ eV, whereas $E_c - E_{m,s} = 0.38$ eV. Fig. 6.6(b) displays f for strong retrapping for $\tau_r = 2 \times 10^{-5}$ s. Here, f is proportional to $\exp(E_c - E/kT)$ for the shallower states. At $T = 130$ K, the quasi-Fermi level $E_c - E_q = 0.295$ eV corresponds to $f = 0.5$, which illustrates the quasi-Fermi distribution. Besides, the values of $E_c - E_q$ and $E_c - E_{m,s}$ are similar.

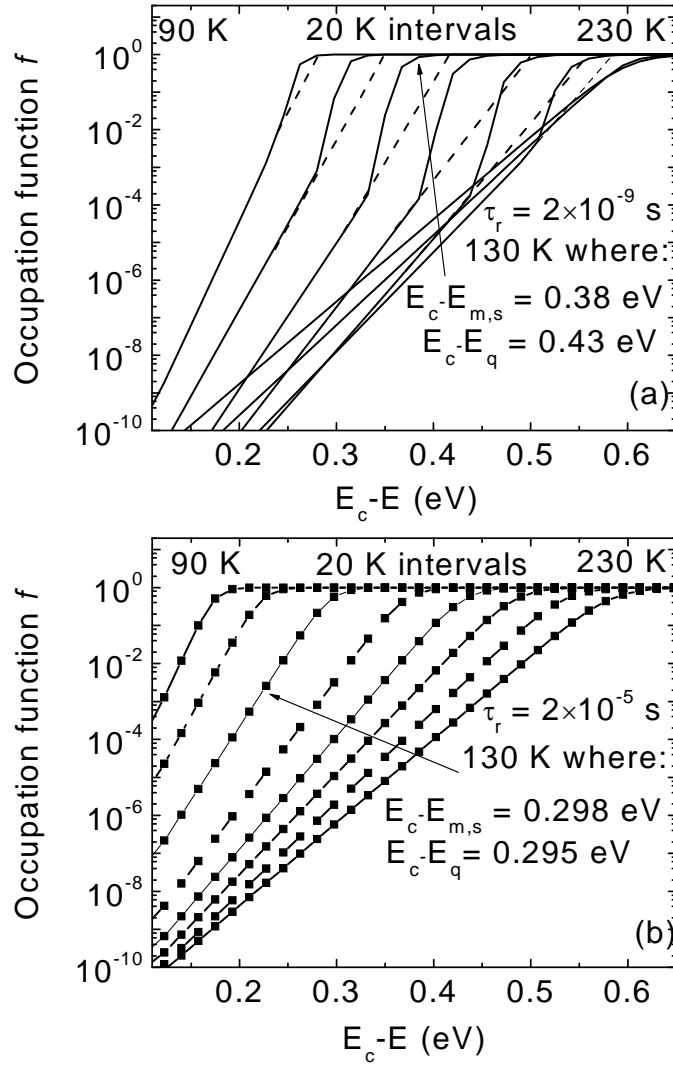


Figure 6.6: Occupation function f determined for different temperature between 90 K and 230 K at 20 K intervals for the cases of weak (a) and strong (b) re trapping. Because of the sharp slope in f , f is not Boltzmann-like. The dashed lines represent the extrapolation of f from low to high energy if f was Boltzmann-like. An example of f is shown at $T = 130$ K, hence $E_c - E_q = 0.43$ eV and $E_c - E_{m,s} = 0.38$ eV (a). For strong re trapping where $\tau_r = 2 \times 10^{-5}$ s, f is Boltzmann-like. An example of f is shown at $T = 130$ K, hence $E_c - E_q = 0.298$ eV and $E_c - E_{m,s} = 0.295$ eV.(b).

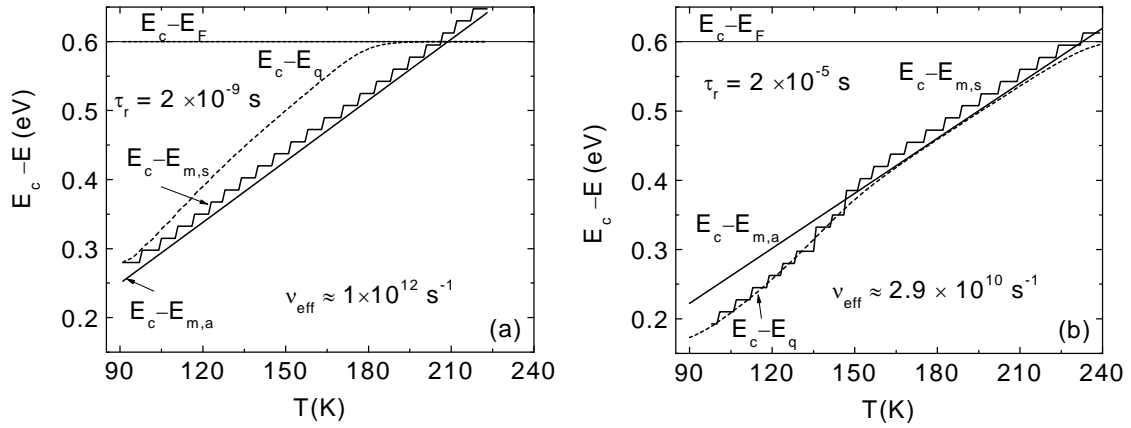


Figure 6.7: Temperature-dependent computed ($E_c - E_{m,s}$) and analytical ($E_c - E_{m,a}$) peak emission energy, quasi-Fermi level $E_c - E_q$ and $E_c - E_F$ in the cases of weak retrapping where $\tau_r = 2 \times 10^{-9}$ s (a), and strong retrapping where $\tau_r = 2 \times 10^{-5}$ s (b).

The energy $E_c - E_{m,s}$ represents the maximum TSC emission energy either for weak or strong retrapping. This energy, $E_c - E_{m,s}$, is given from the simulation. Now, it is important to know which equation could reproduce the energy data of $E_c - E_{m,s}$ and thus describe strong or weak retrapping. For this reason, $E_c - E_{m,a}$ according to Schmidt (Eq. 5.15), $E_c - E_{m,s}$, and $E_c - E_q$ (Eq. 6.2) are plotted in Fig. 6.7 in the case of strong retrapping ($\tau_r = 2 \times 10^{-5}$ s) and weak retrapping ($\tau_r = 2 \times 10^{-9}$ s).

In Figure 6.7(a), $E_c - E_{m,s}$ and $E_c - E_{m,a}$ are very similar, whereas $E_c - E_q$ reveals a pronounced discrepancy essentially at high temperatures. As a result, the energy scale $E_c - E_{m,a}$ perfectly reproduces the data of the simulation in the weak retrapping regime.

In contrast, in Fig. 6.7(b), $E_c - E_{m,s}$ and $E_c - E_q$ are similar over the whole range of temperatures between 90 K and 230 K; except for a very small region above 230 K where the thermal equilibrium is reached. However, $E_c - E_{m,a}$ reveals a strong discrepancy at low temperatures. Thus, $E_c - E_q$, in this work, is suggested to be considered as the energy scale in the strong retrapping case in order to evaluate the DOS.

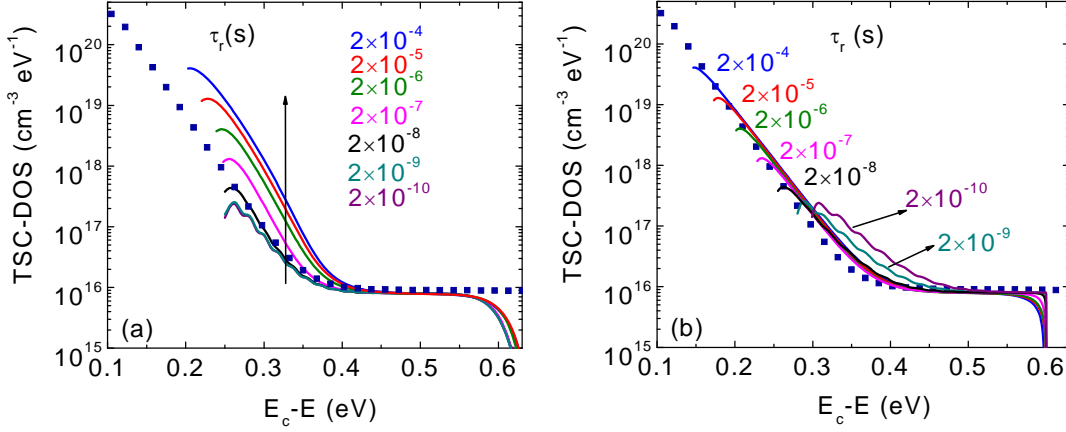


Figure 6.8: Reconstructed TSC-DOS with variation lifetime τ_r ($2 \times 10^{-10} \text{ s} < \tau_r < 2 \times 10^{-4} \text{ s}$).

- (a) $E_c - E_{m,a}$ is regarded as the energy scale. The vertical arrow shows the increase of τ_r from bottom to top. The reconstructed TSC-DOS for $\tau_r = 2 \times 10^{-9} \text{ s}$ and $\tau_r = 2 \times 10^{-10} \text{ s}$ are similar.
- (b) $E_c - E_q$ is regarded as the energy scale. A disagreement with input and reconstructed TSC-DOS appears only for $\tau_r = 2 \times 10^{-9} \text{ s}$ and $\tau_r = 2 \times 10^{-10} \text{ s}$.

Figure 6.8 displays the application of these concepts on the simulated TSC data of Fig. 6.3. The TSC-DOS is evaluated by application of Eq. (5.19) using v_{eff} values obtained at T_F and calculated by application of Eq. 5.15. Two energy scales $E_c - E_{m,a}$ and $E_c - E_q$ are taken into account.

In Fig. 6.8(a) with $E_c - E_{m,a}$, a discrepancy is observed between the input DOS and the TSC-DOS at low energy only for the cases of strong retrapping with long lifetimes. However, the related conduction band tail calculated from reconstructed TSC-DOS is comparable to $E_0 = 23 \text{ meV}$. Good agreement is observed between the input and the reconstructed DOS in the case of weak retrapping. The cut-off of the TSC-DOS at $E_c - E_F$ is clearly observed. However, it slightly exceeds the $E_c - E_F = 0.6 \text{ eV}$ value. This is due to the presence of unoccupied states in an energy interval of about $2kT_F$ for $E_c - E > E_c - E_F$.

Fig. 6.8(b) displays a good agreement in the TSC-DOS for $\tau_r \geq 2 \times 10^{-8} \text{ s}$, where $E_c - E_q$ is taken as the energy scale. Poor agreement is found for the TSC-DOS with $\tau_r = 2 \times 10^{-10} \text{ s}$ and $\tau_r = 2 \times 10^{-9} \text{ s}$. In addition, we observe that the TSC-DOS drops abruptly at $E_c - E_F = 0.6 \text{ eV}$, ignoring the presence of unoccupied defect lying in the range $E_c - E > 0.6 \text{ eV}$. This is undoubtedly due to the weakness of $E_c - E_q$ used as the energy scale.

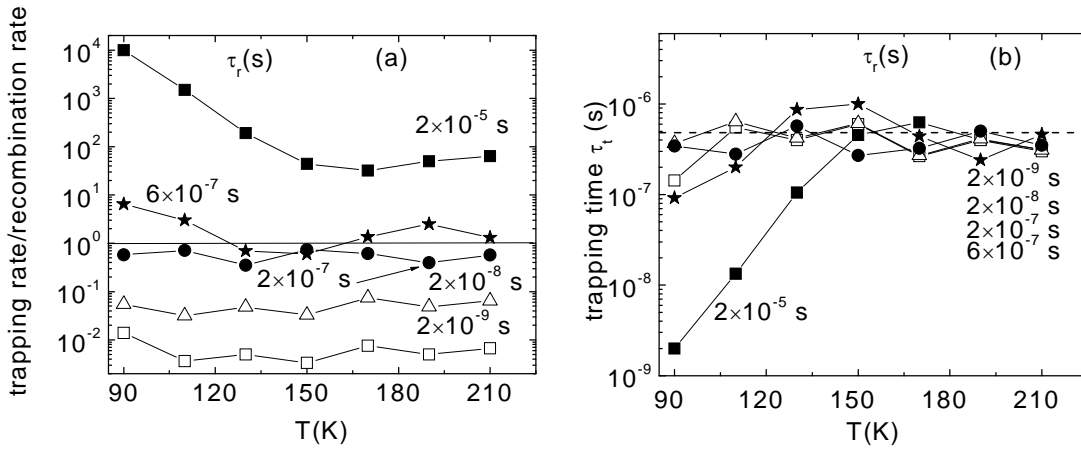


Figure 6.9: Retrapping rate to recombination rate for the cases where τ_r varies between 2×10^{-9} s and 2×10^{-5} s (a). Corresponding retrapping time τ_t . With the dashed line we show the average value of τ_t (b).

Furthermore, strong discrepancy is detected between input and reconstructed DOS for the case $\tau_r = 2 \times 10^{-10}$ s and $\tau_r = 2 \times 10^{-9}$ s.

The ratio r , can now be calculated not only for the cases $\tau_r = 2 \times 10^{-9}$ s and $\tau_r = 2 \times 10^{-5}$ s, but also for the whole range of τ_r showing the intermediate region between strong and weak retrapping.

Figure 6.9(a) shows that the increase of τ_r also leads to an increase of the ratio r when τ_r is between 2×10^{-9} s and 2×10^{-5} s.

The intermediate retrapping regime is defined when $\tau_r/\tau_t \approx 1$. Above, $\tau_t = 6 \times 10^{-7}$ s is determined from Eq. 6.8. To check this value, a simulation is done for $\tau_r = 6 \times 10^{-7}$ s. Figure 6.9(a) displays the corresponding ratio r against the temperature represented with star symbols. For $T < 120$ K, r is larger than 1 and reaches the value 6.52 for $T = 90$ K. Strong retrapping is detected in this region. For $T > 120$ K, r is around 1 indicating the presence of an intermediate retrapping regime. The corresponding τ_t is around 5×10^{-7} s. This shows that the calculated value of τ_t using Eq. 6.8 is quite reasonable to describe the intermediate retrapping regime. In addition, for the case $\tau_r = 2 \times 10^{-7}$ s we observe that $r \leq 1$. The corresponding τ_t is also around 5×10^{-7} s (Fig. 6.9(b)). Thus we can consider that σ_{TSC} obtained from $\tau_r = 2 \times 10^{-7}$ s also belongs to the intermediate retrapping regime.

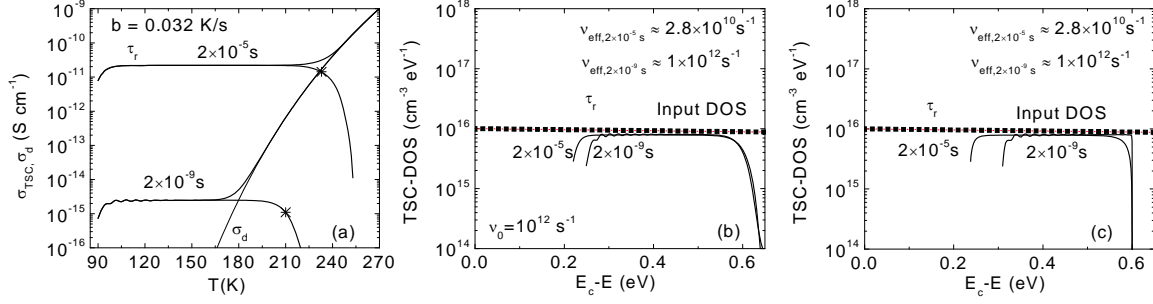


Figure 6.10: Temperature-dependent simulated TSC and dark conductivity obtained from a flat density of states for $\tau_r = 2 \times 10^{-9}$ s and $\tau_r = 2 \times 10^{-5}$ s. The star symbols correspond to the temperature T_F where $E_{m,s}(T_F) = E_F$ is fulfilled (a). Corresponding TSC-DOS in the case where $E_c - E_{m,a}$ is regarded as energy scale (b) and $E_c - E_q$ as energy scale (c).

B. Input DOS = flat distribution of the DOS

Now we propose to examine strong and weak retrapping regimes using as input DOS only a flat distribution of $16 \text{ cm}^{-3} \text{ eV}^{-1}$. The constant DOS extends from E_c to $E_c - E = 0.7 \text{ eV}$. $E_c - E_F$ is located in the gap at 0.6 eV , $c_n = 10^{-8} \text{ cm}^3 \text{ s}^{-1}$ ($\nu_0 = 10^{12} \text{ s}^{-1}$).

Fig. 6.10(a) displays the simulation results showing temperature-dependent simulated TSC and dark conductivity corresponding to two different carrier lifetimes $\tau_r = 2 \times 10^{-9}$ s and $\tau_r = 2 \times 10^{-5}$ s. Under the condition $E_{m,s}(T_F) = E_F$, T_F is determined and plotted with star symbols. Therefore two different ν_{eff} are calculated according to Eq. (5.15): $\nu_{eff} \approx 10^{12} \text{ s}^{-1}$ for $\tau_r = 2 \times 10^{-9}$ s and $\nu_{eff} \approx 2.8 \times 10^{10} \text{ s}^{-1}$ for $\tau_r = 2 \times 10^{-5}$ s. In spite of the absence of a conduction band tail, the evidence of weak ($\nu_{eff} \approx \nu_0$) and strong ($\nu_{eff} < \nu_0$) retrapping is again reported.

Fig. 6.10(b) and Fig. 6.10(c) show the corresponding TSC-DOS where two different energy scales $E_c - E_{m,a}$ and $E_c - E_q$ are considered respectively. TSC-DOS for $\tau_r = 2 \times 10^{-5}$ s in Fig. 6.10(b) and Fig. 6.10(c) are almost similar. The difference between them lies in the region where TSC-DOS drops sharply [see Fig. 6.10(c)] and at the onset of TSC-DOS showing a slight extension of TSC-DOS to low energy in the case where $E_c - E_{m,a}$ is considered as the energy scale [Fig. 6.10(b)]. However, for $\tau_r = 2 \times 10^{-9}$ s, the difference in TSC-DOS between Fig. 6.10(b) and Fig. 6.10(c) is distinctly observed especially at low energies.

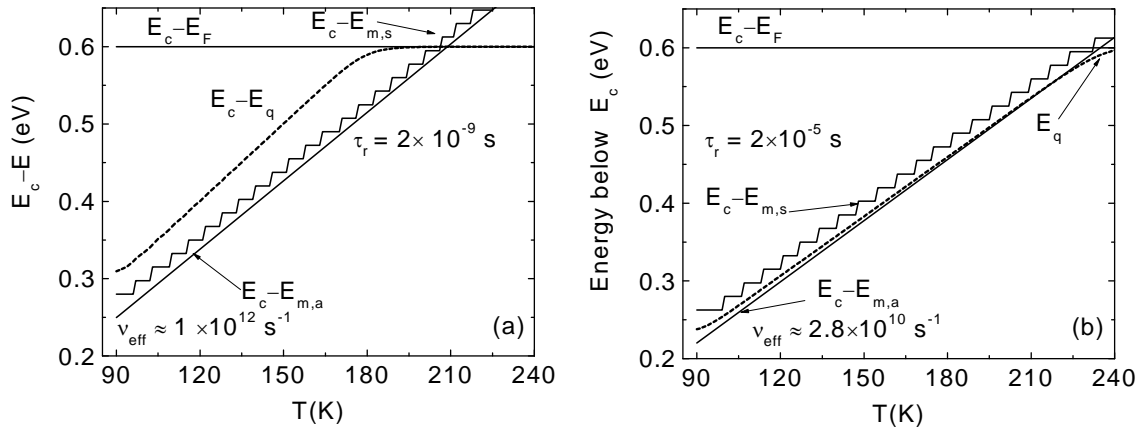


Figure 6.11: Temperature-dependent computed ($E_c - E_{m,s}$) and analytical ($E_c - E_{m,a}$) peak emission energy, quasi-Fermi level $E_c - E_q$ and $E_c - E_F$ obtained using as input DOS a constant distribution. Two cases are considered: $\tau_r = 2 \times 10^{-9}$ s (weak retrapping) (a) and $\tau_r = 2 \times 10^{-5}$ s (strong retrapping) (b).

Fig. 6.11(a) shows that $E_c - E_{m,a}$ nicely reproduces the simulated data of $E_c - E_{m,s}$. However $E_c - E_q$ and $E_c - E_{m,s}$ reveal a disagreement in the case of weak retrapping. This disagreement leads to a shift of the onset of the TSC-DOS to high energy where many states caused by the use of $E_c - E_q$ as the energy scale are not taken into account.

In contrast, in the case of strong retrapping, $E_c - E_{m,s}$, $E_c - E_{m,a}$ and $E_c - E_q$ display a good agreement [Fig. 6.11(b)]. This explains the similarity of TSC-DOS observed for $\tau_r = 2 \times 10^{-5}$ s in Fig. 6.10(b) and Fig. 6.10(c). Therefore, $E_c - E_{m,a}$ or $E_c - E_q$ could be used as the energy scale for a flat density of states in the case of strong retrapping.

6.2.2 Discussion

The simulation results in Fig. 6.1(a) show σ_{TSC} for a model DOS for different lifetime τ_r between 2×10^{-4} s and 2×10^{-10} s. An increase of τ_r systematically involves an increase in σ_{TSC} . This is due to the increased contribution of free carriers in conduction band for high values of τ_r . One also could be expect a transition from weak to strong recombination as τ_r is varied over such a wide range.

The condition $\sigma_{TSC} = \sigma_d$ given by Fritzsche [31,32], in the case of strong retrapping has been applied in order to get v_{eff} and then to evaluate the density of states. The results in Fig. 6.1(b) show a significant discrepancy between input and reconstructed DOS, especially for σ_{TSC} obtained from short lifetime τ_r values. This can be explained in the following way: the v_{eff} parameter is introduced because of a delay in E_m reaching E_F . If the delay is significant, strong retrapping is expected leading to smaller values of v_{eff} with respect to v_0 . In contrast, if the delay is insignificant, v_{eff} is of the same order of magnitude as v_0 , i.e., describing thus the case of weak retrapping. In Fig. 6.1(b) for $\tau_r \leq 2 \times 10^{-8}$ s, calculated values of v_{eff} are overestimated ($v_{eff} > v_0$), which is the unrealistic result. Consequently, the false values of v_{eff} involve a shift of the TSC-DOS to high energy causing firstly a discrepancy between reconstructed and input DOS and secondly a false ‘TSC drop’ which lies in an energetic range $E_c - E > 0.65$ eV. In addition, even for $\tau_r \geq 2 \times 10^{-6}$ s where the retrapping dominates over the recombination, a discrepancy is also observed between introduced and calculated DOS (Fig. 6.1(b)).

To address these problems, the condition $E_{m,s}(T_F) = E_F$ is instead applied to get the T_F values, found graphically, and then to calculate v_{eff} values [104,105] by applying Eq. (5.15).

It has been observed that T_F coincides with the point $\sigma_{TSC} = \sigma_d$ in the case of strong retrapping, however in the case of weak retrapping T_F lies in the region $\sigma_{TSC} \ll \sigma_d$.

Thus the shift of the σ_{TSC} ‘drops’ to higher temperature for longer τ_r values is a consequence of the delay in E_c reaching E_F caused by multiple trapping in the strong retrapping regime, and leads to reduced values for v_{eff} .

It is worth pointing out that the above simulation confirms the application of $\sigma_{TSC} = \sigma_d$ condition proposed by Fritzsche in the case for strong retrapping. However the discrepancy detected in the range $\tau_r \geq 2 \times 10^{-6}$ s between reconstructed and input DOS in Fig. 6.1(b) is due

to the choice of the energy scale. More comments will be offered later about this discrepancy. Furthermore, in the literature there is no relationship relating σ_{TSC} to σ_d in the case of the weak retrapping regime. In this work, the condition $\sigma_{TSC} \ll \sigma_d$ is found, indicative of weak retrapping, in order to get T_F and then to evaluate v_{eff} values.

From the calculated values of v_{eff} in Fig. 6.4, the evidence for the weak and strong retrapping regime is demonstrated. Also, the intermediate retrapping region is deduced where $2 \times 10^{-8} \text{ s} < \tau_r < 2 \times 10^{-6} \text{ s}$.

Equation 6.8 is proposed to fit the simulated values of v_{eff} in Fig. 6.4. A good fit is shown leading to a value of retrapping time $\tau_t = 6 \times 10^{-7} \text{ s}$, obtained at T_F .

For comparison the retrapping time τ_t is calculated at T_F by applying Eq. (6.9) introduced in reference [104]. The equation is given by

$$\tau_t = \frac{1}{c_n g(E_m) kT} \Big|_{T=T_F} . \quad (6.9)$$

From Eq. (6.9), τ_t is around $5 \times 10^{-7} \text{ s}$. A difference of 16% is shown between Eqs. (6.8) and (6.9). This confirms the validity of the proposed equation (Eq. (6.8)).

The occupation functions in Fig. 6.6(a) and Fig. 6.6(b) for different temperatures, reveal that an increase in the temperature eventually leads to the redistribution of trapped carriers over available trap states until finally thermal equilibrium. However, different behaviours are observed in f when the retrapping regime is strong or weak. For example, the occupation function f in Fig. 6.6(a) for $\tau_r = 2 \times 10^{-9} \text{ s}$ (weak retrapping) is not Boltzmann-like because of the sharp drop of f at $E_c - E_{m,s}$. Strong recombination locates $E_c - E_q$ below $E_c - E_{m,s}$ causing thus the ‘jump’ in f at $E_c - E_{m,s}$. On the other hand, strong retrapping reveals a distribution which is Boltzmann-like (Fig. (6.6(b))). $E_c - E_{m,s}$ and $E_c - E_q$ in this regime are similar. Thus it could be noted that the position of $E_c - E_q$ with respect to $E_c - E_{m,s}$ is an indicator of the nature of the retrapping regime.

Using the concentration of trapped carriers at time t and at the temperature T , as well as the concentration of traps obtained from the simulation of σ_{TSC} at given lifetime τ_r , the retrapping time is calculated into states within interval $3kT$ of $E_{m,s}$ according to $\tau_t = \sum_i c_n (N_i - n_i)$. Therefore by calculating the right-hand side of Eq. (6.6), the ratio r , retrapping rate to recombination rate, is deduced for each temperature. r . Indeed, in Fig. 6.5(a) r is much larger than 1 in the case where $\tau_r = 2 \times 10^{-5} \text{ s}$ showing thus a dominant retrapping

regime, whereas r is much smaller than 1 for $\tau_r = 2 \times 10^{-9}$ s showing a strong recombination. τ_t in both cases is estimated around 5×10^{-7} s. Only one difference is detected at low temperatures in the case of strong retrapping ($\tau_r = 2 \times 10^{-5}$ s) where τ_t becomes very small (Fig. 6.5(b)). This means that the presence of the conduction band in this case amplifies the effect of retrapping.

We recall that τ_t equals 6×10^{-7} s is obtained from Eq. 6.8. A simulation has been done and added in Fig 6.9(a) by taking $\tau_r = 6 \times 10^{-7}$ s in order to check the related retrapping regime. As a result the average value of r is around 1. Consequently, σ_{TSC} obtained from $\tau_t = \tau_r = 6 \times 10^{-7}$ s is related to an intermediate retrapping.

In summary, τ_t is evaluated from 3 different methods: from Eqs. 6.8, 6.9 and from the ratio r . The results show that the methods converge to a value of τ_t which lies between 5×10^{-7} s and 6×10^{-7} s.

In Fig. 6.7(a), the energy scale $E_c - E_{m,a}$ obtained from Eq. (5.15) displays a good overlap with $E_c - E_{m,s}$ in the weak retrapping regime case ($\tau_r = 2 \times 10^{-9}$ s). Furthermore in Fig. 6.8 (a) and in the case of weak retrapping ($\tau_r \leq 2 \times 10^{-8}$ s and $v_{eff} \approx v_0$), the reconstructed density of states evaluated by taking $E_c - E_{m,a}$ as the energy scale exhibit a good agreement with input DOS. Besides, the exceeding of TSC-DOS of $3kT$ of $E_c - E_F$ is due to the contribution of unoccupied states in the range $E_c - E_F > 0.6$ eV. Consequently from the simulation, the validity of the Eqs. 5.15 and 5.19 given by Schmidt [103] in the case of the weak retrapping regime are verified.

In Fig. 6.7(b) where $\tau_r = 2 \times 10^{-5}$ s (strong retrapping), a disagreement at low temperatures is shown between $E_c - E_{m,s}$ and $E_c - E_{m,a}$ indicating that $E_c - E_{m,a}$ can not be used as the energy scale, whereas, we observe that $E_c - E_{m,s}$ and $E_c - E_q$ are similar. We suggested to consider $E_c - E_q$ as the energy scale in the case for strong retrapping in order to evaluate DOS. This suggestion is quite reasonable because the corresponding densities of states in Fig. 6.8(b) agree very well with the input DOS in the case of strong retrapping.

In contrast, in Fig. 6.8(b), the density of states for $\tau_r < 2 \times 10^{-8}$ s exhibits strong discrepancy with input DOS. This is because $E_c - E_q$ taken as energy scale is not suitable to describe the weak retrapping regime. An analogue reasoning is valid for the reconstructed DOS corresponding to strong retrapping in Fig. 6.8(a) and showing a discrepancy with input DOS.

Consequently, $E_c - E_{m,a}$ proposed in the literature [103] as the energy scale in the case of strong retrapping is not consistent with our simulation. The quasi Fermi level $E_c - E_q$ in this case is shown to be a suitable parameter to establish the energy scale determining TSC-DOS. However $E_c - E_{m,a}$ is considered as the energy scale for weak retrapping regime.

In Fig. 6.10, a flat density of states without conduction band tail is examined for 2 values of τ_r : $\tau_r = 2 \times 10^{-9}$ s and $\tau_r = 2 \times 10^{-5}$ s. We showed from the obtained value of ν_{eff} that the corresponding σ_{TSC} belongs to weak and strong retrapping. The reconstructed density of states for both cases are evaluated using $E_c - E_{m,a}$ and then $E_c - E_q$ as energy scales (Fig. 6.10(b) and Fig. 6.10(c)).

The energies $E_c - E_{m,s}$ and $E_c - E_q$ in the case of strong retrapping in Fig. 6.11(b) are similar. However, the expected discrepancy found in the first simulation between $E_c - E_{m,s}$ and $E_c - E_{m,a}$ in Fig. 6.7(b) has disappeared. This is due to the absence of conduction band tail. This means $E_c - E_q$ or $E_c - E_{m,a}$ could be used as the energy scale in the case of strong retrapping when the conduction band tail does not exist. Indeed, Zhu [94] calculated $E_c - E_{m,a}$ and $E_c - E_q$ by using a DOS which is almost flat. As a result a slight difference was detected between $E_c - E_{m,a}$ and $E_c - E_q$.

Furthermore we show that $E_c - E_q$ taken as the energy scale in the case of weak retrapping can not be considered, because the states at low energy are not probed (Fig. 6.10(c)). The discrepancy between $E_c - E_q$ and $E_c - E_{m,s}$ in 6.11(a) confirms the poor choice of $E_c - E_q$ as energy scale in this regime.

We can conclude that the suggestion to use $E_c - E_q$ as energy scale in the case of strong retrapping is significant and also necessary, essentially in the case where a conduction band tail is taken into account.

In summary, the strong and weak retrapping as well as the intermediate retrapping regimes have been demonstrated in this section. We have also shown that ν_{eff} parameter could be determined, in the case for weak and strong retrapping, via 2 different conditions: $\sigma_{TSC} \ll \sigma_d$ and $\sigma_{TSC} = \sigma_d$ respectively.

Different criteria allowing the identification of the retrapping regime nature have been studied. These criteria are:

- Ratio r (retrapping rate to recombination rate): $r < 1$: weak retrapping
 $r > 1$: strong retrapping
 $r \approx 1$: intermediate retrapping

- The equation: $\tau_t = \frac{1}{c_n \text{DOS}(E_m) kT}$: $\tau_t \gg \tau_r$: weak retrapping
 $\tau_t \ll \tau_r$: strong retrapping
 $\tau_t \sim \tau_r$: intermediate retrapping

- ν_{eff} parameter determination: $\nu_{eff} \ll \nu_0$: weak retrapping
 $\nu_{eff} = \nu_0$: strong retrapping
 $\nu_{eff} \approx 0.7 \nu_0$: intermediate retrapping

- $E_{m,s}$, $E_{m,a}$, and E_q determination for comparison: $E_{m,s} \approx E_{m,a}$: weak retrapping
 $E_{m,s} \approx E_q$: strong retrapping
(except for a flat DOS where: $E_{m,s} \approx E_q \approx E_{m,a}$)

- Occupation function f : f is not Boltzmann-like distribution: weak retrapping
 f is Boltzmann-like distribution: strong retrapping

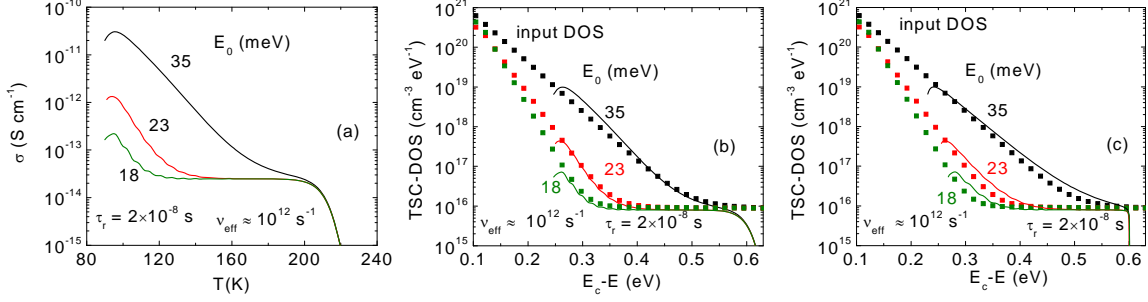


Figure 6.12: Temperature-dependent simulated TSC obtained from three different band tail parameters: 35 meV, 23 meV and 18 meV. $\tau_r = 2 \times 10^{-8} \text{ s}$ and $\nu_0 = 10^{12} \text{ s}^{-1}$ are kept constant (a). Corresponding TSC-DOS in the case where $E_c - E_{m,a}$ is regarded as energy scale (b) and $E_c - E_q$ as energy scale (c).

6.2.3 Band tail parameter variation

In this section we will focus our studies on an eventual change of the retrapping regime nature by varying the conduction band tail parameter E_0 . We start with the same input DOS proposed in the first part of section 6.2.1, i.e. conduction band tail followed with a flat density of states.

The simulation is performed with the parameter such that $\tau_r = 2 \times 10^{-8} \text{ s}$, $\nu_0 = 10^{12} \text{ s}^{-1}$ ($c_n = 10^{-8} \text{ cm}^3 \text{ s}^{-1}$). Only E_0 is varied taking 3 different values: 35 meV, 23 meV and 18 meV. The simulated σ_{TSC} , obtained with $E_0 = 23 \text{ meV}$, has already been investigated above (section 6.2.1) and corresponds to the weak retrapping regime.

Fig. 6.12(a) displays the simulated results showing the temperature-dependent simulated TSC conductivity. An increase of E_0 also leads to an increase of σ_{TSC} . In addition, the flat region of σ_{TSC} disappears progressively with increasing E_0 . The ‘TSC drop’ at high temperature is the same for the 3 simulations with $E_0 = 23 \text{ meV}$ and $E_0 = 18 \text{ meV}$ and $E_0 = 35 \text{ meV}$. This leads to the same value of $\nu_{\text{eff}} (\approx 10^{12} \text{ s}^{-1})$.

Figures 6.12(b) and 6.12(c) display the reconstructed TSC-DOS where $E_c - E_{m,a}$ and $E_c - E_q$ are considered as energy scale respectively. With increasing E_0 the flat DOS of the reconstructed TSC-DOS progressively disappears.

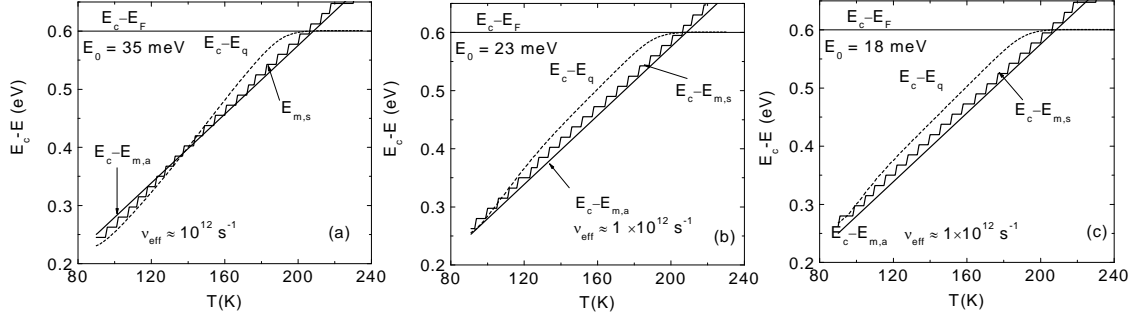


Figure 6.13: Temperature-dependent computed ($E_c - E_{m,s}$) and analytical ($E_c - E_{m,a}$) peak emission energy, quasi-Fermi level $E_c - E_q$ and $E_c - E_F$ obtained when $E_0 = 35$ meV (a), $E_0 = 23$ meV and $E_0 = 18$ meV (c).

Figure 6.12(b) reveals a good agreement between the reconstructed and input DOS in the case where $E_0 = 18$ meV over the whole range of temperatures. In contrast, a poor overlap is detected especially in the range $E_c - E < 0.4$ eV for TSC-DOS with $E_0 = 35$ meV, while for $E_c - E > 0.4$ eV, the reconstructed and input DOS agree well.

In Figure 6.12(c), where $E_c - E_q$ is taken as the energy scale, the reconstructed TSC-DOS with $E_0 = 18$ meV shows an insufficient agreement with input DOS. However, in contrast to the Figure 6.12(b), the good agreement is detected when $E_c - E < 0.4$ eV for TSC-DOS with $E_0 = 35$ meV. To better understand this behavior a plot of $E_c - E_{m,s}$, $E_c - E_{m,a}$ and $E_c - E_q$ is presented in Fig. 6.13.

Figure 6.13(a), where $E_0 = 35$ meV, reveals that neither $E_c - E_q$ or $E_c - E_{m,a}$ can correctly reproduce the $E_c - E_{m,s}$ value over the whole range of temperatures between 90 K and 240 K. Indeed, $E_c - E_{m,s}$ and $E_c - E_{m,a}$ at high temperatures are similar, while at low temperatures below 150 K, $E_c - E_{m,s}$ and $E_c - E_q$ show a good agreement. This clearly explains the insufficient agreement between reconstructed and input DOS for $E_0 = 35$ meV in Fig. 6.12(b) and Fig. 6.12(c).

Fig. 6.13(c) shows a good agreement between $E_c - E_{m,s}$ and $E_c - E_{m,a}$ leading to the good agreement observed in Fig. 6.12(b) between reconstructed TSC-DOS and input DOS with $E_0 = 18$ meV.

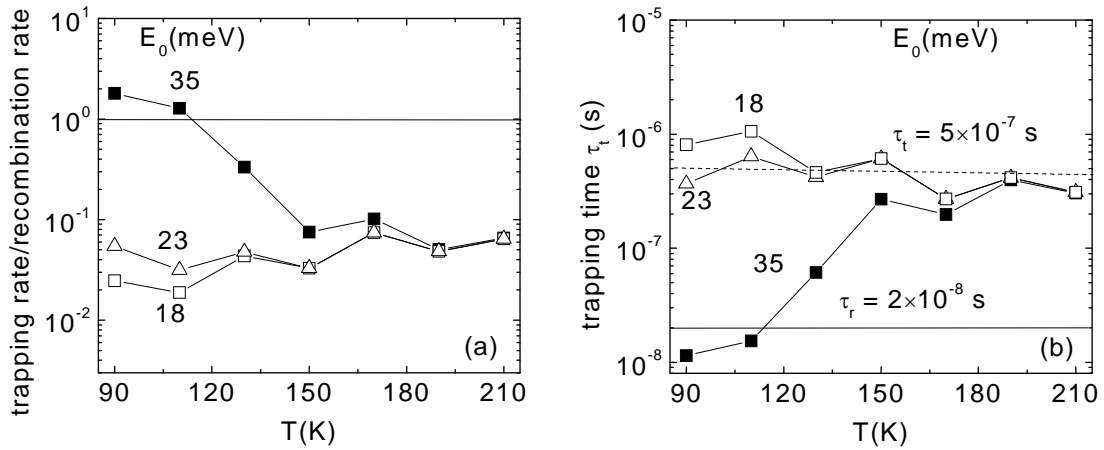


Figure 6.14: The ratio r (retrapping rate to recombination rate) for the cases where $E_0 = 35$ meV, 23 meV and 18 meV (a). Corresponding retrapping time τ_t . With the dashed line we show the average value of τ_t (b).

The comparison of the ratio r , retrapping rate to recombination rate against the temperature, is presented in Fig. 6.14(a). In the case where $E_0 = 18$ meV, r is between 10^{-1} and 10^{-2} indicating weak retrapping. The retrapping time τ_t in the whole range is around 5×10^{-7} s (see Fig. 6.14(b)). However, for the case $E_0 = 35$ meV, r is around 10^{-1} for $T > 150$ K. For $T < 150$ K, r increases and reaches the value 1.8. The corresponding retrapping time τ_t in Fig. 6.14(b) decreases at low temperature and exceeds the value $\tau_r = 2 \times 10^{-8}$ s. Therefore, the strong retrapping regime is reached and lies in a small range of temperatures below 120 K. At high temperatures τ_t approaches the value 5×10^{-7} s.

Discussion

In summary, with increasing E_0 , σ_{TSC} increases; this is due to the strong emission of released carriers from the traps. In addition, it could be observed that the width of the TSC peak at low temperature increases with increasing E_0 .

In the case where $E_0 = 35$ meV, strong retrapping regime is detected at low temperatures ($T < 120$ K), while weak retrapping regime is observed at high temperatures ($T < 120$ K). In addition an insufficient agreement between $E_c - E_{m,s}$ and $E_c - E_{m,a}$, and $E_c - E_{m,s}$ and $E_c - E_q$ is observed.

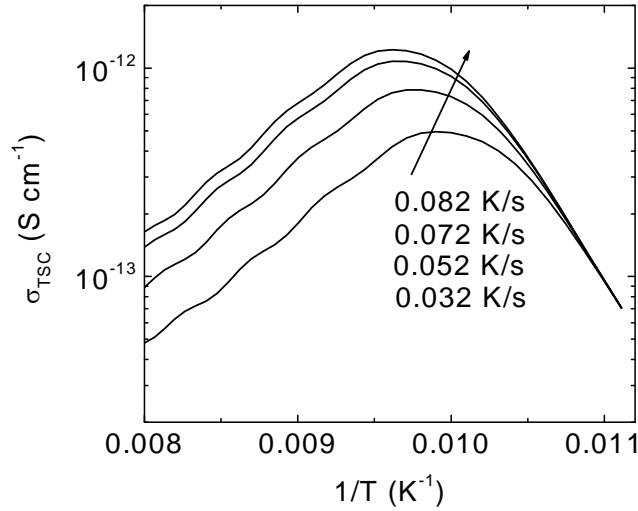


Figure 6.15: σ_{TSC} against inverse temperature obtained by varying heating rate b from 0.032 K/s to 0.082 K/s. $E_0 = 23$ meV, $\tau_r = 2 \times 10^{-8}$ s, $\tau_{rel} = 30$ min and $T_0 = 90$ K are kept constant.

6.2.4 Heating rate variation

To get more information about the TSC characteristics (initial rise at low temperature, ‘TSC drop’) different simulations are performed by varying the heating rate b . We use the same input DOS given in section 6.2.1 with $\tau_r = 2 \times 10^{-8}$ s (weak retrapping regime).

Figure 6.15 displays different σ_{TSC} , at low temperatures, obtained from different heating rates b between 0.032 K/s and 0.082 K/s. The figure reveals a common initial rise of σ_{TSC} until 0.0106 K^{-1} , which could be described with straight line. Furthermore we observe that the σ_{TSC} maximum at T_m moves to higher temperatures with increasing b ; T_m in this case, varies between 101 K and 104 K. The height of the peak also increases. Before to get the corresponding TSC-DOS, let us discuss the origin of the low-temperature peak.

Initial rise

By applying Bezemer’s approach described in the chapter 5, we will show that the presence of the low temperature peak is mainly caused by the product between the Boltzmann tail of f_0 and the term $(\mu\tau)_ng(E)$. For this reason, an exponential function proportional to $\exp(E/E_{oc})$ with $E_{oc} = kT_{oc}$, is chosen to describe the DOS $g(E)$ in Eq. (5.13). Therefore we get:

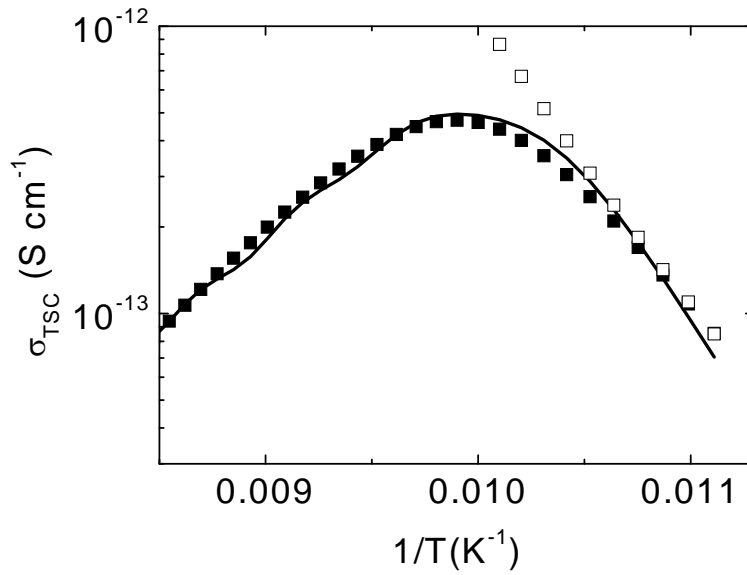


Figure 6.16: σ_{TSC} against inverse temperature obtained with a heating rate $b = 0.032$ K/s and $\tau_{rel} = 30$ min. The full line represents the data from the simulation, full symbols represent the calculated data from Eq. (6.10) and Eq. (6.11) and open symbols represent the calculated data from Eq. (6.14).

$$\sigma_{TSC} \propto f_0(E_m)(\mu\tau)_n \exp\left(-\frac{E_c - E_m}{kT_{oc}}\right) \quad (6.10)$$

and
$$E_c - E_m = kT \ln(52\nu/b) - 0.017\text{eV} \quad (6.11)$$

with
$$f_0(E_m) = \left(1 + \exp\left(\frac{E_m(T) - E_q(T_0)}{kT_0}\right)\right)^{-1} \quad (6.12)$$

In the case where $E_c - E_m < E_c - E_q$ we get $1 \ll \exp\left(\frac{E_m - E_q}{kT_0}\right)$, Eq. (6.12) becomes:

$$f_0(T) = \exp\left(-\frac{E_m(T) - E_q}{kT_0}\right) \propto \exp\left(\frac{E_c - E_m(T)}{kT_0}\right) \propto (52\nu/b)^{\frac{T}{T_0}} \quad (6.13)$$

It should be noted that the Eq. (6.13) is valid only for $E_m - E_q > kT_0$ where T_0 is equal to 90 K.

Using Eqs. (6.10), (6.11) and (6.13) σ_{TSC} is expressed by:

$$\sigma_{TSC} \propto (\mu\tau)_n (52\nu/b)^{T\left(\frac{1}{T_0} - \frac{1}{T_{oc}}\right)} \quad (6.14)$$

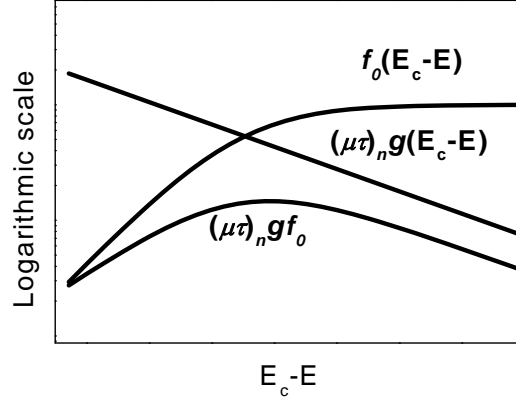


Figure 6.17: Sketch of the initial rise showing the distribution function $f_0(E_c - E)$ and $(\mu\tau)_n g(E_c - E)$ whose product gives the initial rise of $\sigma_{TSC} \approx (\mu\tau)_n g(E) f_0$.

In the case where $T_0 < T_{oc}$, we expect, from Eq. (6.14), that an increase of T leads to an increase of σ_{TSC} . In this case ($E_c - E_m < E_c - E_q$), an agreement between simulated and calculated σ_{TSC} (Eq. 6.14) is achieved only for the first values of T ($90 \text{ K} < T < 96 \text{ K}$, open symbol in Fig. 6.16). The best fit is obtained using Eq. (6.10) and Eq. (6.11) without any approximation. Eq. (6.14) only provides a qualitative approximation of the initial rise of σ_{TSC} . Fig. 6.16 shows the σ_{TSC} data obtained from the simulation (full line) and calculated data (square symbol) from Eq. (6.10) and Eq. (6.11). The low-temperature peak (initial rise) is very well reproduced when $T_{oc} = 267 \text{ K}$ ($E_0 = 22 \text{ meV}$), $T_0 = 90 \text{ K}$ and $\tau_r = 2 \times 10^{-8} \text{ s}$.

In order to get a better understanding of the initial rise of σ_{TSC} , a sketch given by Fritzsche [31] is reproduced in Fig. 6.17.

Fritzsche clearly shows that the initial rise is strongly related to the initial distribution $f_0(E)$ at T_0 . $f_0(E)$ in Fig. 6.17 exhibits 2 regions: initial rise $f_0 < 1$ and quasi steady state where $f_0 \approx 1$.

Figure 6.18(a) displays σ_{TSC} against the temperature for various b between 0.032 K/s and 0.082 K/s . For each b , v_{eff} is determined at T_F according to Eq. 5.15. It has been observed that at each star symbol in Fig. 6.18(a), the condition $\sigma_{TSC} = 0.02\sigma_d$ is fulfilled.

Figure 6.18(b) reveals the corresponding TSC-DOS. We can observe that the TSC – DOS do not change when b is varied.

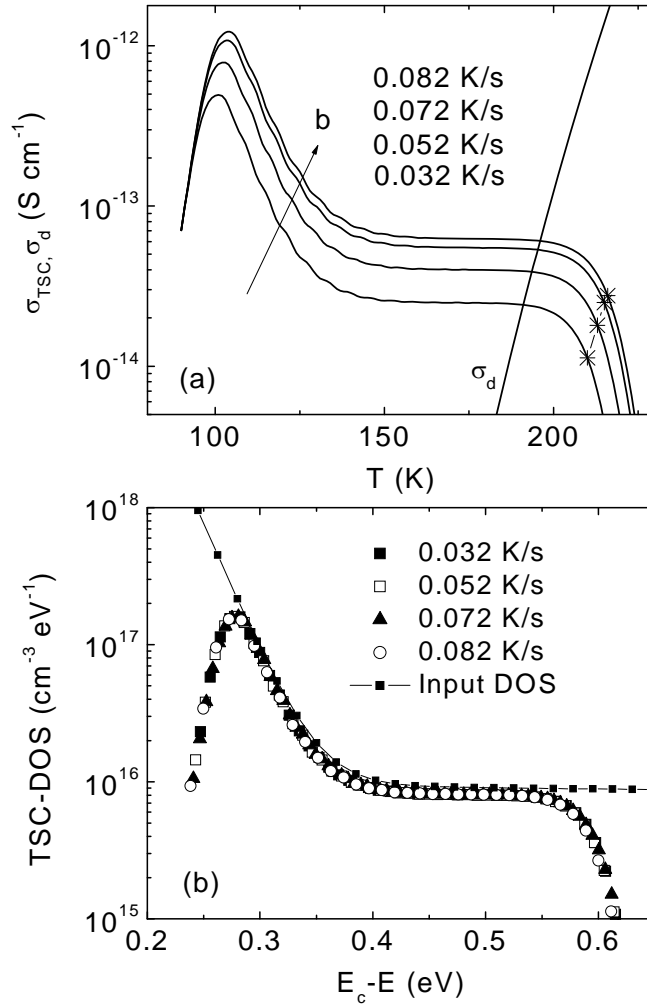


Figure 6.18: Temperature-dependent simulated TSC obtained by varying heating rate b from 0.032 K/s to 0.082 K/s. $E_0 = 23$ meV, $\tau_r = 2 \times 10^{-8}$ s, $\tau_{rel} = 30$ min and $T_0 = 90$ K are kept constant. Star symbol indicates the temperature T_F where v_{eff} is calculated (a). Corresponding TSC-DOS obtained by application of Eqs. (5.19) and (5.15) (b).

Discussion

It is shown that the presence of low-temperature peak of TSC (Fig. 6.16) is due to the product of the exponential decay of DOS and the Boltzmann tail of the occupation function $f_0(T_0)$ which increases rapidly when E_m moves more deeply to the gap.

With increasing b , the peak in Figure 6.18(a) at T_m shifts to high temperatures. From an analytical calculation, Simmons found the same behaviour [87,88]. Furthermore, the change of the peak in height is attributed to an increase of the carrier emission rate (see Eq. 5.3). In addition the results show that v_{eff} could also be determined for other σ_{TSC} if the ratio

σ_{TSC}/σ_d at T_F is known for only one σ_{TSC} . Activation energy equal to the Fermi level is obtained using values of σ_{TSC} represented by star symbols (Fig. 6.18(a)). The TSC-DOS in Figure 6.18.(b) does not vary with increasing the heating rate b . This result is consistent because the density of states should not depend on the experimental parameters.

6.2.5 Capture coefficient variation

A. Simulation with $\tau_r = 2 \times 10^{-8}$ s

In this section strong and weak retrapping regimes are investigated by varying the capture coefficient c_n or ν_0 . We recall that $\nu_0 = c_n N_c$ ($N_c = 10^{20} \text{ cm}^{-3}$ is the effective density of states). For this reason, we consider the same input density of states given in the first part of section 6.2.1 with $\tau_r = 2 \times 10^{-8}$ s and $E_c - E_F = 0.6$ eV and $E_0 = 23$ meV.

The case where $c_n = 10^{-8} \text{ cm}^3 \text{ s}^{-1}$ is already studied and the corresponding σ_{TSC} is related to a weak retrapping regime. Three additional simulations have been achieved with: $c_n = 10^{-9} \text{ cm}^3 \text{ s}^{-1}$, $c_n = 10^{-7} \text{ cm}^3 \text{ s}^{-1}$ and then $c_n = 10^{-6} \text{ cm}^3 \text{ s}^{-1}$.

Figure 6.19(a) shows simulated TSC. The results reveal that the decrease in c_n implies a slight increase in σ_{TSC} at low temperatures for $T < 140$ K. However, for $T > 140$ K and before the 'TSC drop', σ_{TSC} is c_n -independent. Besides different 'TSC drops', are observed when c_n is varied. The drop shifts towards low temperatures with increasing c_n (or ν_0).

Figure 6.19(b) and Figure 6.19(c) display the reconstructed DOS by using the simulated σ_{TSC} shown in Fig. 6.19(a). Also in this study two energy scales are taken into account $E_c - E_{m,a}$ and $E_c - E_q$. Input and reconstructed TSC-DOS agree fairly in Fig. 6.19(b) for the cases where $c_n = 10^{-9} \text{ cm}^3 \text{ s}^{-1}$ and $c_n = 10^{-8} \text{ cm}^3 \text{ s}^{-1}$. This good agreement confirms the use of $E_c - E_{m,a}$ as energy scale in the case of weak retrapping regime. However a poor overlap is shown for $c_n = 10^{-7} \text{ cm}^3 \text{ s}^{-1}$ and $c_n = 10^{-6} \text{ cm}^3 \text{ s}^{-1}$.

In contrast, by considering $E_c - E_q$ as energy scale in Fig. 6.19(b), TSC-DOS disagree with the input DOS for $c_n = 10^{-9} \text{ cm}^3 \text{ s}^{-1}$ and $c_n = 10^{-8} \text{ cm}^3 \text{ s}^{-1}$. Besides, a good overlap is shown for the case $c_n = 10^{-7} \text{ cm}^3 \text{ s}^{-1}$ and $c_n = 10^{-6} \text{ cm}^3 \text{ s}^{-1}$.

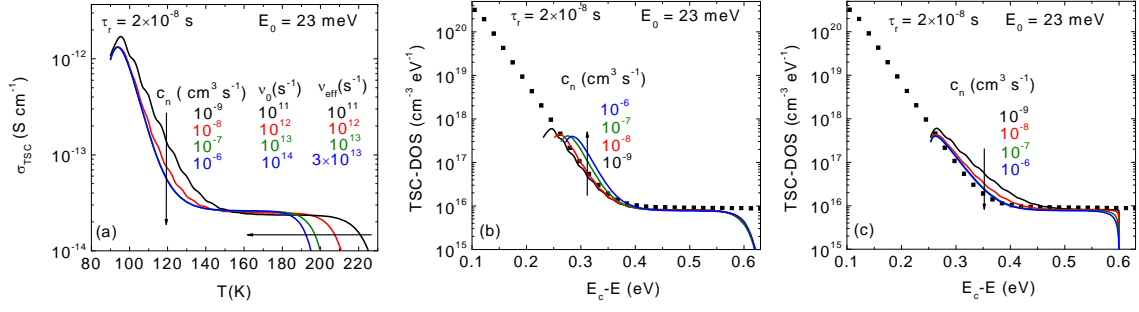


Figure 6.19: Simulated TSC obtained from 4 different capture coefficients c_n (or 4 different ν_0): 10^{-6} $\text{cm}^3 \text{s}^{-1}$, 10^{-7} $\text{cm}^3 \text{s}^{-1}$, 10^{-8} $\text{cm}^3 \text{s}^{-1}$ and 10^{-9} $\text{cm}^3 \text{s}^{-1}$. $E_0 = 23$ meV and $\tau_r = 2 \times 10^{-8}$ s are kept constant. The calculated ν_{eff} is shown. Vertical and horizontal arrows indicate the increase of c_n from top to bottom and from right to left respectively (a). Corresponding TSC-DOS in the case where $E_c - E_{m,a}$ is regarded as the energy scale. The vertical arrow indicates the increase of c_n from bottom to top (b). The corresponding TSC-DOS in the case where $E_c - E_q$ is considered as the energy scale. Here, the vertical arrow indicates the increase of c_n from top to bottom (c).

The values of ν_{eff} are determined for each σ_{TSC} when thermal equilibrium is reached: $E_{m,s} = E_F$. In addition, referring to Eq. (6.9), retrapping time τ_t at T_F is evaluated. ν_{eff} and τ_t values are summarized in Table 6.1.

Table 6.1 reveals an increase of ν_{eff} when ν_0 increase because the retrapping time τ_t decreases. ν_{eff} and ν_0 are similar for $c_n = 10^{-9}$ $\text{cm}^3 \text{s}^{-1}$ and $c_n = 10^{-8}$ $\text{cm}^3 \text{s}^{-1}$. In addition the corresponding τ_t is 100 and 10 orders of magnitude longer than τ_r respectively. This clearly indicates that the retrapping regime nature corresponds to weak retrapping.

| c_n ($\text{cm}^3 \text{s}^{-1}$) | ν_0 (s^{-1}) | ν_{eff} (s^{-1}) | τ_t (s) |
|---------------------------------------|-----------------------------|---------------------------------|----------------------|
| 10^{-9} | 10^{11} | 10^{11} | 5.2×10^{-6} |
| 10^{-8} | 10^{12} | 10^{12} | 5.5×10^{-7} |
| 10^{-7} | 10^{13} | 0.8×10^{13} | 5.8×10^{-8} |
| 10^{-6} | 10^{14} | 3×10^{13} | 6.0×10^{-9} |

Table 6.1: ν_{eff} and τ_t values calculated for each σ_{TSC} in Fig. 6.19(a) for carrier lifetime $\tau_r = 2 \times 10^{-8}$ s.

In contrast, for $c_n = 10^{-7} \text{ cm}^3 \text{ s}^{-1}$, τ_t and τ_r values are comparable and ν_{eff} values show slight decrease. The corresponding σ_{TSC} belongs to intermediate retrapping regime. For the last case where $c_n = 10^{-6} \text{ cm}^3 \text{ s}^{-1}$, τ_t is smaller than τ_r and the value of $\nu_{eff} = 3 \times 10^{13} \text{ s}^{-1}$ is smaller than $\nu_0 = 10^{14} \text{ s}^{-1}$. In this case a strong retrapping of carriers is obvious.

Discussion

In summary, an invariance of σ_{TSC} , for $T > 140 \text{ K}$ and before the TSC drops, is observed over a large range of c_n between $10^{-6} \text{ cm}^3 \text{ s}^{-1}$ and $10^{-9} \text{ cm}^3 \text{ s}^{-1}$, respectively. This is due to the flat input DOS in this region. However, an increase of σ_{TSC} for $T < 140 \text{ K}$ is detected when c_n decrease (Fig. 6.19(a)). This is related to the decrease of ν_{eff} which is certainly due to a delay of $E_{m,s}$ to reach E_F caused by stronger concentration of released carriers. In this section the transition from weak to strong retrapping is achieved.

B. Simulation with $\tau_r = 2 \times 10^{-5} \text{ s}$

Here we examine the effect of the c_n variation on the retrapping regime by considering a long lifetime $\tau_r = 2 \times 10^{-5} \text{ s}$. Two additional simulations have been done applying the same input DOS used in section 6.2.1. Also all other parameters like τ_r , $E_c - E_F$ and E_0 are kept the same, only c_n is varied: $c_n = 10^{-9} \text{ cm}^3 \text{ s}^{-1}$ (triangle symbol), $c_n = 10^{-8} \text{ cm}^3 \text{ s}^{-1}$ (circle symbol) and $10^{-7} \text{ cm}^3 \text{ s}^{-1}$ (full line).

Figure 6.20(a) displays temperature-dependent simulated TSC showing that σ_{TSC} is c_n independent. ν_{eff} value ($2.8 \times 10^{10} \text{ s}^{-1}$) is the same for the 3 simulations.

Furthermore, according to Eq. (6.9), τ_t is calculated for the 3 simulations such that: $\tau_t = 5 \times 10^{-6} \text{ s}$ for $c_n = 10^{-9} \text{ cm}^3 \text{ s}^{-1}$ ($\nu_0 = 10^{11} \text{ s}^{-1}$), $\tau_t = 5 \times 10^{-7} \text{ s}$ for $c_n = 10^{-8} \text{ cm}^3 \text{ s}^{-1}$ ($\nu_0 = 10^{12} \text{ s}^{-1}$) and $\tau_t = 5 \times 10^{-8} \text{ s}$ for $c_n = 10^{-7} \text{ cm}^3 \text{ s}^{-1}$ ($\nu_0 = 10^{13} \text{ s}^{-1}$).

For each simulation, τ_t is shorter than $\tau_r = 2 \times 10^{-5} \text{ s}$. Therefore strong retrapping is expected. Figure 6.20(b) displays the reconstructed TSC-DOS corresponding to Fig. 6.20(a). A good overlap is shown with input DOS emphasising once again the strong retrapping regime by using $E_c - E_q$ as energy scale.

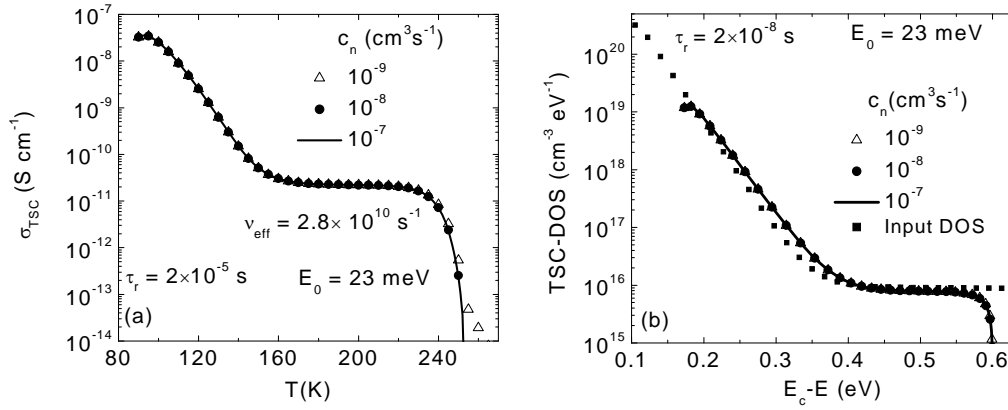


Figure 6.20: Temperature-dependent simulated TSC obtained from three different capture coefficients c_n (or ν_0): $10^{-9}\ cm^3\ s^{-1}$ (triangle symbol), $10^{-8}\ cm^3\ s^{-1}$ (circle symbol), $10^{-7}\ cm^3\ s^{-1}$ (full line). $E_0 = 23\ meV$ and $\tau_r = 2 \times 10^{-5}\ s$ are kept constant (a). Corresponding TSC-DOS in the case where $E_c - E_q$ is regarded as the energy scale (b).

Discussion

In summary, σ_{TSC} is very slightly affected by a c_n variation. Indeed, ν_{eff} value, for 3 simulations is smaller than ν_0 showing thus a dominant retrapping with respect to recombination. Besides, the invariance of σ_{TSC} as well as the TSC-DOS by varying c_n (Fig. 6.20) indicates that the transition to weak retrapping regime is not possible. This is due to a high value of τ_r with respect to the values τ_t ($\tau_t \ll \tau_r$). That means to reach a weak retrapping regime, the parameter c_n must be smaller than $10^{-9}\ cm^3\ s^{-1}$.

6.2.6 T-dependent carrier lifetime

In the above studies, the characteristic features of strong and weak retrapping regimes have been investigated through a TSC simulation where the carrier lifetime τ_r is assumed to be temperature independent. In this section, we consider the same input DOS given in section 6.2.1. The other input parameters are not changed; only the temperature-dependent carrier lifetime $\tau_r(T)$ is varied. We propose to describe $\tau_r(T)$ with an exponential function such that: $\tau_r(T) \sim 10^{-5} \exp(-10^3 K^{-1}/T) s$. The three simulations have been carried out in Fig. 6.21(a) for 3 different $\tau_r(T)$: $1 \times \tau_r(T)$, $10 \times \tau_r(T)$ and $100 \times \tau_r(T)$.

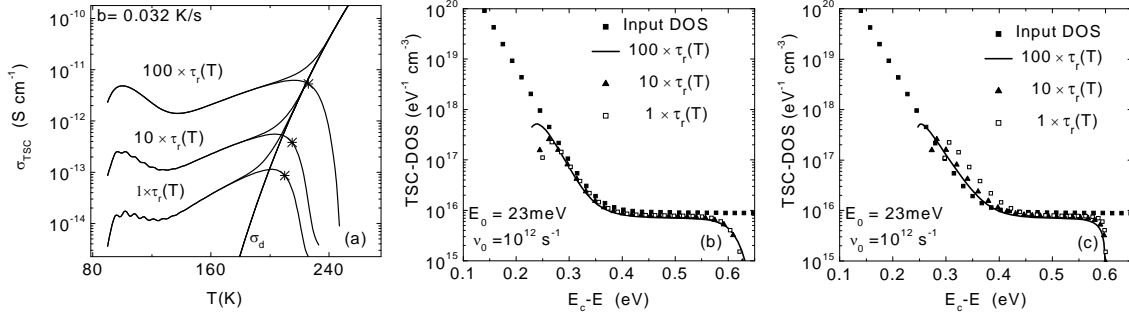


Figure 6.21: Temperature-dependent simulated TSC obtained from three T-dependent lifetimes: $\tau_r(T)$, $10 \times \tau_r(T)$ and $100 \times \tau_r(T)$. $E_0 = 23$ meV and $\nu_0 = 10^{12}$ s $^{-1}$ are kept constant. With the star symbols we show the temperature T_F at which $E_{m,s}(T_F) = E_F$ is fulfilled. (a). Corresponding TSC-DOS in the case where $E_c - E_{m,a}$ is regarded as energy scale (b) and $E_c - E_q$ as energy scale (c).

With increasing τ_r , σ_{TSC} increases showing different ‘TSC drops’ which progressively shifts towards high temperatures. The temperature T_F at which E_m reaches E_F is evaluated for each σ_{TSC} and plotted against the corresponding $\sigma_{TSC}(T_F)$ with star symbols. Fig. 6.21(a) reveals a gradual shift of the star symbols towards the point where σ_{TSC} and σ_d cross. This behaviour has been already observed in section 6.2.1 where τ_r is temperature independent. It can be seen that for the simulation with $100 \times \tau_r(T)$, T_F is found at $\sigma_{TSC} = \sigma_d$, whereas for that with $1 \times \tau_r(T)$, T_F is found at $\sigma_{TSC} \ll \sigma_d$.

Using the T_F value determined for each σ_{TSC} , ν_{eff} is evaluated according to Eq. (5.15). $\nu_{eff} = 10^{12}$ s $^{-1}$ for σ_{TSC} with $\tau_r = 1 \times \tau_r(T)$, $\nu_{eff} = 0.7 \times 10^{12}$ s $^{-1}$ for σ_{TSC} with $\tau_r = 10 \times \tau_r(T)$ and $\nu_{eff} = 10^{11}$ s $^{-1}$ for σ_{TSC} with $100 \times \tau_r(T)$.

Figure 6.21(b) and Fig. 6.21(c) exhibit the reconstructed DOS considering $E_c - E_{m,a}$ and $E_c - E_q$ as energy scale respectively. The input DOS agrees with the reconstructed DOS for $\tau_r = 1 \times \tau_r(T)$ and $\tau_r = 10 \times \tau_r(T)$ in Fig. 6.21(b). A same drop of DOS at high energy is observed. Good agreement is observed in Fig. 6.21(b) and Fig. 6.21(c) for $\tau_r = 100 \times \tau_r(T)$.

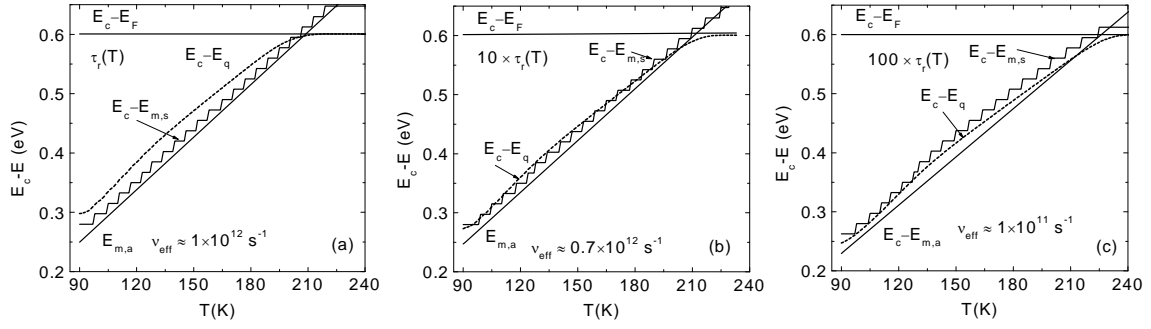


Figure 6.22: Temperature-dependent computed ($E_c - E_{m,s}$) and analytical ($E_c - E_{m,a}$) peak emission energy, quasi-Fermi level $E_c - E_q$ and $E_c - E_F$ obtained for $1 \times \tau_r(T)$ (a), $10 \times \tau_r(T)$ (b) and $100 \times \tau_r(T)$ (c).

To get more information a plot of $E_c - E_{m,s}$, $E_c - E_{m,a}$ and $E_c - E_q$ is shown in Fig. 6.22 for each τ_r . $E_c - E_{m,s}$, $E_c - E_{m,a}$ agree well for $\tau_r = 1 \times \tau_r(T)$ in Fig. 6.22(a). Besides, it can be seen that the agreement of the 3 energy scales is acceptable in Fig. 6.22(b) for $\tau_r = 10 \times \tau_r(T)$. However, for $\tau_r = 100 \times \tau_r(T)$, Fig. 6.22(c) reveals a good overlap between $E_c - E_{m,s}$, and $E_c - E_q$ whereas, $E_c - E_{m,s}$, $E_c - E_{m,a}$ disagree.

The retrapping regime is also determined by calculating the ratio r , retrapping rate to recombination rate, by applying Eq. (6.6). The ratio r is plotted in Fig. 6.23(a) against the temperature for the three σ_{TSC} . For $\tau_r(T) = 1 \times \tau_r(T)$, r is between 10^{-3} and 0.28, whereas r is between 10^{-1} and 1.4 for $\tau_r(T) = 10 \times \tau_r(T)$ exceeding slightly $r = 1$. For $\tau_r(T) = 100 \times \tau_r(T)$, r is between 4 and 13. Fig. 6.23(b) exhibits the corresponding retrapping time τ_r . For $\tau_r(T) = 100 \times \tau_r(T)$, τ_r is calculated using Eq. (6.9) for comparison. At low temperatures, a variation of about 50% is detected between data obtained from Eq. (6.6) and Eq. (6.9).

Discussion

The variation of τ_r from $1 \times \tau_r(T)$ to $100 \times \tau_r(T)$ in Fig. 6.21(a) involves an increase of σ_{TSC} . The different drops which shift at high temperatures are due to the delay of $E_{m,s}$ to reach E_F .

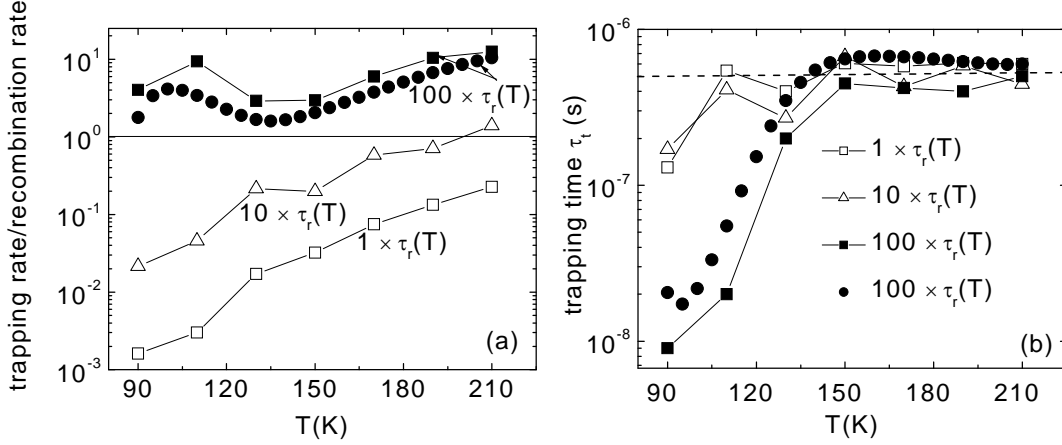


Figure 6.23: Retrapping time to recombination time, r , for $\tau_r(T)$, $10 \times \tau_r(T)$ and $100 \times \tau_r(T)$ by applying Eq. (6.6). With the circle symbol, $r = \tau_r/\tau_t$ is calculated using Eq. (6.9) (a). Corresponding retrapping time τ_t . τ_t (circle symbol) is obtained from Eq. (6.9). With the dashed line we show the average value of τ_t at high temperatures (b).

Consequently v_{eff} decreases with increasing τ_r . The comparison with $\nu_0 = 10^{12} \text{ s}^{-1}$ and v_{eff} allows to determine the retrapping regime nature. In the first case where $\tau_r = 1 \times \tau_r(T)$, ν_0 and v_{eff} are similar; the ratio r is smaller than 1 and the comparison between input and reconstructed DOS shows a good agreement in Fig. 6.21(b). Consequently, the related σ_{TSC} corresponds to the weak retrapping regime. For $\tau_r = 100 \times \tau_r(T)$, v_{eff} is smaller than ν_0 , r is much higher than 1. This implies that σ_{TSC} is described with the strong retrapping regime. However, a slight decrease of v_{eff} is observed for $\tau_r(T) = 10 \times \tau_r(T)$. At high temperatures, r exceeds the 1 value in Fig. 6.23(a). This feature shows that the corresponding σ_{TSC} can only be described with an intermediate retrapping regime. In contrast to the case where τ_r is temperature independent in section 6.2.1, both $E_c - E_q$, and $E_c - E_{m,a}$ could be considered as energy scales for the intermediate retrapping-regime case. We can conclude that, in this case, the transition from weak to strong retrapping regime (intermediate retrapping regime) is shown if we consider the 3 simulations. Only, it is difficult to make a difference between intermediate and weak retrapping regime when τ_r approaches $\tau_r = 10 \times \tau_r(T)$. Furthermore, an acceptable agreement is shown between the application of Eq. 6.6 and Eq. 6.9 which determine τ_t .

6.3. Conclusion

Detailed investigation of the strong and weak retrapping as well as the intermediate regime is reported via the simulation of thermally stimulated current (TSC). Different parameters have been varied in order to gain more information about the trapping regime. Criteria have been obtained allowing the identification of strong and weak retrapping. The validity of Schmidt's approach has been shown in the case of weak retrapping. However, for strong retrapping, the quasi Fermi level $E_c - E_q$ has been shown to be suitable parameter to establish the energy scale of the TSC-DOS. The condition $\sigma_{TSC} = \sigma_d$ proposed by Fritzsche to get the effective attempt-to-escape ν_{eff} values has been verified. However, from the simulation the exploitation of the range $\sigma_{TSC} \ll \sigma_d$ has been proposed in order to obtain ν_{eff} values in the case of the weak retrapping regime. Furthermore, the initial rise of TSC from simulation data has been reproduced using Bezemer's approach.

The variation of parameters such as heating rate b does not effect on the retrapping regime. However, with increasing the band tail parameter, the intermediate retrapping regime has been reached. It has been observed that the variation of the capture coefficient over a large range does not affect the strong retrapping regime.

Chapter 7

Experimental and simulated results of TSC for the weak retrapping regime

This chapter presents the experimental and simulated results of TSC measurements performed on a microcrystalline sample with low crystalline volume fraction R_c . The first part of this chapter deals with the determination of the retrapping regime related to this sample by applying the different criteria investigated in section 6.2. It is worth noting that a support of a TSC simulation is necessary to determine the DOS in the gap as well as the traps parameters such as conduction band tail parameter, capture coefficient and retrapping time. The DOS in the different sections is evaluated from Schmidt's approach, except for the section 7.1.3 where Landweer and Bezemer approach is applied for comparison.

It should be noted that the potential of the TSC technique is clearly shown through the results in the sections 7.1, 7.2 and 7.3. In contrast, the limits as well as the assumptions, under which the DOS has been evaluated, are addressed in the end of the sub-section 7.3.4.

The second part focusses on the investigation of the experimental parameter variation during TSC measurements such as constant heating rate b , initial temperature T_0 , relaxation time t_{rel} and photogeneration rate G_0 . The aim of this section is to study the effect of the variation of the experimental parameters on the retrapping regime nature as well as on the DOS.

Finally, the last part of this chapter deals with the origin of the initial rise of the TSC curve at low temperature.

7.1 TSC for $\mu\text{c-Si:H}$ with $R_c = 34\%$

The $\mu\text{c-Si:H}$ film studied in this section is characterized by a crystalline volume fraction R_c of about 34%. We note that the parameters W and h of the sample are 0.5 mm and 10 mm respectively (more information can be found in chapter 3).

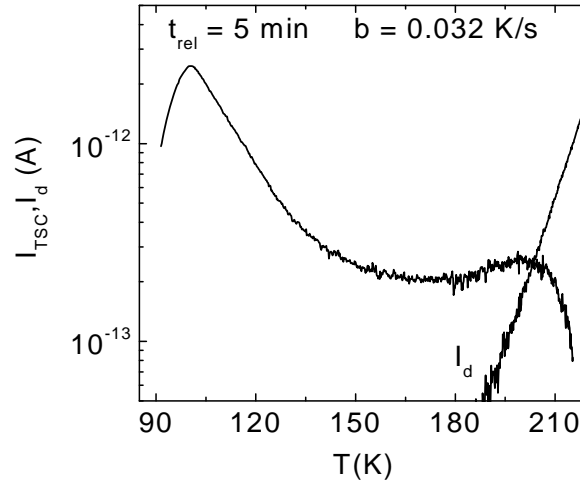


Figure 7.1: Temperature-dependent TSC and dark current. The measurements were carried out at $T_0 = 90$ K, $b = 0.032$ K/s, $t_{rel} = 5$ min and $G_0 = 2.4 \times 10^{20}$ cm⁻³ s⁻¹.

Heat treatment was carried out at a temperature of around 150 °C for 30 min. During the TSC-measurements the time-dependent current was recorded by an electrometer.

The sample was cooled down to T_0 in darkness then illuminated with a light emitting diode (LED) with wavelength $\lambda = 640$ nm. The photo-flux ϕ of the LED, measured by a photodiode, is about 10^{16} cm⁻²s⁻¹. The sample was illuminated for 3 min. After that, the excitation was turned off and the sample was allowed to relax for a time t_{rel} . Then it was heated at constant heating rate b in the darkness.

The TSC measurement in Fig. 7.1 was carried out with $T_0 = 90$ K with $b = 0.032$ K/s, and $t_{rel} = 5$ min. Figure 7.1(a) exhibits the temperature dependence of the TSC and the dark current. The TSC current increases initially with increasing temperature showing a maximum at $T_m = 100$ K. The current then decreases until 145 K. A shoulder appears over a wide range of temperature between 145 K and 203 K. Finally a sharp drop of I_{TSC} is shown from 203 K to 216 K.

7.1.1 Mobility-lifetime product determination

As has been already mentioned, separated photoconductivity measurements allow to get the temperature-dependent electron mobility-lifetime $(\mu\tau)_n(T)$ in order to extract the TSC-DOS.

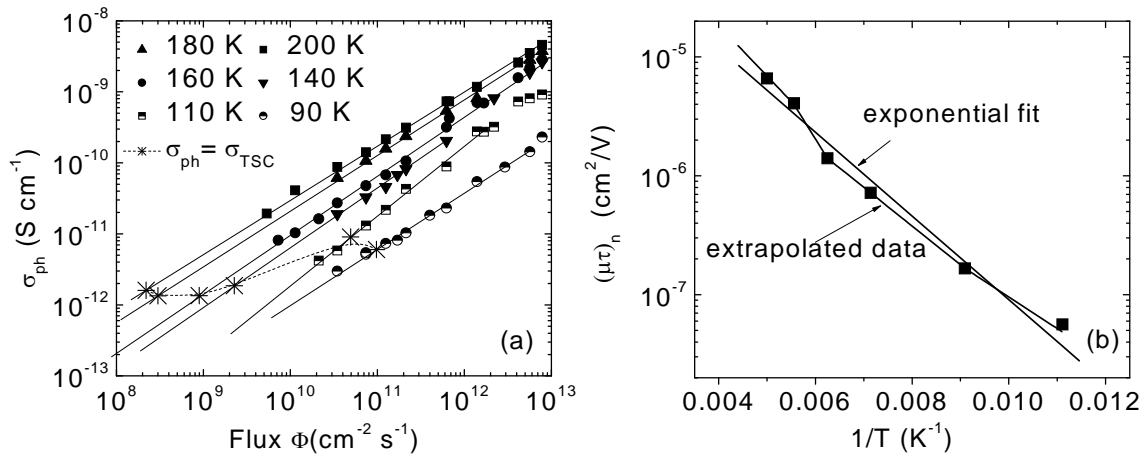


Figure 7.2: Photoconductivity measurements performed at different temperatures between 90 K and 200 K over a range of photon fluxes Φ between 10^{10} cm⁻² s⁻¹ and 10^{13} cm⁻² s⁻¹, respectively. The star symbols show σ_{ph} data such that $\sigma_{ph} = \sigma_{TSC}$, obtained by extrapolating the experimental data to low Φ . The extrapolation is represented with full line (a). Mobility lifetime product of free electrons $(\mu\tau)_n$ obtained from photoconductivity measurements. Square symbols indicate $(\mu\tau)_n$, from Eq. (5.10). Extrapolation of $(\mu\tau)_n$ data as well as exponential fit are shown (b).

For this reason, photoconductivity measurements have been performed at different temperatures.

The light source was a red He-Ne laser, with which the sample was excited at photon fluxes F between 10^{10} cm⁻² s⁻¹ and 10^{13} cm⁻² s⁻¹. Figure 7.2(a) displays σ_{ph} against the photon flux F at different temperatures.

A photon-flux F is determined for each temperature where the Eq. (5.12) is fulfilled. For $T = 140$ K, 160 K, 180 K, 200 K, an extrapolation of experimental data is needed because the values of σ_{TSC} are very small. Therefore an extrapolation of data using Eq. (5.11) is necessary. In spite of the long equilibration time considered after each measurement of σ_{ph} , an error of σ_{ph} of less than 30% is estimated.

The values of $(\mu\tau)_n(T)$ are determined according to Eq. (5.10). $(\mu\tau)_n(T)$ is plotted against $1/T$ in Fig. 7.2(b). The exponential fit and the data extrapolation are presented to obtain a shape describing $(\mu\tau)_n$. A difference smaller than 30% is calculated between experimental data and the data of exponential fit. This value is of the same order of magnitude as the error evaluated during the photoconductivity measurements. We note that, to evaluate TSC-DOS, the simple exponential fit is chosen.

7.1.2 Simulation of experimental results

To determine the TSC-DOS, the evaluation of the effective attempt-to-escape frequency ν_{eff} is necessary. In the previous simulation (see chapter 6), it has been shown that ν_{eff} could be calculated for the cases of weak and strong retrapping regimes by using: $\sigma_{TSC} \ll \sigma_d$ and $\sigma_{TSC} = \sigma_d$, respectively. Thus we suggest to examine both conditions separately. In each case, TSC simulation is performed in order to reproduce the experimental σ_{TSC} . The procedure consists of the following steps:

1. From $\sigma_{TSC} = \sigma_d$, the values of $T_{F,exp}$, $\nu_{eff,exp}$ and $E_c - E_F$ are evaluated. $E_c - E_F = kT_{F,exp} \ln(200 \text{Scm}^{-1} / \sigma_d)$ and $\nu_{eff,exp}$ (according to Eq. (5.15)) are determined.
2. Evaluation of the input DOS. From the $\nu_{eff,exp}$ value, the TSC-DOS (according to Eq. (5.15) and (5.19)) is evaluated. This DOS is approximated to be the input DOS in the simulation.
3. Simulation parameters. The simulation is performed using the experimental parameters as input parameters in the simulation. These parameters are: heating rate $b = 0.032$ K/s, $t_{rel} = 5$ min, $G_0 = 1 \times 10^{20} \text{cm}^{-3} \text{s}^{-1}$, $T_0 = 90$ K, and carrier lifetime $\tau(T)$ obtained from the mobility lifetime product (see exponential fit in Fig. 7.2(b)). The mobility μ is assumed temperature independent and it is equal $10 \text{cm}^2/\text{V}$.
4. Simulation circles. In the TSC simulation, the attempt-to-escape frequency ν_0 must be given. Knowing that ν_{eff} must always be smaller than ν_0 , we suggest to vary ν_0 such as $\nu_{eff} \leq \nu_0$ in order to get the best fit between $\sigma_{TSC,exp}$ (experimental data) and $\sigma_{TSC,sim}$ (simulated data).
5. Reconstruction of the DOS. From the condition $E_{m,s} = E_F$, $T_{F,sim}$ is graphically obtained and then $\nu_{eff,sim}$ is evaluated. $\sigma_{TSC,sim}$ and the value of $\nu_{eff,sim}$ are introduced in Eq. 5.19 in order to evaluate the reconstructed DOS.
6. Whenever no good fit between simulated and experimental σ_{TSC} could be obtained, we used the second option by assuming a weak retrapping regime. The same steps from 1 to 4 must be considered in order to reproduce once again the experimental σ_{TSC} .

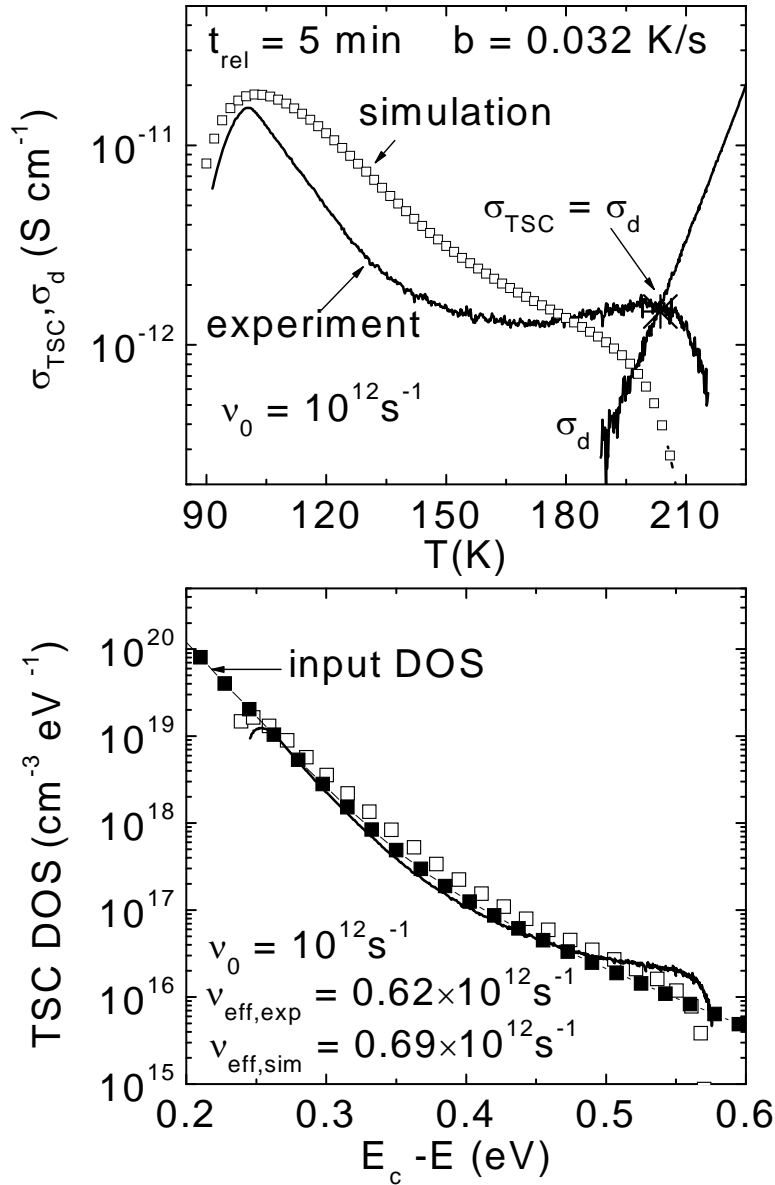


Figure 7.3: Simulated and experimental σ_{TSC} . σ_d is added. The star symbol shows the temperature $T_{F,exp}$ where $\sigma_{TSC} = \sigma_d$ is fulfilled. The simulation is performed with $b = 0.032$ K/s, $t_{rel} = 5$ min. The square symbols represent simulated σ_{TSC} indicating a strong discrepancy with experimental σ_{TSC} (a). Open symbols indicate the reconstructed DOS from simulated σ_{TSC} , while the full line indicates TSC-DOS from experimental σ_{TSC} . Full symbols are input DOS (b).

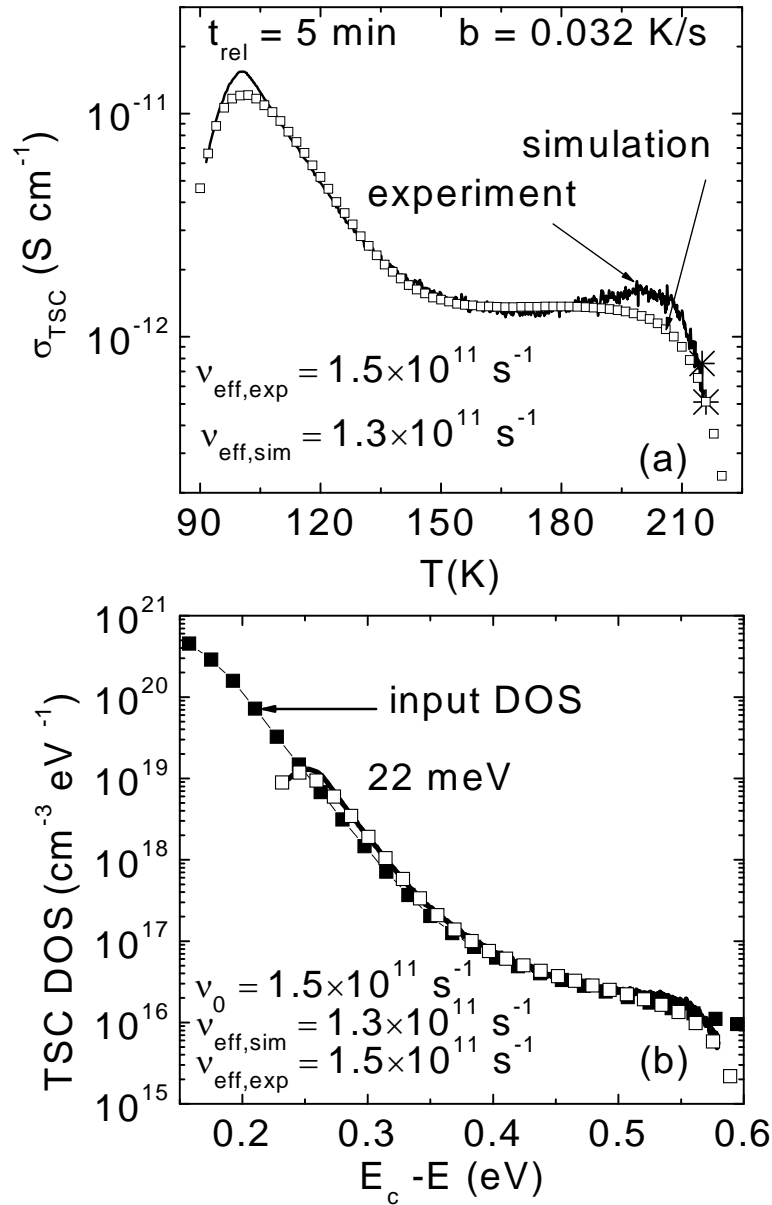


Figure 7.4: Simulated (square symbols) and experimental (full line) σ_{TSC} . The star symbols shows the temperature $T_{F,exp} = 215$ K and $T_{F,sim} = 216$ K at which $v_{eff,exp} = 1.5 \times 10^{11} \text{ s}^{-1}$ and $v_{eff,sim} = 1.3 \times 10^{11} \text{ s}^{-1}$ are evaluated (a). Full line indicates TSC-DOS obtained from experimental σ_{TSC} . Open symbols indicate reconstructed DOS evaluated from simulated σ_{TSC} and $v_{eff,sim}$ value. The simulation is performed with input DOS shown with full symbols. In the simulation v_0 is taken equal $1.5 \times 10^{11} \text{ s}^{-1}$ (b).

We start with the condition $\sigma_{TSC} = \sigma_d$, at which graphically $T_{F,exp} = 203.6$ K is obtained. $E_c - E_F = 0.570$ eV and $\nu_{eff,exp} = 6.2 \times 10^{11} \text{ s}^{-1}$ are calculated. ($T_{F,exp}$ is represented by the star symbol in Fig. 7.3(a). Different simulations are performed for ν_0 between $6.2 \times 10^{11} \text{ s}^{-1}$ and $1 \times 10^{12} \text{ s}^{-1}$. As a result, the experimental σ_{TSC} is not correctly reproduced. An example is shown in Fig. 7.3 where $\nu_0 = 1 \times 10^{12} \text{ s}^{-1}$. In Fig. 7.3(b), an acceptable agreement is shown between the input and the reconstructed DOS in contrast, simulated and experimental σ_{TSC} differ (Fig. 7.3(a)).

We now start with the assumption that weak retrapping applies. We use $\sigma_{TSC} \ll \sigma_d$ and then we determine $T_{F,exp}$. But it is not possible to identify $T_{F,exp}$ unambiguously as in the case of strong retrapping. We can observe from Fig. 7.1 that the $\sigma_{TSC} \ll \sigma_d$ region lies above 203.6 K and correspond to a range of temperature, we then suggest to select several different temperatures $T_{F,exp}$ in this region and hence evaluate possible $E_c - E_F$ and $\nu_{eff,exp}$ values.

To illustrate this approach the first ‘‘trial’’ temperature selected is $T_{F,exp} = 211$ K (at which $\sigma_{TSC} / \sigma_d \approx 0.33$), giving $E_c - E_F = 0.575$ eV and $\nu_{eff,exp} = 2.5 \times 10^{11} \text{ s}^{-1}$. Using these figures, a DOS was computed (step 2) and then to ‘‘close the loop’’ we simulated σ_{TSC} from this DOS, but found an insufficient agreement between the original experimental and the simulated σ_{TSC} . Moving further down the ‘‘ σ_{TSC} drop’’ such that $\sigma_{TSC} = 0.1 \sigma_d$ results in, $T_{F,exp} = 215$ K, $E_c - E_F = 0.577$ eV and $\nu_{eff,exp} = 1.5 \times 10^{11} \text{ s}^{-1}$. Using these figures to calculate the TSC-DOS allows us to represent the simulation input DOS by a linear function between 0 and 0.1 eV and the sum of two exponential functions where the first band tail parameter $E_0 = 22$ meV is between E_c and $E_c - E = 0.3$ eV and the second $E_0 = 114$ meV is between $E_c - E = 0.3$ eV and $E_c - E = 0.7$ eV.

By taking $\nu_0 = \nu_{eff,exp} = 1.5 \times 10^{11} \text{ s}^{-1}$, a very good agreement between experimental and simulated TSC conductivity is obtained, as shown in Fig. 7.4(a). By applying $E_{m,s} = E_F$, $T_{F,sim} = 216$ K is graphically determined and hence $\nu_{eff,sim} = 1.3 \times 10^{11} \text{ s}^{-1}$ is evaluated (according to Eq. (5.15)).

In a further step, the DOS is perfectly reconstructed from the simulated σ_{TSC} using $\nu_{eff,sim}$ value (Fig. 7.4(b)). This demonstrates the consistency of the combined experiment-simulation approach.

We note that simulations where $\nu_0 > \nu_{eff,exp}$ ($\nu_{eff,exp} = 1.5 \times 10^{11} \text{ s}^{-1}$) show a poor agreement between simulated and experimental σ_{TSC} .

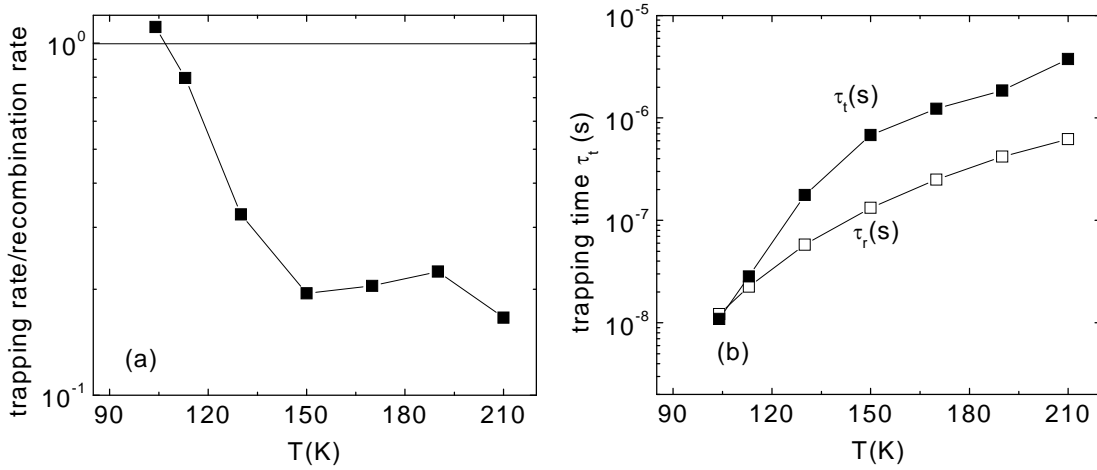


Figure 7.5: The temperature dependence of the ratio retrapping rate to recombination rate (a). Retrapping time $\tau_t(T)$ is represented with full symbol, while the recombination time $\tau_r(T)$ is represented with open symbol (b).

To compare the strong and weak retrapping effect, we calculate and then plotted the ratio r , retrapping rate to recombination rate against the temperature. $\tau_r(T)$ is calculated from Eq (6.9). Figure 7.5(a) shows the ratio r against the temperature. Over the whole range of the temperature, r varies between 0.166 and 1.11. A plateau appears between 150 K and 210 K. Figure 7.5(b) displays both retrapping $\tau_t(T)$ and recombination $\tau_r(T)$ times. At low temperature i.e. below 120 K, $\tau_t(T)$ is slightly larger than $\tau_r(T)$. However at a high temperature, an appreciable difference between $\tau_t(T)$ and $\tau_r(T)$ can be observed.

Figure 7.6(a) illustrates $E_c - E_{m,s}$, $E_c - E_{m,a}$, $E_c - E_q$ and $E_c - E_F$ against the temperature from the simulation (see Fig.7.4). It can be seen that $E_c - E_{m,s}$ represented with full symbol agrees very well with $E_c - E_{m,a}$ data obtained from Eq. (5.15). In contrast, a discrepancy is shown essentially at high temperature between $E_c - E_{m,s}$ and $E_c - E_q$. At low temperature and below 120 K, $E_c - E_q$ is close to $E_c - E_{m,s}$. We note that $E_c - E_{m,s}$ crosses $E_c - E_F$ at 216 K where $\nu_{eff,sim} = 1.3 \times 10^{11} \text{ s}^{-1}$ is evaluated.

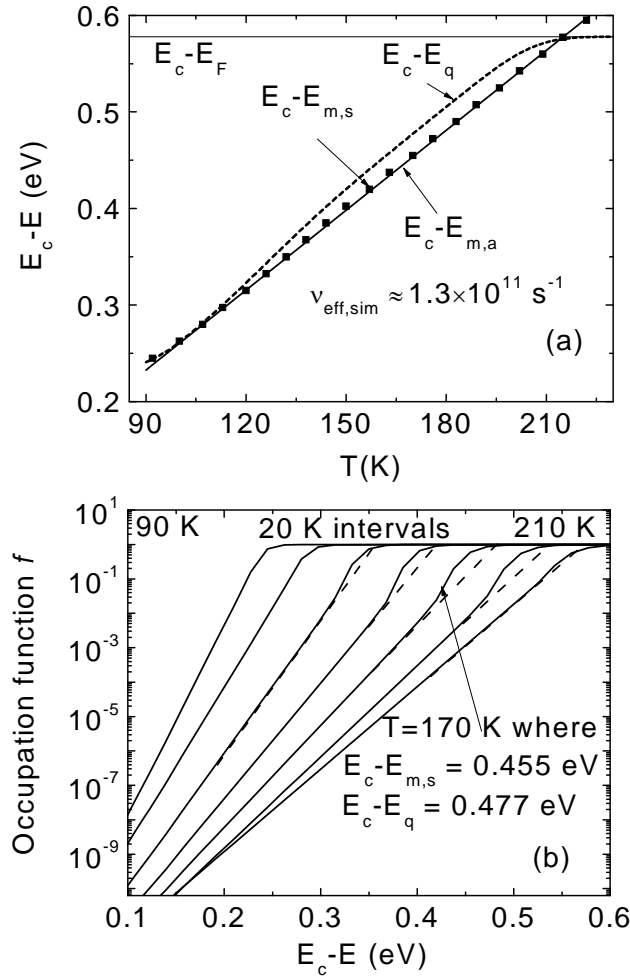


Figure 7.6: Temperature-dependent computed $E_c - E_{m,s}$ (square symbol) and analytical $E_c - E_{m,a}$ (full line) peak emission energy, quasi-Fermi level $E_c - E_q$ (dashed line) and E_F . Good overlap is shown between $E_c - E_{m,a}$ and $E_c - E_{m,s}$ (a). Occupation function f determined for different temperature between 90 K and 230 K at 20 K intervals. The jump of f at $E_c - E_{m,s}$ underlines the weak retrapping regime. An example of f is shown at $T = 170 \text{ K}$, where $E_c - E_{m,s} = 0.455 \text{ eV}$ and $E_c - E_q = 0.477 \text{ eV}$ (b).

Figure 7.6(b) shows the occupation function f against the energy. f is evaluated at different temperatures between 90 K and 210 K with 20 K interval. At the temperature 170 K, $E_c - E_{m,s} = 0.455 \text{ eV}$ and $E_c - E_q = 0.477 \text{ eV}$. In addition for a given temperature, Fig. 7.6(b) reveals that f is not Boltzmann function. As we have already explained in the last chapter, this is due to the presence of a strong jump of f . The dashed lines show the extrapolation of f if f was a Boltzmann function. The extrapolation at $f = 1$ indicates E_q value.

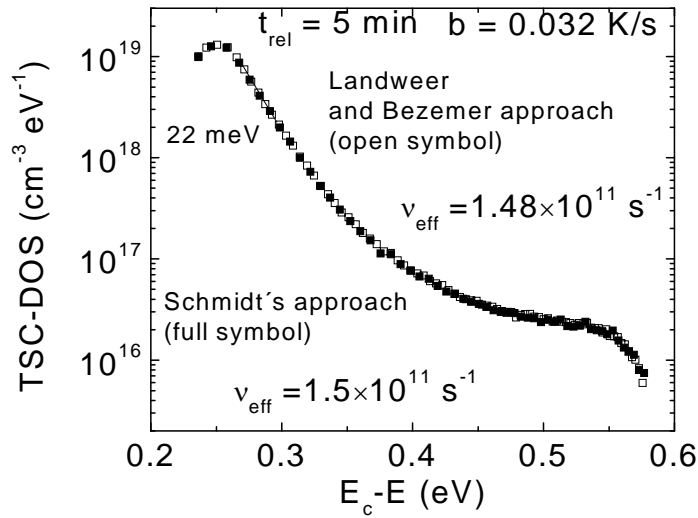


Figure 7.7: TSC-DOS from the Landweer and Bezemer approach according to Eqs. (5.13) and (5.14) is represented with open symbols. The corresponding ν_{eff} is around $1.48 \times 10^{11} \text{ s}^{-1}$. The TSC-DOS from the Schmidt's approach according to Eqs. (5.15) and (5.19) is represented with full symbols, $\nu_{eff} = 1.48 \times 10^{11} \text{ s}^{-1}$. An excellent overlap is shown between both procedures.

7.1.3 Application of Landweer and Bezemer approach

Until now the extraction of DOS was achieved by applying the Schmidt's approach whose validity has been clearly shown in chapter 6. For comparison we apply in this section the Landweer and Bezemer procedure.

Figure 7.7 indicates the experimental data of the TSC-DOS by applying the Landweer and Bezemer approach represented with open symbol and the Schmidt's approach with full symbol. A slight difference of about 1.3% is detected in ν_{eff} determination. However, a very good agreement is shown in the TSC-DOS between both approaches.

7.2 Discussion

The TSC curve in Fig. 7.1 shows an initial rise followed by a sharp drop of σ_{TSC} from $T_m = 100.2 \text{ K}$. Therefore, the presence of a conduction band tail is expected. With increasing

temperature T , σ_{TSC} slowly decreases over a wide range of T and then drops to very small values of σ_{TSC} because all gap states are in equilibrium with the transport states.

From photoconductivity measurements exponential profile is found to describe $(\mu\tau)_n$ values. TSC-DOS determination requires to have not only $(\mu\tau)_n$ but also ν_{eff} in order to establish the energy scale. ν_{eff} is calculated by applying $\sigma_{TSC} = \sigma_d$. Different simulations have been done by varying ν_0 in order to get the best fit of experimental σ_{TSC} . A very good overlap between simulated and experimental σ_{TSC} is obtained when $\nu_0 \approx \nu_{eff,exp} \approx 1.5 \times 10^{11} \text{ s}^{-1}$; simulated $\nu_{eff,sim}$ is the same order as the experimental $\nu_{eff,exp}$. The reconstructed TSC-DOS from simulated σ_{TSC} agrees very well with the experimental and input DOS (Fig. 7.4).

In order to gain more information about the retrapping regime other features have been investigated. In Fig. 7.5(a), the ratio r , retrapping to recombination rate, is lower than the value 1 at high temperature showing a stronger recombination than retrapping. However, if we examine r at low temperature below 120 K in Fig. 7.5(b), $\tau_i(T)$ is slightly above $\tau_r(T)$, which indicates that in this region an intermediate regime can be expected. This agrees well with the overlap shown in Fig. 7.6(a) between $E_c - E_q$ and $E_c - E_{m,s}$ below 120 K. But in the whole range of temperatures above 120 K, $\tau_i(T)$ is widely larger than $\tau_r(T)$, and $E_c - E_{m,s}$ and $E_c - E_{m,a}$ agree very well. All these indications show that the recombination effect is larger than retrapping effect. Also in Fig. 7.6(b), the occupation function f , for temperatures below T_F , illustrates that f , close to $E_c - E_m$, is not Boltzmann function. This again emphasises the weak retrapping regime of this sample.

In summary, we found: ν_0 and ν_{eff} are the same order of magnitude, $E_c - E_{m,s}$ and $E_c - E_{m,a}$ agree well, $\tau_i(T) > \tau_r(T)$ and f is not a Boltzmann function in the region close to $E_c - E_m$. Consequently, σ_{TSC} corresponds to weak retrapping regime

To compare quantifiably the TSC-DOS with other approaches, the Bezemer approach has been applied. The excellent agreement between the TSC-DOS in Fig. 7.7 and the similar values of ν_{eff} demonstrate that the differences in the numerical values in Eq. (5.13) and (5.14) and also Eq. (5.15) and (5.19) are not important. The advantage of the Schmidt approach is the high flexibility to account for a variation in T_0 .

Over a range of energy between 0.25 eV and 0.32 eV the TSC-DOS in Fig. 7.7, (from Bezemer or Schmidt procedure), reveals in both cases, a band-tail parameter of about 22 meV. Deeper in the gap the DOS changes and a shoulder appears. The drop in the TSC-DOS between 0.55 eV and 0.6 eV indicates the position of the Fermi level. It important to point out

that an error about 30 % is estimated for TSC-DOS determination. This is due to the error in the photocurrent measurement (we recall that, this measured photocurrent allows to get $(\mu\tau)_n$). Besides, the capture coefficient defined as $c_n = v_0/N_c$ is estimated around $1.5 \times 10^{-9} \text{ cm}^3 \text{ s}^{-1}$.

7.3 Parameter variation

Different parameters during the TSC measurements are varied such as heating rate b , initial temperature T_0 , relaxation time t_{rel} , and generation rate G_0 . The aim of these measurements is to gain more information about the experimental initial rise of σ_{TSC} at low temperature and also to investigate the effect of the experimental parameters on the TSC-DOS as well as on the retrapping regime. In each section the results are presented followed by a discussion.

7.3.1 Heating rate variation

Fig. 7.8(a) shows the temperature against the time for different heating rates b between 0.034 K/s and 0.087 K/s. A constant heating rate is chosen to describe $T(t)$.

Fig. 7.8(b) displays different measurement cycles of excess currents for $T_0 = 90 \text{ K}$ with $t_{rel} = 30 \text{ min}$ and $G_0 = 2.4 \times 10^{20} \text{ cm}^{-3} \text{ s}^{-1}$. The constant heating rate b is varied between 0.034 K/s and 0.087 K/s. At low temperature, the data approximately exhibit the same initial rise until 98 K. With increasing b , the current increases showing different maxima T_m in the TSC currents such as: 104.8 K (0.034 K/s), 108.1 K (0.054 K/s), 109 K (0.072 K/s) and 109.5 K (0.087 K/s). By approaching the dark current at high temperature, the curves become much closer.

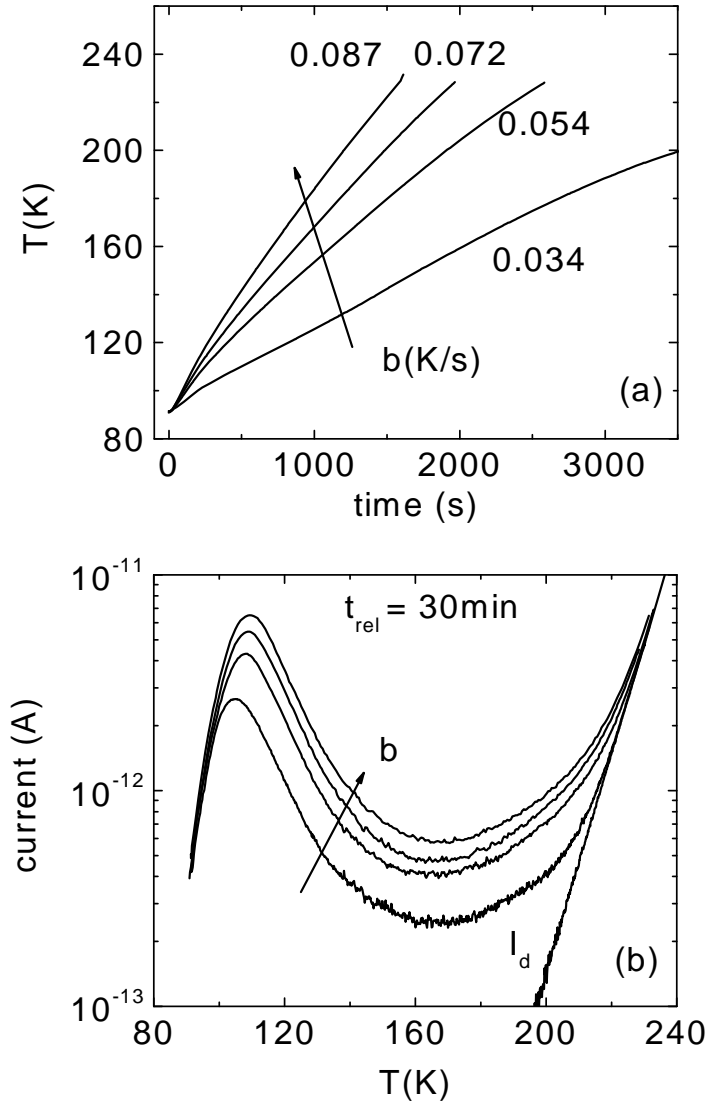


Figure 7.8: Time-dependent temperature for different experimental heating rates b between 0.034 K/s and 0.087 K/s (a). Temperature-dependent excess and dark current by varying heating rate b between 0.034 K/s and 0.087 K/s. The measurements are performed with $T_0 = 90$ K, $t_{rel} = 30$ min and $G_0 = 2 \times 10^{20} \text{ cm}^{-3} \text{ s}^{-1}$ (b).

Initial rise at low temperature

In order to understand the origin of the experimental initial rise of σ_{TSC} at low temperature, we propose to apply Eq. (6.10) and Eq. (6.11). The experimental initial rise in Fig 7.9 obtained with $b = 0.034$ K/s and $t_{rel} = 30$ min (see Fig. 7.8(b)) is represented with full line. The full symbols indicate the calculated initial rise from Eq. (6.10) and Eq. (6.11). Very good overlap is shown in Fig. 7.9 between experimental and calculated σ_{TSC} .

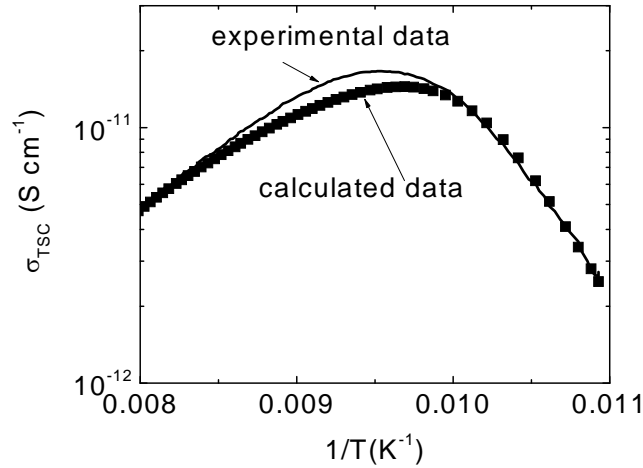


Figure 7.9: Experimental and calculated initial rise of σ_{TSC} against $1/T$ for $b = 0.034$ K/s. Full line represented experimental data from Fig. 7.8(b): Open symbols represent the calculated data according to Eq. (6.10) and Eq. (6.11). The input parameters in the analytical calculations are: $T_0 = 90$ K, the quasi Fermi level E_q after t_{rel} and just before heating equals 0.2518 eV and $T_{oc} = 267$ K.

This is achieved only when the DOS, described with an exponential function which is proportional to $\exp(-(E_c - E_m)/E_o)$ ($E_o = kT_{oc}$), and the mobility lifetime product depending on the temperature are considered. In the calculation, we take $v_{eff} = 1.5 \times 10^{11} \text{ s}^{-1}$, $T_{oc} = 267$ K, $T_0 = 90$ K and the quasi Fermi level $E_c - E_q$ after t_{rel} and just before heating equals 0.2518 eV. As is explained in sketch represented in Fig. 6.17, the peak of σ_{TSC} at low temperature is caused by the product of a fast decrease of $(\mu\tau)_ng(E_m)$ and exponential increase of the occupation function at T_0 . Fritzsche showed a bad fit between calculated and experimental initial rise at $T_0 = 130$ K [31,86,88]. This is may be because the conduction band tail and the mobility lifetime product are not taken into account.

Figure 7.10 reveals I_{TSC} against the time for different heating rates between 0.034 K/s and 0.087 K/s. The integrated charge Q such that $Q = \int I_{TSC} dt$ is calculated for each TSC curve. A slight increase of about 15% of Q is observed with increasing b .

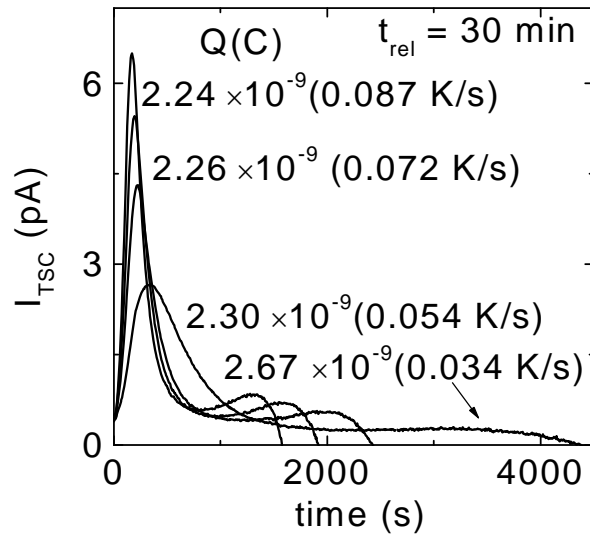


Figure 7.10: Time-dependent TSC current for different b between 0.034 K/s and 0.087 K/s. The integrated charge Q is deduced for each I_{TSC} .

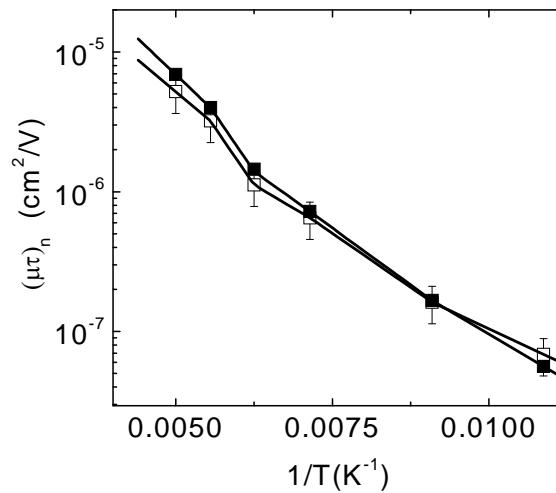


Figure 7.11: Mobility lifetime product $(\mu\tau)_n$ obtained from photoconductivity measurements. Open symbols are evaluated from σ_{TSC} whose $b = 0.072$ K/s. The plot of $(\mu\tau)_n$ (full symbol) related to $b = 0.034$ K/s is added for comparison.

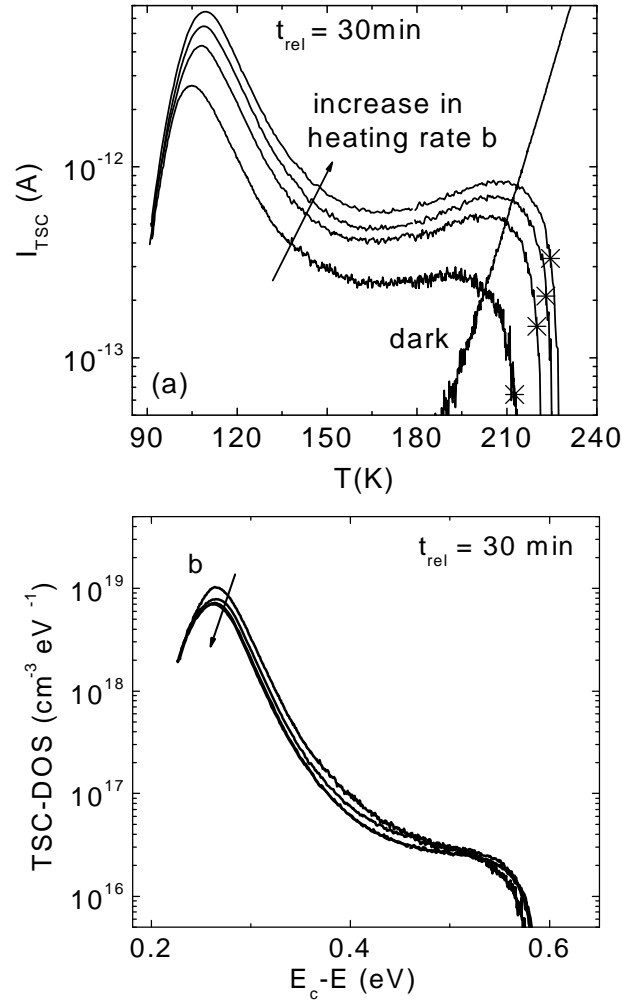


Figure 7.12: Temperature-dependent I_{TSC} and dark current by varying b between 0.034 K/s and 0.087 K/s. With star symbol we show T_F at which v_{eff} is evaluated (a). Corresponding TSC-DOS (b).

To get the TSC-DOS corresponding to each TSC curve, the evaluation of the $(\mu\tau)_n$, related to each TSC, is necessary. For this sample, the γ value (see Eq. (5. 12)), obtained from the fit of the curves in Fig. 7.2(a), varies between 0.75 and 0.93. Therefore, according to $(\mu\tau)_n \approx G^{\gamma-1}$, we can expect that the calculated values of $(\mu\tau)_n$ at given temperature, are similar. For each TSC curve in Fig. 7.8(b), $(\mu\tau)_n$ is evaluated. An example is shown in Fig. 7.11 where $(\mu\tau)_n$ is obtained from photoconductivity measurements. For comparison, the plot of $(\mu\tau)_n$ in Fig. 7.2(b) is added; a difference less than 30% is detected. This difference and the error estimated during photoconductivity measurements (Fig. 7.2(a)) are of the same order of

magnitude. This implies that $(\mu\tau)_n$ curves, corresponding to different σ_{TSC} plotted in Fig.7.8(b), could be considered similar.

Fig. 7.12(a) shows the TSC current corresponding to Fig. 7.8(b) after subtraction of I_d . The different TSC drops shift to higher temperature with increasing b . The v_{eff} value is evaluated for each TSC curve using $E_{m,a} = E_F$ where $\sigma_{TSC} = 0.1\sigma_d$: we obtain $1.7 \times 10^{11} \text{ s}^{-1}$ (0.034 K/s), $1.32 \times 10^{11} \text{ s}^{-1}$ (0.054 K/s), $1.14 \times 10^{11} \text{ s}^{-1}$ (0.072 K/s) and $1.12 \times 10^{11} \text{ s}^{-1}$ (0.087 K/s). Star symbol indicates the related T_F . Fig. 7.12(b) represents the corresponding TSC-DOS. Only a slight variation in TSC-DOS is observed when b changes in spite of the current increase. This variation is smaller than 30%. The conduction band tail parameter is about 22 meV with a variation of about 2 meV.

Discussion

The general shape of TSC does not change for different b . However, the low temperature-peak moves to higher temperature and increases in height (Fig. 7.8(b)). From analytical calculations, Simmons [83] determined the TSC current for different b and the same trends have been observed. In addition, experimental measurements from other authors [100,101] also show the same behaviour. The increase of the current is certainly due to stronger emission of carriers to conduction band, caused by the b increase.

In order to show the presence of the low temperature-peak, the experimental data in Fig. 7.9 are fitted using Eq. (6.10) and Eq. (6.11). By taking into account the presence of the conduction band tail as well as the variation of $(\mu\tau)_n$ against the temperature, a good fit between experimental and calculated σ_{TSC} is shown in Fig. 7.9. Therefore the low-temperature peak of TSC is due to the product of the Boltzmann tail of the occupation function $f_0(E_m)$ at starting temperature T_0 and the term $(\mu\tau)_n g(E_m)$. We conclude that the theory of Bezemer expects the presence of low-temperature peak when the rise of the occupation function at T_0 is considered.

In addition, we note that the integrated charge does almost not vary with increasing b .

To establish the energy scale, v_{eff} is evaluated at different temperature T_F . The slight variation in the different TSC-DOS in Fig. 7.12(b) indicates that the procedure for the DOS determination from TSC is robust in view of the observed variation in the current upon a

change in b . A variation of 30% is detected which is the same order of magnitude of the error estimated in determining the TSC-DOS. Consequently, the TSC-DOS could be considered b -independent.

7.3.2 Initial temperature variation

In these measurements the sample is illuminated at different initial temperatures, while all other parameters are kept the same. Consequently, a series of initial rise is obtained.

TSC measurements in Fig. 7.13(a) are carried out with a constant heating rate 0.055 K/s, $t_{rel} = 30$ min and different initial temperatures $T_0 = 90, 100$ and 140 K.

The figure reveals clearly 2 different sharp peaks at 90 K and 100 K. Although the initial rise of TSC is different for various T_0 , the TSC thereafter follow the same curve at higher temperature. Fig. 7.13(b) shows the TSC-DOS corresponding to the measurements in Fig. 7.13(a) by applying Eq. (5.19). Different energy ranges are taken into account using Eq. (5.15).

Fig. 7.14 shows the calculated and experimental initial rise at different T_0 . For calculations (Eq. (6.10)) the input parameters are: $T_{0c} = 267$ K and $E_c - E_q = 0.2524$ eV for $T_0 = 90$ K, $T_{0c} = 290$ K and $E_c - E_q = 0.2734$ eV for $T_0 = 100$ K, and $T_{0c} = 302$ K and $E_c - E_q = 0.3938$ eV for $T_0 = 140$ K. A good overlap is shown between calculated and experimental initial rise when T_0 increases.

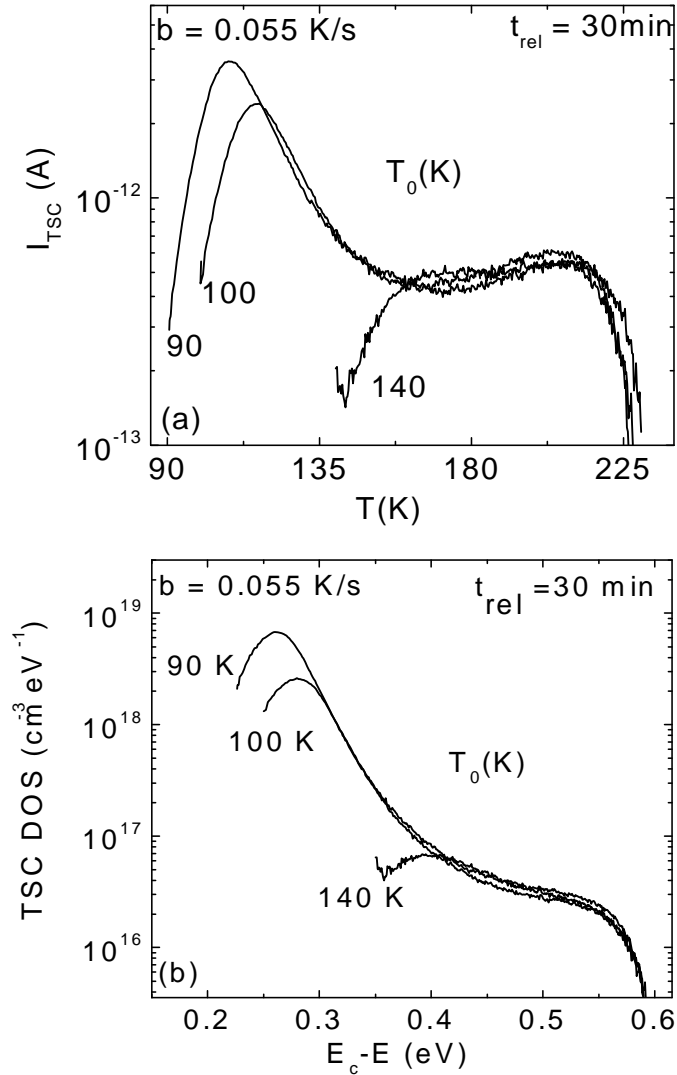


Figure 7.13: Temperature-dependent I_{TSC} and dark conductivity for $T_0 = 90$ K, 100 K and 140 K. The measurements are carried out with $b = 0.055$ K/s and $t_{rel} = 30$ min (a). Corresponding TSC-DOS (b).

Discussion

In Fig. 7.13(a), the low-temperature peak moves to higher temperature T_0 and the magnitude rapidly decreases. A strong dependence is observed between T_m and T_0 . These results agree well with those from Fritzsche-Ibaraki [31,32]. To show the origin of the peak at high temperature, the initial rise is calculated for each T_0 by applying Eq. (6.10) and Eq.

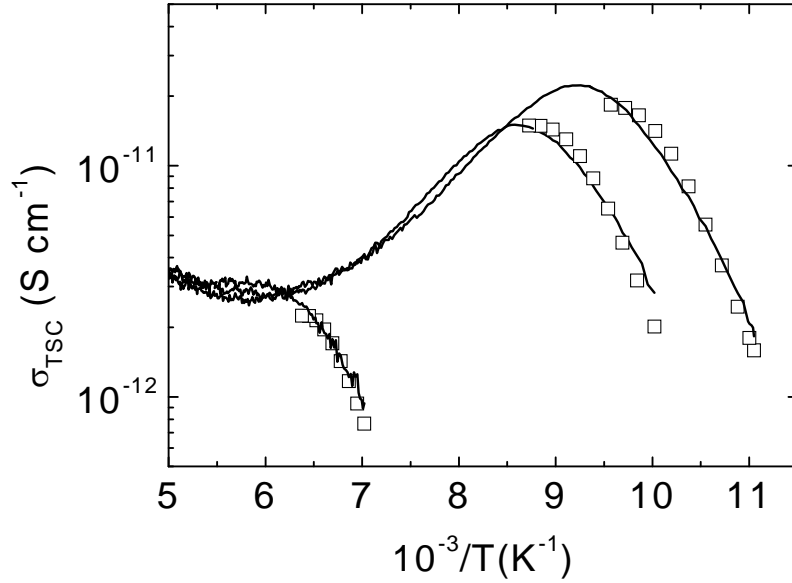


Figure 7.14: A series of different onsets in TSC presented as function of the inverse of T (full line). The data are taken from Fig. 7.13(a). Square symbols indicate the calculated initial rise from Eq. (6.11) and Eq. (6.12). The input parameters in the calculations are: $T_{0c} = 267$ K and $E_c - E_q = 0.2524$ eV for $T_0 = 90$ K, $T_{0c} = 290$ K and $E_c - E_q = 0.2734$ eV for $T_0 = 100$ K and $T_{0c} = 302$ K and $E_c - E_q = 0.3938$ eV for $T_0 = 140$ K

(6.11). A good agreement is displayed in Fig. 7.14 indicating once again that the presence of the initial rise is caused by the product of $((\mu\tau)_{ng}(E))$, showing a rapid decrease, and the occupation function at starting heating rate, showing a rapid increase.

It is important to point out that Zhou and Elliott [91] and other authors [100] showed that below a critical temperature T_0 ($T_{0r} = 80$ K), the low-temperature peak does not depend on T_0 , and the various initial rise have the same T_m . In this case T_0 is larger than T_{0r} and the initial rise can be accounted for by the emission from partially filled DOS when E_m is moving between the conduction band edge and the quasi Fermi level at T_0 .

The different onsets in the TSC-DOS distributions in Fig. 7.13(b) demonstrate that the low-energy maximum is not a real image of the DOS. In addition, a good overlap in the TSC-DOS is observed when T_0 is varied.

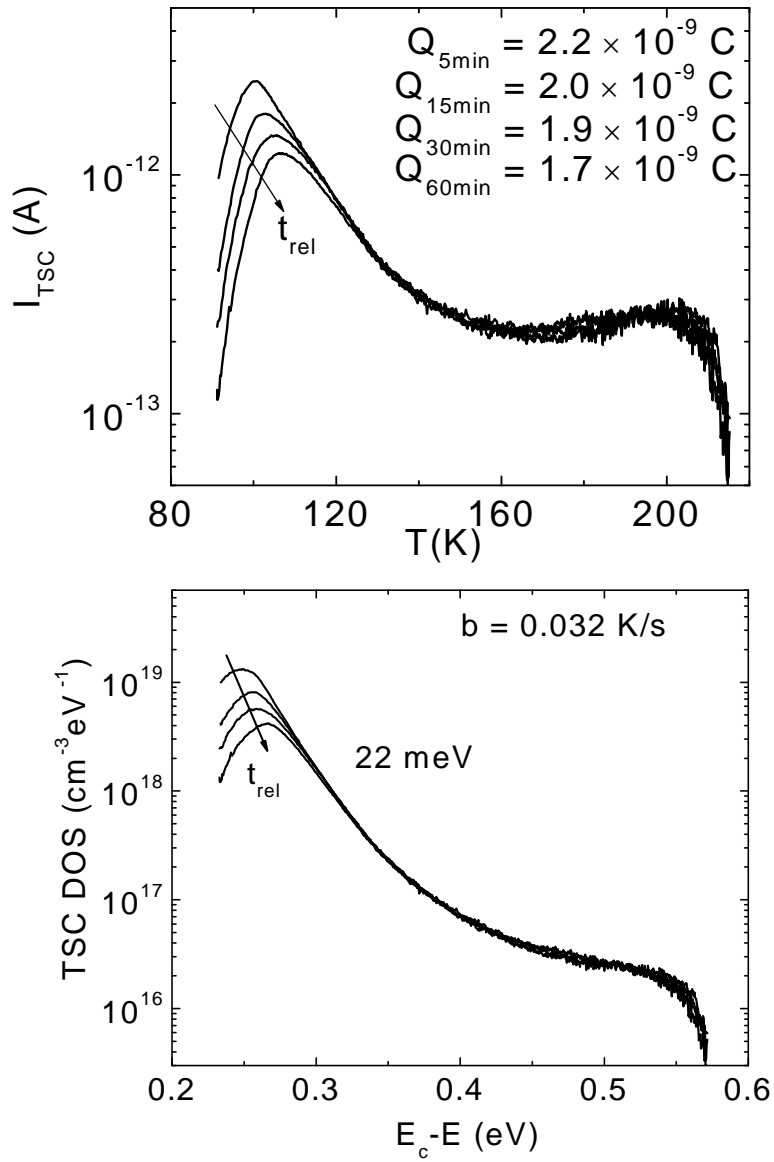


Figure 7.15: Temperature-dependent I_{TSC} by varying t_{rel} between 5 min and 1h. The measurements are carried out with $b = 0.032$ K/s and $T_0 = 90$ K and $G_0 = 2 \times 10^{20} \text{ cm}^{-3} \text{ s}^{-1}$ (a). Corresponding TSC-DOS (b).

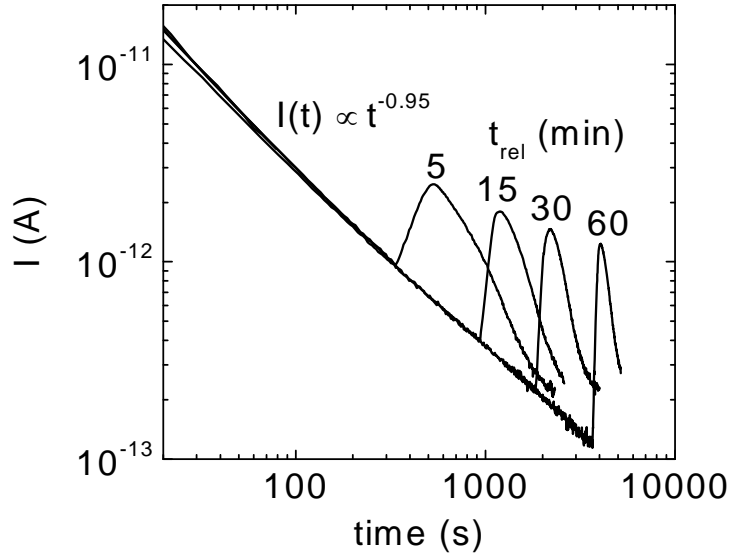


Figure 7.16: Time-dependence of I showing the decay of photocurrent after illumination at 90 K. The decay is obtained for different t_{rel} between 5 min and 60 min. A power-law exponent according to t^{-a} with $a = 0.95$ is also shown.

7.3.3 Relaxation time variation

In this section we investigate the effect of the relaxation time t_{rel} on the TSC as well as the TSC-DOS shape. For this reason, TSC measurements are performed by varying t_{rel} between 5 min and 1h at $T_0 = 90$ K, $b = 0.032$ K/s and $G_0 = 2 \times 10^{20} \text{ cm}^{-3} \text{ s}^{-1}$.

Fig. 7.15 (a) reveals different initial rise starting at different current. The peak moves at high temperature and becomes higher with decreasing t_{rel} . With increasing t_{rel} , the current at 90 K decreases leading to a slight increase of quasi Fermi level E_q . Above the peak at high temperature, the TSC curves are similar. In this region, the TSC is not affected by the initial distribution change at 90 K. Besides, the integrated charge Q decreases for longer t_{rel} . Over the energy range from 0.25 eV to E_F , Fig. 8.15 (b) displays a very good overlap between TSC-DOS obtained from Fig. 7.15 (a).

A logarithmic scale is chosen in Fig. 7.16 to examine the current decay during t_{rel} at 90 K before heating. The current decay is described with power-law exponent according to t^{-a} where $a = 0.95$. Also, the figure displays different peaks for different t_{rel} . The maximum of the TSC peak is higher for smaller value of t_{rel} .

Discussion

The effect of the eventual change on the characteristic of TSC by changing the relaxation time t_{rel} between 5 min and 60 min is shown in Fig. 7.15(a). For a longer waiting time the current decreases and the quasi Fermi level E_q , just after t_{rel} , shifts towards E_F ($E_c - E_{q,5min} = 0.2458$ eV, $E_c - E_{q,15min} = 0.2525$ eV, $E_c - E_{q,30min} = 0.2560$ eV and $E_c - E_{q,60min} = 0.2611$ eV), which indicates that the density of the trapped carriers also decreases. Consequently the integrated charge Q equally must decrease. This has been already checked; a variation of Q of about 23% is detected when t_{rel} changes from 5 min to 60 min. However, the general shape for $T > T_m$ (the maximum temperature of the peak) is t_{rel} -independent. The corresponding TSC-DOS in Fig. 7.15(b) exhibit a very good agreement showing that the calculated DOS, between 0.25 eV and Fermi level, does not depend on t_{rel} .

We showed in Fig. 7.16 that the decay is described by a power-law, with power-law exponent of 0.95. This agrees well with the analytical study of the decay which is done by Fritzsche in the case of weak retrapping regime and where the decay of the current is proportional to t^{-1} [91].

7.3.4 Photogeneration rate variation

Fig. 7.17(a) displays two different TSC carried out with two different photogeneration rates G_0 , 3.5×10^{16} cm⁻³s⁻¹, and 2.4×10^{20} cm⁻³s⁻¹, and $T_0 = 90$ K. The other experimental parameters are kept the same: $b = 0.052$ K/s and $t_{rel} = 30$ min. We note that the sample was first illuminated with the smallest G_0 and then after the TSC measurement; it was cooled and again illuminated at 90 K with the second G_0 .

Fig. 7.17(a) does not reveal a significant difference in the current when G_0 changes by 4 orders of magnitude. The corresponding TSC-DOS curves also are very similar.

Figure 7.18(a) shows the current I depending on the time measured at 90 K. The figure reveals the first two steps prior to the measurement. The two photo-generation rates 3.5×10^{16} cm⁻³s⁻¹ and 2.4×10^{20} cm⁻³s⁻¹ are considered. For the first step, the current for $G_0 = 3.5 \times 10^{16}$ cm⁻³s⁻¹ is of 3 orders of magnitude smaller with respect to the current measured when $G_0 = 2.4 \times 10^{20}$ cm⁻³s⁻¹; but still this does not affect the decay of current in Fig. 7.18.(a) after illumination. Besides, the integrated charge Q shown in Fig. 7.18(b) does not vary with increasing G_0 .

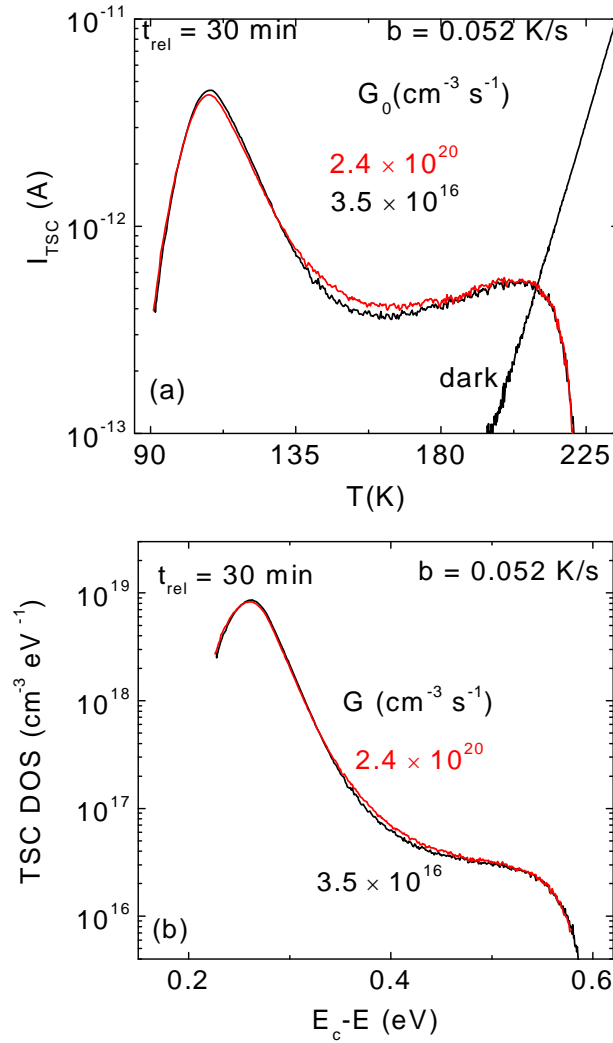


Figure 7.7: Temperature-dependent I_{TSC} and dark current by varying photo-generation rate. The measurements are carried out with $b = 0.052$ K/s and $T_0 = 90$ K and $t_{rel} = 30$ min (a). Corresponding TSC-DOS (b).

Discussion

If we consider two photo-generation rates G_{01} and G_{02} such as $G_{01} \ll G_{02}$ in both cases, the gap states between the Fermi level and the quasi-Fermi level are filled. At $t = t_{rel}$, two quasi Fermi levels are obtained. The quasi Fermi level for G_{01} is then located much deeper than that for G_{02} ($E_c - E_{q01} > E_c - E_{q02}$). That means few traps will have a chance to contribute to the TSC current, and we expect a TSC curve smaller in magnitude when G_{01} is used. With this TSC, much information about the density of states in the gap will be missed.

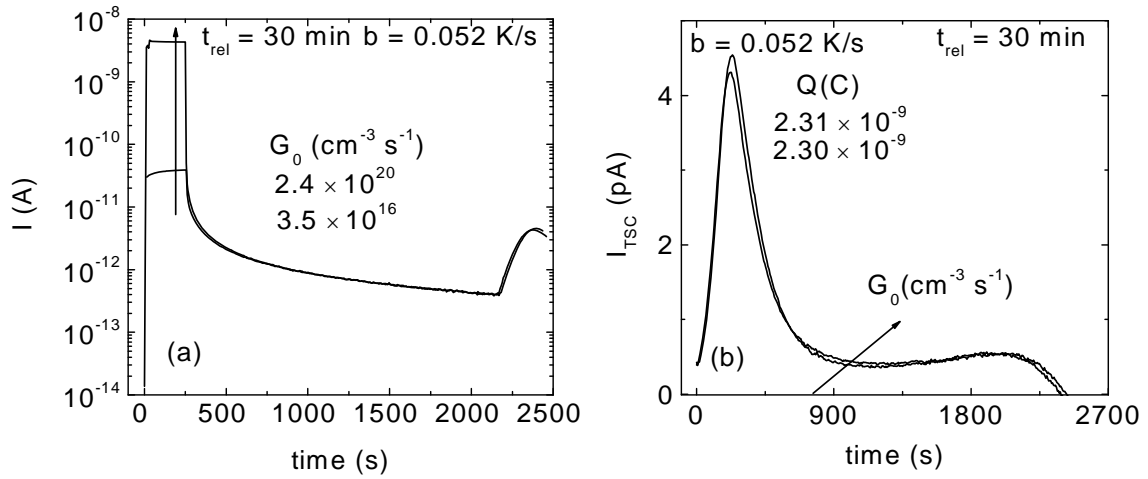


Figure 7.18: The current I against the time measured at 90 K. The curve describes 2 different steps. First step when the sample is illuminated for $t_{ill} = 3\text{min}$, second step when the illumination is turned off which leading to a decay of current. Two photo-generation rates are considered: $3.5 \times 10^{16} \text{ cm}^{-3} \text{ s}^{-1}$ and $2.4 \times 10^{20} \text{ cm}^{-3} \text{ s}^{-1}$ (a). Time-dependent TSC for both G_0 . The integrated charge Q is deduced for each I_{TSC} (b).

From the above explication we can easily understand that the knowledge of the photo-generation rate with which the sample must be illuminated such as a maximum of traps is filled, is important. Two TSC measurements have been performed using two photo-generation rates such as $G_{02}/G_{01} \approx 10^4$. The quasi Fermi level corresponding to G_{01} is 0.2518 eV and to G_{02} is 0.2516 eV (both quasi Fermi levels are calculated at $t = t_{rel}$). We observe that the quasi Fermi levels as well as the TSC curves are very similar. These results mean that the same trap levels are filled using either G_{01} or G_{02} . Furthermore, the TSC-DOS as well as the integrated charge Q are in both situations similar.

Advantages and limits of the TSC technique

The most important advantage of the TSC technique is to determine the profile of the density of states in the gap for $E_c - E < E_c - E_F$ as well as the capture coefficient c_n . In contrast, this technique does not give any information on the states lying in the region $E_c - E > E_c - E_F$ (0.578 eV is the position of Fermi level). We also have to underline that the drop of the TSC curve, indicating the thermal equilibrium, is not exactly determined. Indeed, a slight variation in the dark current involves a shift in the TSC drop. Therefore we estimate that the

corresponding drop in the DOS, at high energy and close to E_F , lies within an energy $2kT$ of E_F .

In addition, a great care must be taken in the $(\mu\tau)_n$ determination which is essential parameter in the DOS evaluation. We also note that for all calculations a value of $10 \text{ cm}^2 \text{ V}^{-1} \text{ s}^{-1}$ of the mobility has been considered. In the literature, the same value is used in amorphous silicon. In chapter 2 (section 2.3) we reviewed some features of microcrystalline silicon. Many investigations [61] assure that the transport is controlled by the disordered tissue which encapsulates the crystallites columns. From this, the use of the mobility value given above is justified.

The absorption coefficient α depends on the temperature. This dependence is not taken into account in the $(\mu\tau)_n$ evaluation. Only measurements, at room temperature, have been used. In fact, we expect a slight change in the DOS if $\alpha(T)$ was considered.

Referring to [19], the prefactor σ_0 introduced in Eq. 4.2 (see chapter 4) depends on the crystalline volume fraction. In our case a variation of σ_0 between 100 S cm^{-1} and 200 S cm^{-1} leads to a change in DOS which is smaller than 30 % (estimated error in DOS evaluation). In this work, the same value of $\sigma_0 = 200 \text{ S cm}^{-1}$ is used for all samples.

7.4 Conclusion

The combined experiment- and simulation approach of TSC, applied on $\mu\text{c-Si:H}$ with 34% crystalline volume fraction, has shown that the related σ_{TSC} corresponds to the weak retrapping regime. Also, the TSC-DOS profile emerges with a conduction band tail parameter of about 22 meV between 0.25 eV and 0.32 eV. Deeper in the gap, the slope decreases and a shoulder appears at high energy. Other parameters such as the retrapping time and the capture coefficient $c_n \approx 10^{-9} \text{ cm}^3 \text{ s}^{-1}$ are deduced.

In order to get more information about the characteristics of the TSC, different experimental parameters are varied. It has been demonstrated that the presence of the low-temperature peak is caused by the product of the rapid increase of the occupation function at 90 K and a decrease of $(\mu\tau)_n \times g(E)$. Furthermore, it has been shown that the obtained TSC-DOS do not vary in the probed parameter space.

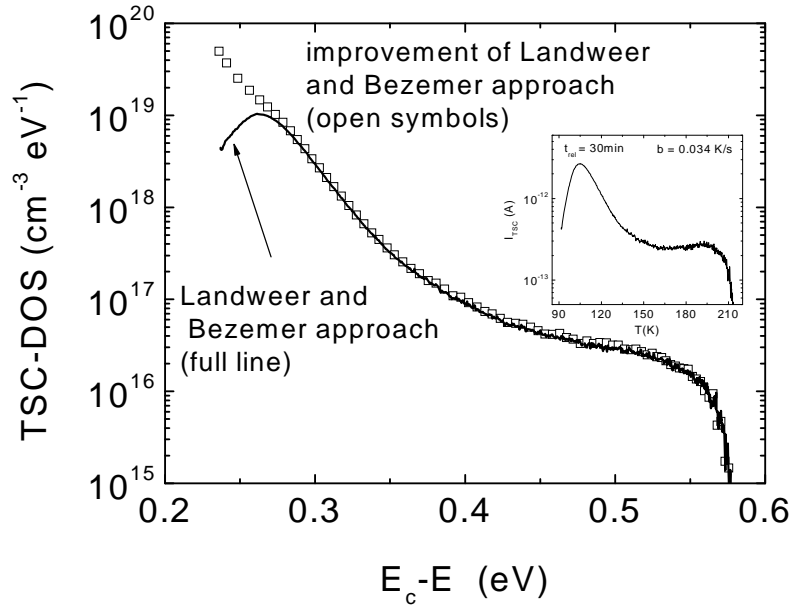


Figure 7.19: TSC-DOS evaluated from experimental σ_{TSC} obtained from measurement carried out with $b = 0.034$ K/s and $T_0 = 90$ K and $t_{rel} = 30$ min. Open symbols indicate the TSC-DOS from improvement of Landweer and Bezemer approach by taking into account Eq. (7.4). Full line shows TSC-DOS from Landweer and Bezemer approach with the approximation $f_0 \approx 1$. The related σ_{TSC} is shown in the inset.

7.5 Improvement of Landweer Bezemer approach

In section 7.3.2, the experimental results reveal that the low energy maximum in Fig. 7.14 is not a real image of the TSC-DOS. The aim of this section is to show that this peak is due to an artefact in the TSC-DOS evaluation, and the origin of the low temperature peak of TSC is related to shallow states in the conduction band tail.

Fig. 7.19 displays the TSC-DOS evaluated from the Landweer and Bezemer approach (Eqs. (5.13) and (5.14)) with the approximation $f_0 \approx 1$ (full line). Open symbols represent the TSC-DOS from improvement of the Landweer and Bezemer approach where the occupation function f_0 given by

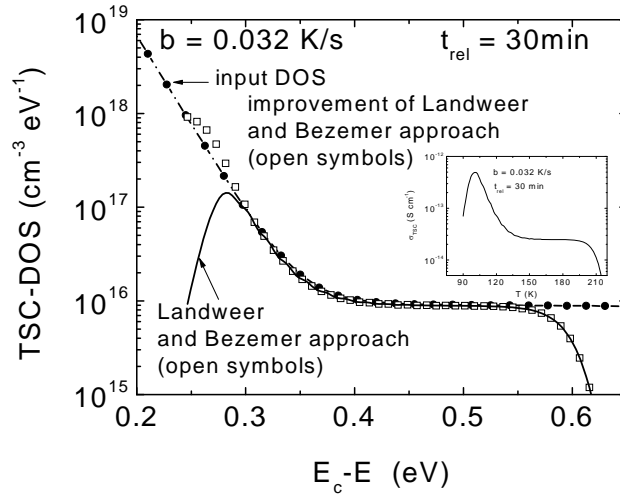


Figure 7.20: TSC-DOS evaluated from simulated σ_{TSC} obtained such that $b = 0.032$ K/s and $T_0 = 90$ K and $t_{rel} = 30$ min. Open symbols indicate the TSC-DOS from improvement of Landweer and Bezemer approach by taking into account Eq. (7.4). Full line shows TSC-DOS from Landweer and Bezemer approach with the approximation $f_0 \approx 1$. The related σ_{TSC} is shown in the same figure.

$$f_0(T_0, E_m) = \frac{1}{1 + e^{\frac{E_m - E_q}{kT_0}}} \quad (7.4)$$

is used for $T_0 = 90$ K. Same calculations (Eqs. (5.13), (5.14) and Eq. (7.43)) have been done using simulated data (see Fig. 7.20).

The results in Fig. 7.19 and 7.20 show that by considering Eq. 7.4, the peak of the TSC-DOS disappears. If all states are supposed fully occupied, a false TSC-DOS is obtained. This could be avoided if the relaxation time before TSC is taken shorter, resulting in a less pronounced peak in the related TSC-DOS at low energy.

In summary, with the assumption $f_0 \approx 1$, a false DOS is obtained at low energy. By considering the Eq. 7.4, the results show that the low-temperature peak of TSC is related to shallow states, partly occupied in the conduction band tail.

Chapter 8

Experimental and simulated results of TSC for the strong retrapping regime

This chapter provides experimental and simulated investigation of the strong retrapping regime. TSC is applied on a $\mu\text{c-Si:H}$ sample with high crystalline volume fraction in order to determine the related retrapping regime and then to extract the density of states in the gap. In addition more information, about trap parameters is gained with the support of the TSC simulation such as retrapping time and occupation function.

Furthermore, strong retrapping regime is examined by varying experimental parameters such as heating rate and generation rate.

In the last part of this chapter, TSC measurement is carried out on a second sample with high crystalline volume fraction. The related DOS as well as the retrapping regime are determined.

8.1 TSC for the sample with $R_c = 79\%$

The $\mu\text{c-Si:H}$ sample with a high crystalline volume fraction R_c of about 79% is introduced in Cryostat. The sample is first annealed in vacuum at the temperature 150 °C for 30 min. After that the sample is cooled down to $T_0 = 96$ K. The TSC measurement is carried out with $G_0 = 10^{20} \text{ cm}^{-3} \text{ s}^{-1}$, $t_{rel} = 900$ s and $b = 0.053$ K/s. The sample with a thickness of about 2 μm has coplanar electrodes separated with a distance of 1 mm. A voltage of 100 V is applied in order to measure the current. It should be noted that a penetration depth of about 1 μm ($d \approx 1/\alpha$) is considered in the evaluation of TSC conductivity. The parameter α is the absorption coefficient which corresponds to a wavelength $\lambda = 640$ nm. This wavelength is used to illuminate the sample.

Figure 8.1 displays temperature-dependent TSC and dark conductivity. An initial rise of σ_{TSC} appears in the temperature range between 96 K and 112 K. After that, σ_{TSC} increases monotonously to high values with increasing the temperature and then drops around 250 K. It should be noted that σ_d crosses σ_{TSC} at $T_{F,exp} = 206.7$ K.

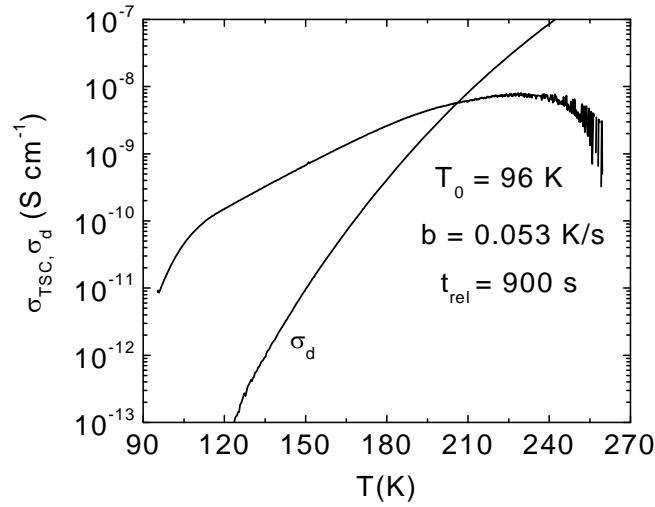


Figure 8.1: Temperature-dependent TSC and dark conductivity. The measurements were carried out at $T_0 = 96$ K, $b = 0.053$ K/s, $t_{rel} = 3$ min and $G_0 = 2.4 \times 10^{20}$ cm $^{-3}$ s $^{-1}$.

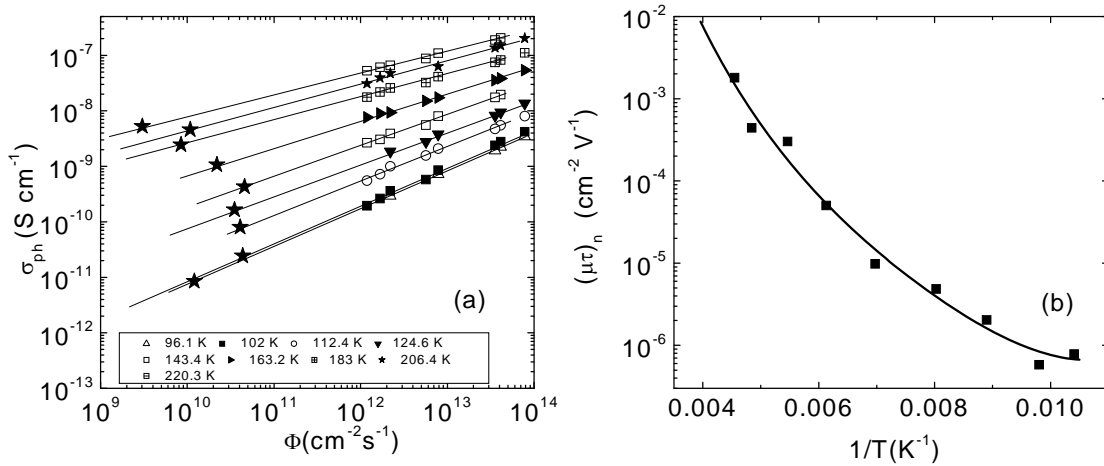


Figure 8.2: Photoconductivity at different temperatures between 96 K and 220.3 K over a range of photon fluxes Φ between 10^{12} cm $^{-2}$ s $^{-1}$ and 10^{14} cm $^{-2}$ s $^{-1}$ respectively. Full lines represent the linear fit. For each temperature T , a photon flux is determined by extrapolating the experimental data to low Φ such that $\sigma_{ph} = \sigma_{TSC}$. The star symbol shows the data determined from Eqs. 5.11 and 5.12 (a). Mobility lifetime product of free electrons $(\mu\tau)_n$ against $1/T$. Square symbol indicate $(\mu\tau)_n$, according to Eq. (5.10). A good fit of $(\mu\tau)_n$ data is obtained with polynomial function of order 4 (b).

To determine the retrapping regime we also examined both conditions: $\sigma_{TSC} = \sigma_d$ and $\sigma_{TSC} \ll \sigma_d$ where ν_{eff} could be calculated. We recall that when $\nu_{eff} < \nu_0$ we expect strong retrapping, while weak retrapping for $\nu_{eff} \approx \nu_0$. According to Eq. 5.15, $\nu_{eff} = 1.9 \times 10^8 \text{ s}^{-1}$ is calculated at $T_{F,exp} = 206.7 \text{ K}$ ($\sigma_{TSC} = \sigma_d$). At higher temperature where $\sigma_{TSC} \ll \sigma_d$, ν_{eff} drastically becomes smaller. In addition, knowing from literature that ν_0 only takes the values between 10^{11} s^{-1} and 10^{12} s^{-1} , we can state that the TSC for this sample corresponds to the strong retrapping regime because ν_{eff} is much smaller than ν_0 .

Figure 8.2(a) shows photoconductivity measurements carried out in order to get the profile of $(\mu\tau)_n(T)$. According to Eq. 5.10 the mobility lifetime is calculated for each temperature. Good fit of $(\mu\tau)_n(T)$ values is obtained using polynomial function of order 4 (Fig. 8.2(b)). We note that the exponential fit is not chosen because with this function a bad fit of experimental data is obtained.

8.1.1 Density of states and simulation

We recall that, from chapter 6 for the strong retrapping regime, the maximum concentration of emitted electrons come from traps at the energy $E_c - E_q$ (quasi Fermi level) expressed by

$$E_c - E_q = kT \ln \left(\frac{200 S cm^{-1}}{\sigma_{tot}} \right) \quad (8.1)$$

with $\sigma_{tot} = \sigma_{ph} + \sigma_d$

To describe the DOS of this sample, $E_c - E_q$ will be considered as energy scale.

Fig. 8.3(a) displays the experimental density of states represented with full line. A peak at low energy is followed by an exponential decrease of the DOS which can be described with one exponential function characterised with a parameter of about $E_0 = 85 \text{ meV}$ between 0.29 eV and 0.35 eV. The drop at high energy is related to the TSC drop in TSC which indicates the thermal equilibrium.

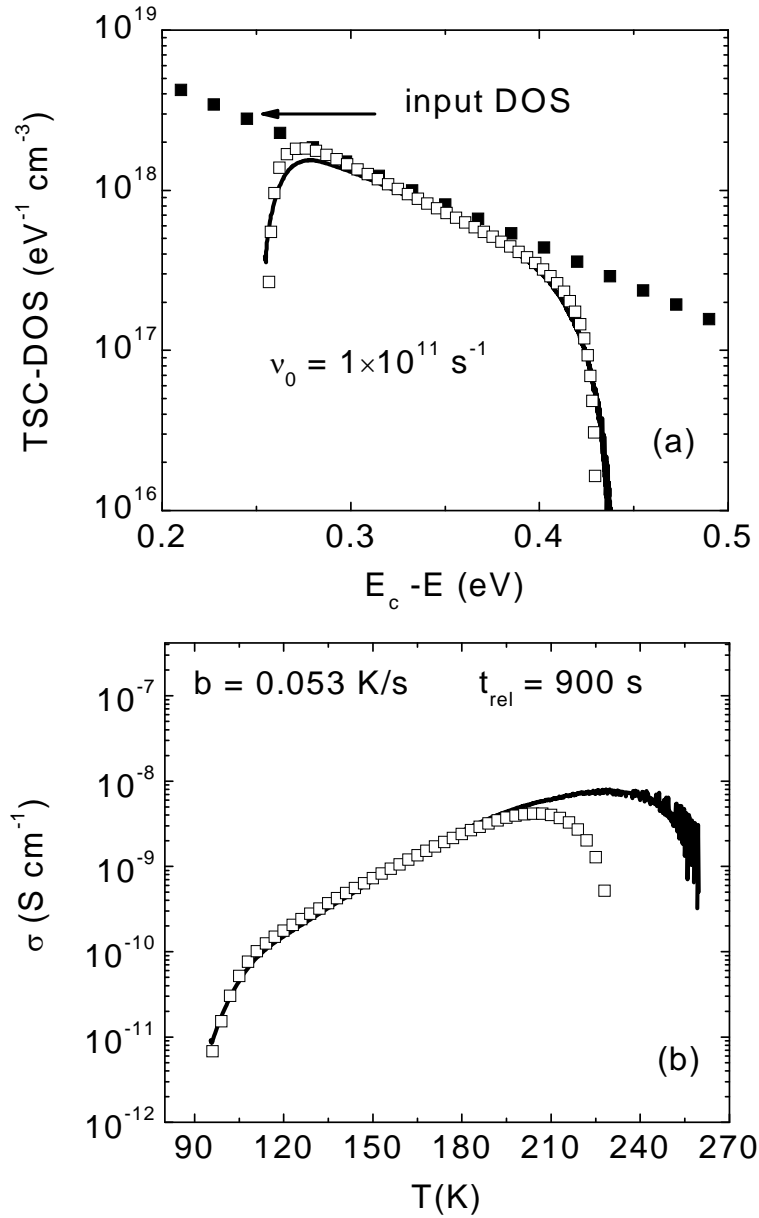


Figure 8.3: TSC-DOS against $E_c - E$. Full line indicates TSC-DOS obtained from experimental σ_{TSC} . Open symbols indicate reconstructed DOS evaluated from simulated σ_{TSC} . The simulation is performed with input DOS shown with full symbols. In the simulation, ν_0 is taken equal $1 \times 10^{11} \text{ s}^{-1}$ (a). Temperature-dependent simulated (square symbols) and experimental (full line) σ_{TSC} (b).

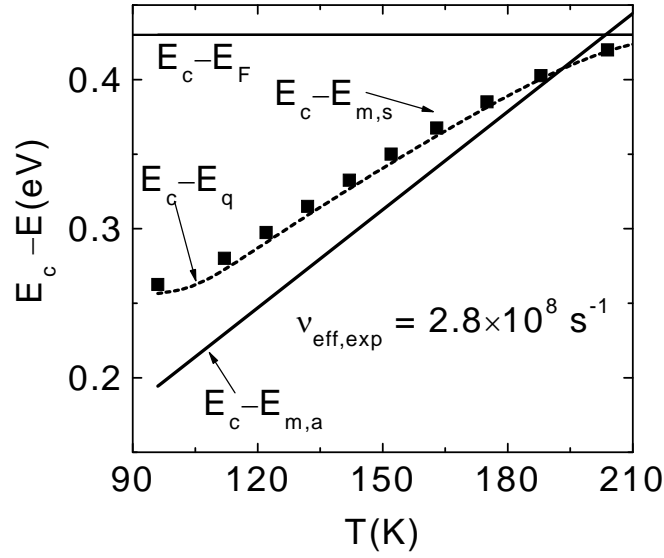


Figure 8.4: Temperature-dependent computed $E_c - E_{m,s}$ (full line) and analytical $E_c - E_{m,a}$ (square symbol) peak emission energy, quasi-Fermi level $E_c - E_q$ (dashed line) and $E_c - E_F$. Good overlap is shown between $E_c - E_q$ and $E_c - E_{m,s}$. However, $E_c - E_{m,s}$ and $E_c - E_{m,a}$ disagree.

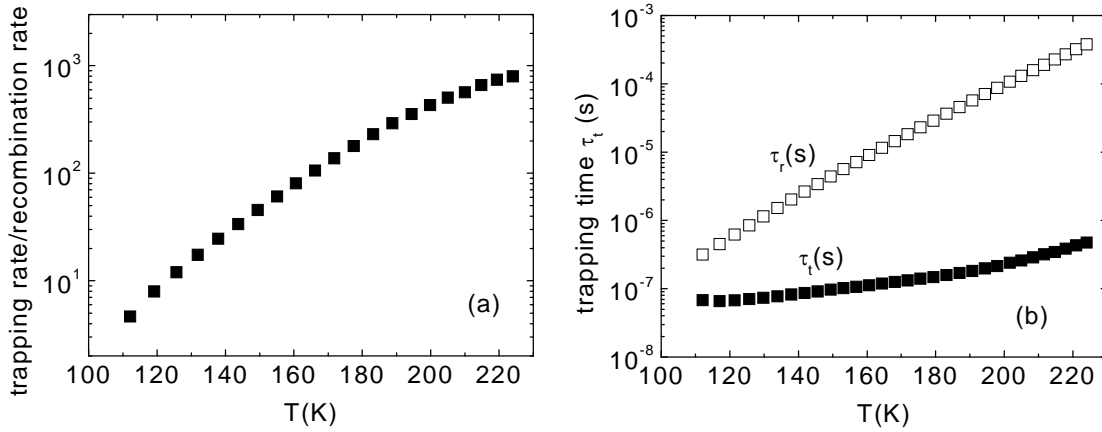


Figure 8.5: The temperature dependence of the ratio retrapping rate to recombination rate (a). Retrapping time $\tau_t(T)$ is represented with full symbol, while the recombination time $\tau_r(T)$ is represented with open symbol (b).

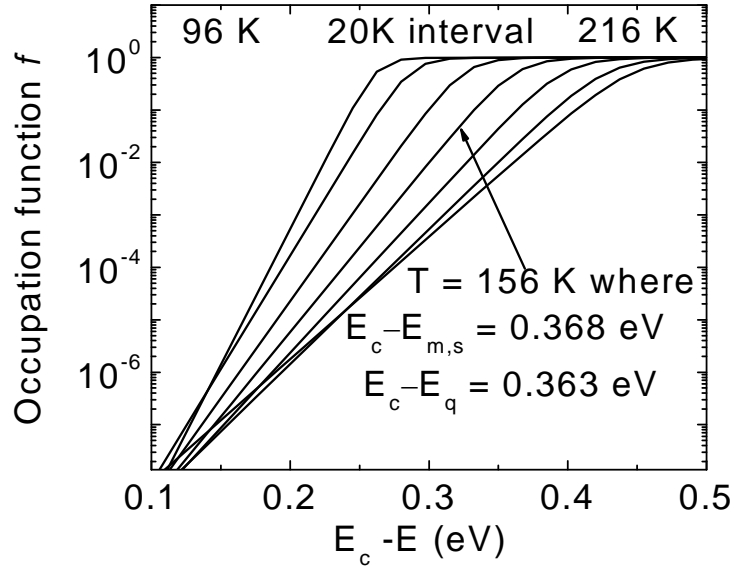


Figure 8.6: Occupation function f numerically determined for different temperature between 90 K and 216 K at 20 K intervals. f at is Boltzmann-like for each temperature. The strong retrapping regime is underlined. An example of f is shown at $T = 156$ K, where $E_c - E_q = 0.363$ eV and $E_c - E_{m,s} = 0.368$ eV (b).

To get more information about the retrapping regime a simulation has been performed with an input DOS such that $g(E_q) = 7.15 \times 10^{19} \text{ eV}^{-1} \text{ cm}^{-3} \exp\left(-\frac{(E_c - E_q)}{E_0}\right)$. Other parameters are introduced in the simulation such as: $T_0 = 96$ K, $t_{rel} = 900$ s, $E_c - E_F = 0.43$ eV, $E_0 = 85$ meV and $v_0 = 1 \times 10^{11} \text{ s}^{-1}$. The recombination time is obtained from Fig. 9.2(b). We note that $\mu = 10 \text{ cm}^2/\text{Vs}$. It should be noted that the best fit (Fig. 8.3) between simulated and experimental TSC-DOS is obtained only if $E_c - E_q$ is considered as energy scale.

Open symbols represent the simulated data of σ_{TSC} in Fig. 8.3(b). A very good overlap is shown between simulated and experimental σ_{TSC} especially between 96 K and 200 K. However a discrepancy at high temperature for σ_{TSC} is detected. This is due to the poor overlap between simulated and experimental σ_d .

Figure 8.3(a) shows a good agreement between experimental and simulated TSC-DOS. It is important to point out that a very slight change is obtained between the experiment and the simulation data (for σ_{TSC} or TSC-DOS) in Fig. 8.3 when v_0 varies between 10^{11} s^{-1} and 10^{12} s^{-1} . That means for strong retrapping regime an accurate value of v_0 (or capture coefficient c_n , $v_0 = c_n N_c$) can not be deduced.

Figure 8.4 illustrates temperature-dependent E_c-E . It can be seen that $E_c-E_{m,s}$ represented with full line agrees very well with E_c-E_q . In contrast, a discrepancy is shown between $E_c-E_{m,s}$ and $E_c-E_{m,a}$. We note that $\nu_{eff} = 2.8 \times 10^8 \text{ s}^{-1}$ is obtained when $E_c-E_{m,s}$ cross E_c-E_F at $T_{F,sim} = 204 \text{ K}$.

Figure 8.5(a) shows the ratio r , retrapping rate to recombination rate, against the temperature. Over the whole range of the temperature, r varies between 5 and 500.

Figure 8.5(b) reveals retrapping time $\tau_r(T)$ evaluated from Eq. (6.9) and recombination time $\tau_r(T)$. We observed that $\tau_r(T)$ is larger than $\tau_i(T)$.

Figure 8.6 shows the occupation function f against the temperature. f is evaluated at different temperatures between 96 K and 216 K with 20 K interval. At the temperature 156 K, $E_c-E_{m,s} = 0.368 \text{ eV}$ and $E_c-E_q = 0.363 \text{ eV}$. In addition, Fig. 8.6 reveals that f is Boltzmann function.

8.1.2 Discussion

The TSC conductivity (see Fig. 8.1), for the sample with high crystalline volume fraction R_c , exhibits very high values especially at high temperature, compared with the sample having small R_c . In addition the mobility lifetime product is 2 orders of magnitude larger than that of the sample with $R_c = 34 \%$. The electrons in the sample with $R_c = 79 \%$ have more chance to undergo the retrapping effect. This agrees well with the calculated value of ν_{eff} which is at least 3 orders of magnitude smaller than ν_0 . Also, the results show high values of r ($r \gg 1$), and the corresponding occupation function is Boltzmann like. Consequently the TSC of this sample corresponds to the strong retrapping regime. In addition, the profile of the density of states is characterised with the parameter $E_0 = 85 \text{ meV}$. Furthermore, the low energy peak in TSC-DOS (Fig. 8.3(a)) is not a real image of the DOS. This peak is related to an artefact in the TSC-DOS evaluation.

The experimental data are well reproduced from the simulation. Nevertheless, the value of ν_0 can not be obtained because the quality of the overlap between simulated and experimental σ_{TSC} is the same when ν_0 varies between 10^{11} s^{-1} and 10^{12} s^{-1} . For this reason complimentary measurements are necessary to get the value of ν_0 (see chapter 9).

8.2 Parameter variation

8.2.1 Heating rate variation

To get more information about the TSC-DOS of this sample, we have varied different parameters such as heating rate b and generation rate G_0 .

Fig. 8.7(a) displays different measurement cycles of excess currents for $T_0 = 96$ K with $t_{rel} = 900$ s and $G_0 = 2.4 \times 10^{20} \text{ cm}^{-3} \text{ s}^{-1}$. The constant heating rate b is varied between 0.024 K/s and 0.053 K/s. At low temperature, the data approximately exhibit the same initial rise until 103 K. A slight increase in the current is observed with increasing b .

Figure 8.7(b) reveals I_{TSC} against the time for different heating rates between b . The integrated charge Q such that $Q = \int I_{TSC} \times dt$ is calculated for each TSC curve. A slight increase of about 25% of Q is observed with increasing b . This increase is related to the error evaluated when the current is subtracted from dark current.

Fig. 8.8 represents the TSC-DOS corresponding to σ_{TSC} in Fig. 8.7(a). Small variation in TSC-DOS about 30% is observed upon b change. This variation is similar to the error which is estimated during $(\mu\tau)_n$ determination.

Discussion

By varying the heating rate b , the general shape of TSC does not change. However, a small increase in σ_{TSC} is detected with increasing b . The increase of the current is due to a stronger effective emission (nett = emission – trapping) of the trapped carriers to the conduction band, caused by b increase. We also note that the retrapping effect decrease the effective emission rate of trapped electrons. For this reason the variation of σ_{TSC} upon change of b in the case of strong retrapping is less important compared with that in the weak retrapping regime.

Small variation in the TSC-DOS is observed with increasing b . Therefore, we can consider that the density of states does not depend on b in the case of strong retrapping regime.

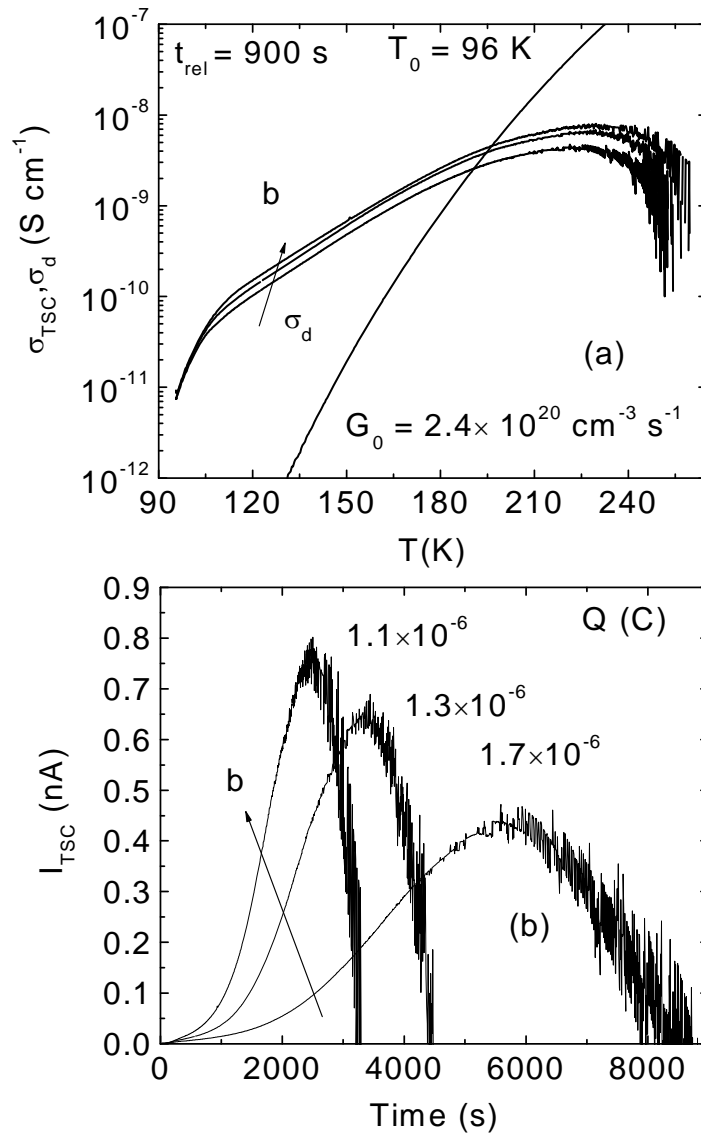


Figure 8.7: Temperature-dependent σ_{TSC} and σ_d by varying b between 0.024 K/s and 0.053 K/s (a). Time-dependent TSC current for different b . The integrated charge Q is deduced for each I_{TSC} (b).

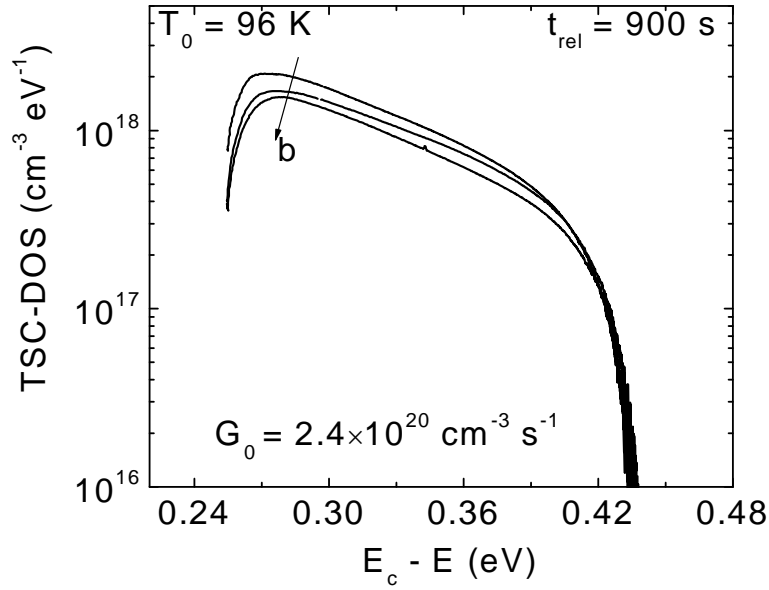


Figure 8.8: TSC-DOS obtained by varying b between 0.034 K/s and 0.053 K/s. The corresponding σ_{TSC} are represented in Fig. 8.7(a).

8.2.2 Photogeneration rate variation

Fig. 8.9(a) displays two different TSC carried out at two different photo-generation G_0 rates, $G_{01} = 2 \times 10^{16} \text{ cm}^{-3} \text{ s}^{-1}$, and $G_{02} = 2 \times 10^{20} \text{ cm}^{-3} \text{ s}^{-1}$, with which the sample is illuminated at 96 K. The other experimental parameters are kept the same: $b = 0.053 \text{ K/s}$ and $t_{rel} = 900 \text{ s}$.

We note that the sample was firstly illuminated with small G_0 and then after TSC measurement, it was cooled down and again illuminated at 96 K with the second G_0 .

Figure 8.9 does not reveal significant difference in current when G_0 changes of 4 orders of magnitude. The corresponding TSC-DOS curves equally are very similar.

Discussion

In the case of strong retrapping, the TSC current is not affected by a variation of photogeneration rate which changes of 4 orders of magnitude. The same traps, in both cases for $E_c - E > E_c - E_q$ are filled. Consequently the obtained TSC-DOS slightly vary.

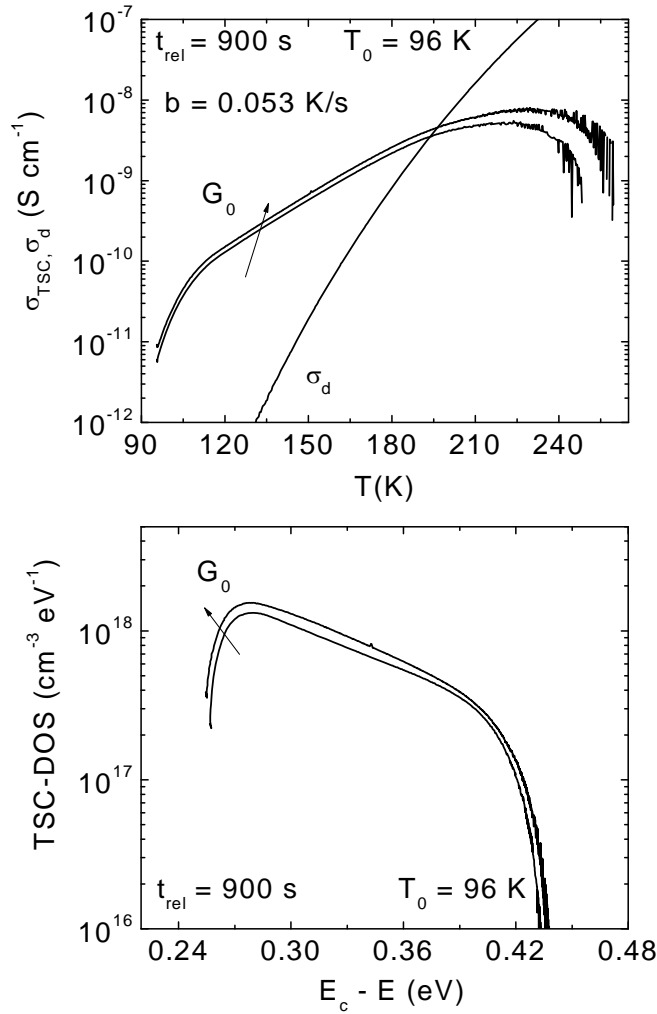


Figure 8.9: Temperature-dependent σ_{TSC} and dark conductivity by varying photo-generation rate: $G_{01} = 10^{20} \text{ cm}^{-3} \text{ s}^{-1}$, $G_{02} = 10^{16} \text{ cm}^{-3} \text{ s}^{-1}$. The measurements are carried out with $b = 0.053 \text{ K/s}$, $T_0 = 96 \text{ K}$ and $t_{rel} = 900 \text{ s}$ (a). Corresponding TSC-DOS (b).

8.3 Conclusion

TSC measurements with a simulation have been performed on a $\mu\text{c-Si:H}$ sample with high crystalline volume fraction (79%). Evidence of the strong retrapping has been provided and a profile of TSC-DOS is determined with a parameter $E_0 = 85 \text{ meV}$ between 0.29 eV and 0.35 eV .

The variation of different experimental parameters does not change the retrapping regime. Also the obtained TSC-DOS does not vary in the probed parameter space.

8.4 Experimental and simulated results for $\mu\text{-Si:H}$ with $R_c = 88\%$

In this section TSC is performed on the $\mu\text{-Si:H}$ sample with crystalline volume fraction about 88 %. At 90 K, the sample is illuminated for 3min. After a relaxation time $t_{rel} = 900\text{s}$, the sample is heated with $b = 0.055 \text{ K/s}$.

Figure 8.10(a) shows σ_{TSC} and σ_d against the temperature. For this sample, the initial rise of σ_{TSC} is characterized with a sharp increase until 101 K. Between 101.4 K and 200 K, TSC conductivity increases monotonously. At $T = 200 \text{ K}$, an abrupt increase of the conductivity appears until the thermal equilibrium is reached.

The DOS determination according to Eq. 5.19 shows a high density of states about $10^{19} \text{ cm}^{-3} \text{ eV}^{-1}$ around the Fermi level ($E_c - E_F = 0.572 \text{ eV}$). This value is very high and certainly, it does not correspond to the real DOS of the sample. Then we propose to extrapolate, in Fig. 8.10(a), σ_{TSC} data from 200 K to the cross with σ_d where $T^* = 222 \text{ K}$. The extrapolation is represented with dashed line (see Fig. 8.10(a)). The new TSC conductivity between 90K and 222 K is labelled σ_{TSC}^* . The value of ν_{eff} at T^* is equal to $0.7 \times 10^{11} \text{ s}^{-1}$.

Figure 8.10(b) shows the mobility lifetime product $(\mu\tau)_n(T)$ against $1/T$ obtained according to Eq. (5.10). A good fit of the experimental data is described by an exponential function. We note that $(\mu\tau)_n(T)$ is obtained in a region where γ , light intensity exponent of photoconductivity measurement, is between 0.865 and 0.935.

Figure 8.11 shows the TSC-DOS related to σ_{TSC} and σ_{TSC}^* . As has been already mentioned, a high DOS is observed around Fermi level ($E_c - E_F = 0.5715 \text{ eV}$), if σ_{TSC} is considered. The DOS related to σ_{TSC}^* is labelled TSC-DOS*. From an exponential fit ($g(E) \approx \exp(-(E_c - E)/E_0)$ between 0.29 eV and 0.33 eV, $E_0 = (48 \pm 2) \text{ meV}$

To get more information about the retrapping regime nature we plot in Fig. 8.12(a) the ratio r , retrapping rate to recombination rate as well as the recombination $\tau_r(T)$ and retrapping $\tau_i(T)$ time in Fig. 8.12(b). We note that $\tau_r(T)$ is obtained from Fig. 8.10(b) ($\mu = 10 \text{ cm}^2/\text{Vs}$), and $\tau_i(T)$ is obtained by application of Eq. 6.9 using the DOS evaluated from σ_{TSC}^* . In Fig. 8.12(a), over a region of temperatures between 101 K and 200 K, r varies between 0.0303 and 0.899, indicating the presence of the weak retrapping regime. However between 200 K and 221 K, r reaches the value 1.386. This shows a change of the retrapping regime from weak to strong.

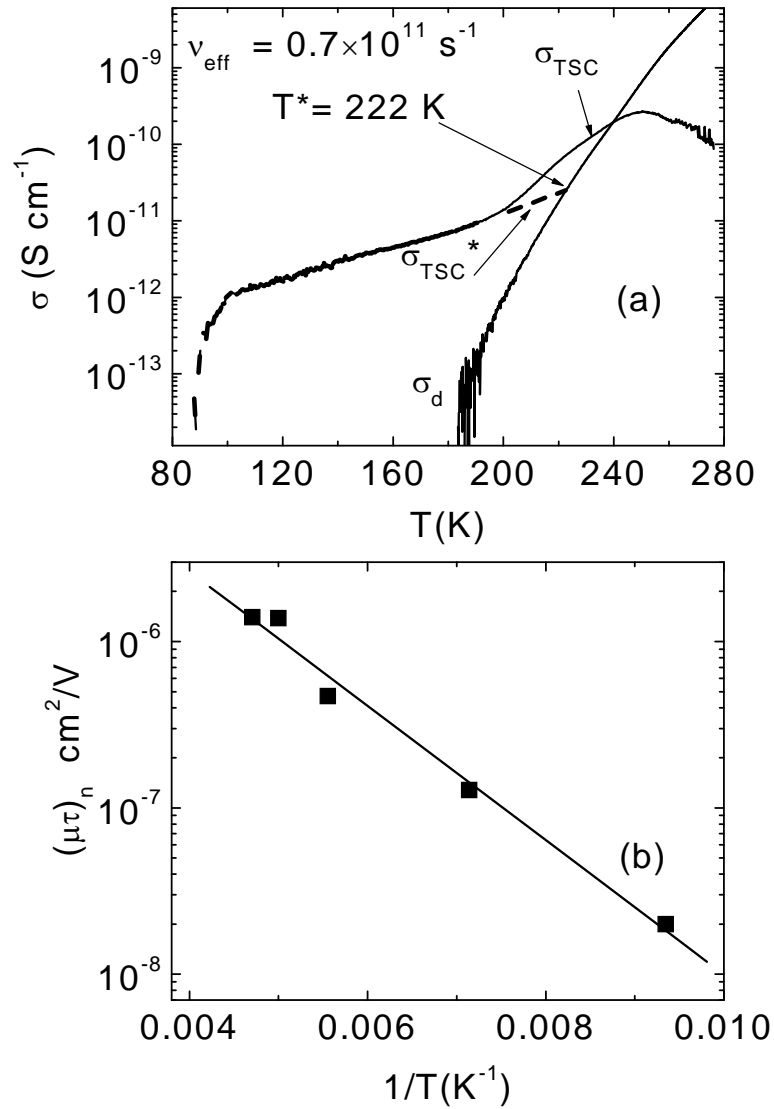


Figure 8.10: Temperature-dependent σ_{TSC} and σ_d . The TSC measurements were carried where $T_0 = 90$ K, $b = 0.055$ K/s, $t_{rel} = 3$ min and $G_0 = 2.4 \times 10^{20}$ cm⁻³ s⁻¹. Dashed line represents the extrapolated data of σ_{TSC} from $T = 200$ K to the cross with σ_d , where $T^* = 222$ K. The new TSC conductivity, between 90 K and 222 K, is labelled σ_{TSC}^* (a). Mobility lifetime product of free electrons $(\mu\tau)_n$ obtained from photoconductivity measurements (b).

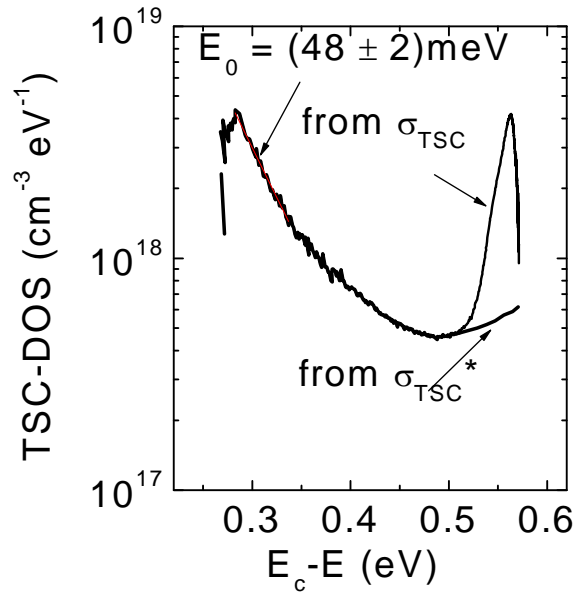


Figure 8.11: TSC-DOS profiles determined from σ_{TSC}^* and in σ_{TSC} in Fig. 8.10(a). From exponential fit ($DOS \approx \exp(-(E_c - E)/E_0)$) between 0.29 eV and 0.33 eV, $E_0 = (48 \pm 2)$ meV.

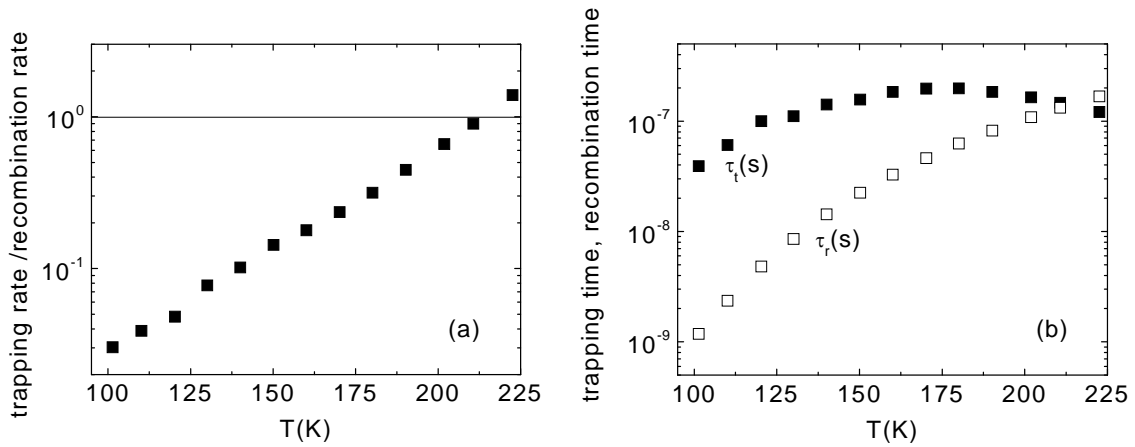


Figure 8.12: The temperature dependence of the ratio, retrapping rate to recombination rate. Square symbol shows r which corresponds to σ_{TSC}^* (a). Recombination time $\tau_r(T)$ is represented with open symbol, while the retrapping time $\tau_i(T)$ is represented with full symbol (b).

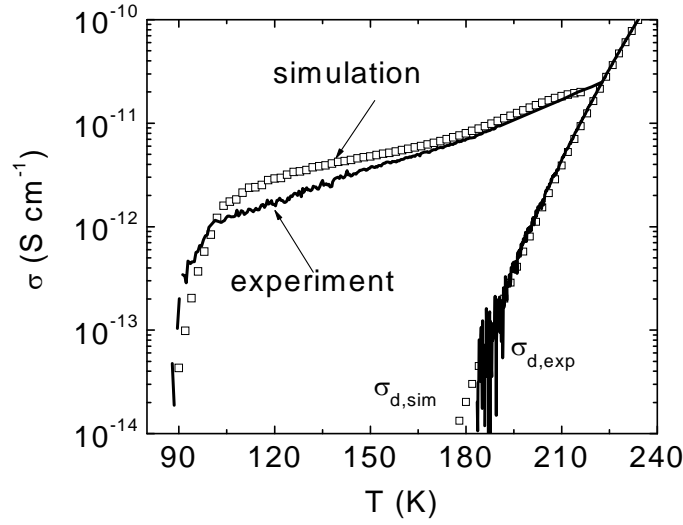


Figure 8.13: Experimental and simulated data of σ_{TSC}^* and σ_d depending on the temperature. σ_{TSC}^* is taken from Fig. 8.10(a).

Fig. 8.13 represents the simulated result of σ_{TSC}^* . σ_{TSC}^* is taken from Fig. 8.10(a). For the simulation, the input DOS is approximated by TSC-DOS*. Input DOS is the sum of 2 exponential functions, where the first parameter $E_0 = 48$ meV is between 0.29 eV and 0.33 eV, while the second parameter $E_0 = 127$ meV is between 0.33 eV and 0.486 eV. It should be noted that a best fit of σ_{TSC}^* ; especially in the region $190 \text{ K} < T < 215 \text{ K}$ (Fig. 8.13) is obtained only if a bump is added to the input DOS. The maximum of the bump at 0.6 eV is equal to $0.8 \times 10^{18} \text{ cm}^{-3} \text{ eV}^{-1}$. The full width at half maximum (FWHM) is equal to 0.16 eV.

8.4.1 Discussion

Unusually, σ_{TSC} of this sample reveals 2 different slopes in the quasi steady state region (see Fig. 8.10(a)). Indeed, the profile of σ_{TSC} at 200 K changes abruptly before the thermal equilibrium. The abrupt change around 200 K in Fig. 8.10(a) is attributed to a change in the retrapping regime nature where the ratio r starts to increase. In addition, the simulation results in Fig. 8.13, shows that to reproduce correctly σ_{TSC}^* , a bump must be considered. The energetic position of the bump corresponds to the abrupt change of σ_{TSC} around 200 K. This means that the behaviour of σ_{TSC} could be due to the existence of new defects near to the Fermi level which correspond to dangling bonds.

Then we propose that the origin of this change of σ_{TSC} is related to the defect in the gap near to Fermi level, causing a change in the retrapping regime.

Chapter 9

Density of states from other techniques

This chapter deals with an investigation of $\mu\text{-Si:H}$ from photoconductivity measurements which determine the density of states. These techniques present a complementary study with the aim to determine the capture coefficient c_n (or ν_0). The techniques are: intensity-dependence of steady-state photoconductivity (SSPC), steady state photocarrier grating (SSPG) and low-frequency modulated photocurrent (LF-MPC).

In section 9.1, these techniques briefly are described. Section 9.2 presents the experimental results of DOS from TSC and photoconductivity measurements followed by a discussion. Finally a conclusion of this chapter is addressed.

9.1 Photoconductive techniques

9.1.1 SSPC

In this technique the photocurrent has been measured over a large range of photon-fluxes F . Different temperatures have been taken into account. In Fig. 9.1(a) we show an example of SSPC measurement at the temperature 140 K. F is varied between $10^{13} \text{ cm}^{-2} \text{ s}^{-1}$ and $5 \times 10^{16} \text{ cm}^{-2} \text{ s}^{-1}$. Using [106], the density of states is calculated by [106]

$$g(E_{fn}) = \frac{(1-\gamma)\mu_n}{(\mu\tau)_n c_n \gamma kT} \quad (9.1)$$

$$E_c - E_{fn}(T) = kT \ln \frac{(200 \text{ S cm}^{-1})}{\sigma_{tot}} \quad (9.2)$$

$$\text{with } \sigma_{tot} = \sigma_{ph} + \sigma_d$$

According to Eq. 9.1, we can easily see that the knowledge of $g(E_{fn})$ requires the determination of γ , defined by $I_{ph} \propto F^\gamma$, c_n , capture coefficient, as well as $(\mu\tau)_n$.

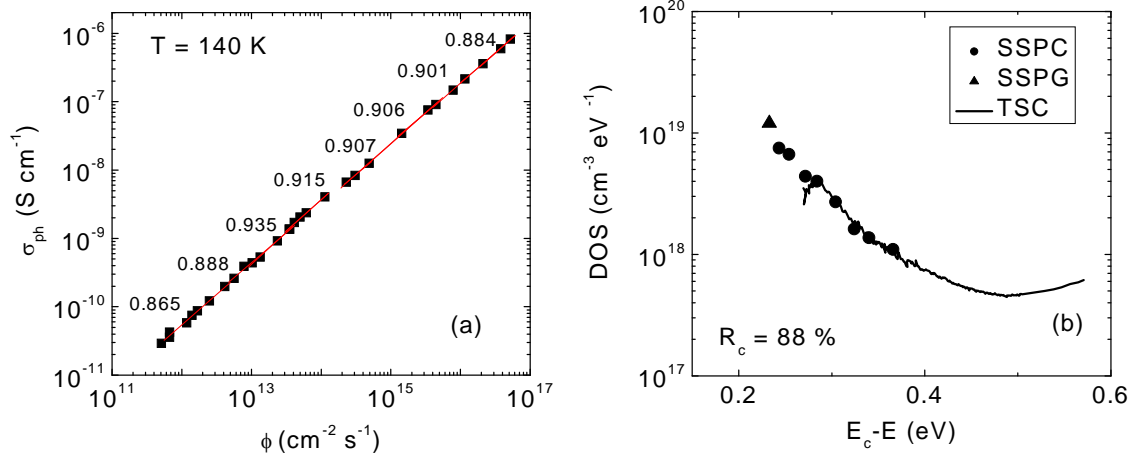


Figure 9.1: Photoconductivity measurements performed at $T = 140$ K over a range of photon fluxes F between 10^{13} $\text{cm}^{-2} \text{s}^{-1}$ and 10^{17} $\text{cm}^{-2} \text{s}^{-1}$ (a). An example showing the calibration of the DOS data from SSPC and SSPG with TSC measurements. c_n is around 1.5×10^{-9} $\text{cm}^3 \text{s}^{-1}$.

Then we suggest to calculate γ in several small ranges of F , as has been shown in Fig. 9.1. For each range, we calculate the quasi Fermi level $E_c - E_{fn}$ (see Eq. 9.2) and $(\mu\tau)_n$. The parameter c_n is unknown, then we calibrate the DOS from SSPC with that from TSC in order to estimate the value of c_n . The measurement in Fig. 9.1 belong to the sample with $R_c = 88\%$. In Fig. 9.1(b), we show the result of the DOS from SSPC, c_n is around 1.5×10^{-9} $\text{cm}^3 \text{s}^{-1}$. It should be noted that the DOS value obtained from SSPC measurements in a region of F , where $\sigma_{ph} = \sigma_{TSC}$ are not presented because this technique is consistent only at high photon-fluxes.

9.1.2 SSPG

Here the sample is illuminated with 2 coherent laser beams of intensity I_1 and I_2 ($I_1 \ll I_2$) (for more detail see chapter 4). Schmidt *et al.* [107] proposed an analytical expression of the DOS based on the knowledge of some parameters obtained from SSPG measurements. The equation is given

$$g(E_{fn}) = \frac{q\mu_n G_0}{c_n k_B T \sigma_0} \left[\frac{1}{1 + \frac{G_1}{G_2}} \sqrt{\frac{2\sigma_0}{\gamma\sigma_1(1-\beta_{lim})}} - 1 \right] \quad (9.3)$$

σ_I is the photoconductivity when the sample is illuminated by a light whose intensity is I_1 , while σ_0 is measured from $I_1 + I_2$. G_0 is the photo-generation rate obtained from $I_1 + I_2$. G_1 and G_2 are the photo-generation rates from I_1 and I_2 respectively. β_{lim} is the ratio u_c/u_{inc} measured at high grating period Λ , where $\beta(\Lambda)$ curve tends towards a constant value. Here again, we notice that the parameter c_n (capture coefficient) is unknown; a calibration of SSPG and TSC data is necessary to get the DOS from this technique and essentially to estimate the value of c_n . In the same figure (Fig. 9.1(b)), we plot the DOS value obtained at the temperature $T = 140$ K by application Eq. 9.3, and where $E_c - E_{fn} = 0.233$ eV.

9.1.3 LF-MPC

The sample in LF-MPC technique is illuminated with monochromatic light modulated by a chopper whose frequency ω varies between 0 and 200 Hz. As a result, a phase φ between the excitation and the modulated photocurrent of the sample is measured by a lock-in amplifier SR530. This phase shift is due to the interaction between the free carriers created under illumination and localised states in the gap. At low frequency and according to [108], it has been shown that the $\tan\varphi$ is a function linearly depending on the frequency ω ; and the slope is related to the density of states taken at the quasi Fermi level. This equation is expressed by

$$g(E_{fn}) = \frac{2G_{dc}}{k_B T} \frac{\tan\varphi}{\omega} \quad (9.4)$$

G_{dc} denotes the continuous component of the modulated photo generation rate.

9.2 Experimental results

Figure 9.2(a) summarizes the experimental DOS from TSC (full line), SSPC, LF-MPC and SSPG (symbols) of the sample with $R_c = 34\%$. With open symbols we show the DOS data at 160 K. Data of DOS from SSPC and SSPG measurements are adjusted with the DOS data from TSC for a capture coefficient c_n taken between 1 and $3 \times 10^{-9} \text{ cm}^3 \text{ s}^{-1}$.

Figure 9.2(b) presents the DOS only from SSPC measurements for the sample with $R_c = 52\%$. Different temperatures between 130 K and 283 K have been taken into account. Since the samples, with R_c equals 34% and 52%, are deposited with the same deposition parameters (only $SC = [\text{SiH}_4] / [\text{H}_2]$ differs), we suggest to calculate the DOS at the same c_n value taken for the sample with $R_c = 34\%$.

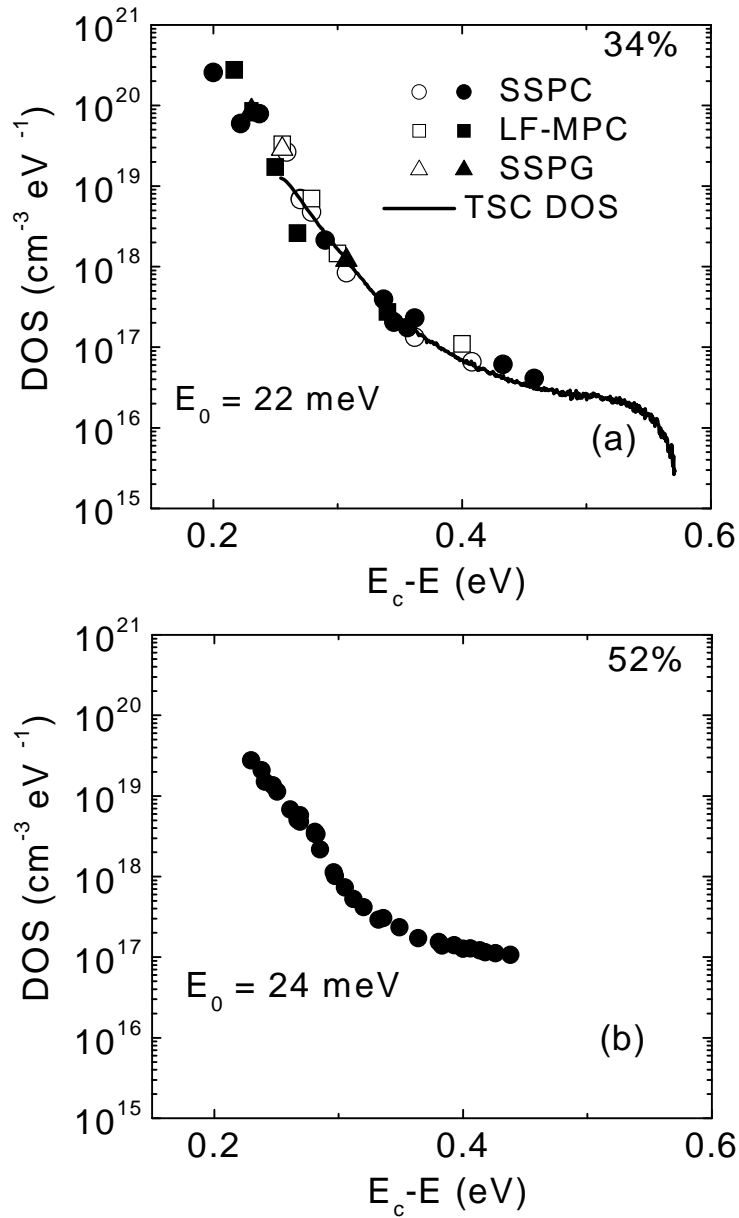


Figure 9.2: Density of states from TSC (full line) and photoconductivity measurements SSPC, LF-MPC and SSPG (symbols) for the sample with $R_c = 34\%$. Full symbols represent the photoconductivity measurements at temperature 90, 110, 140, 180, and 200 K. Open symbols show DOS data at 160 K. The band tail parameter $E_0 = 22 \text{ meV}$ (a). SSPC-DOS measurements performed on the sample with $R_c = 52\%$ at the temperatures between 130 K and 283 K. For calculation the capture coefficient c_n is taken equals $1.5 \times 10^{-9} \text{ cm}^3 \text{ s}^{-1}$. The band tail parameter between 0.23 eV and 0.25 eV is $E_0 = 24 \text{ meV}$ (b).

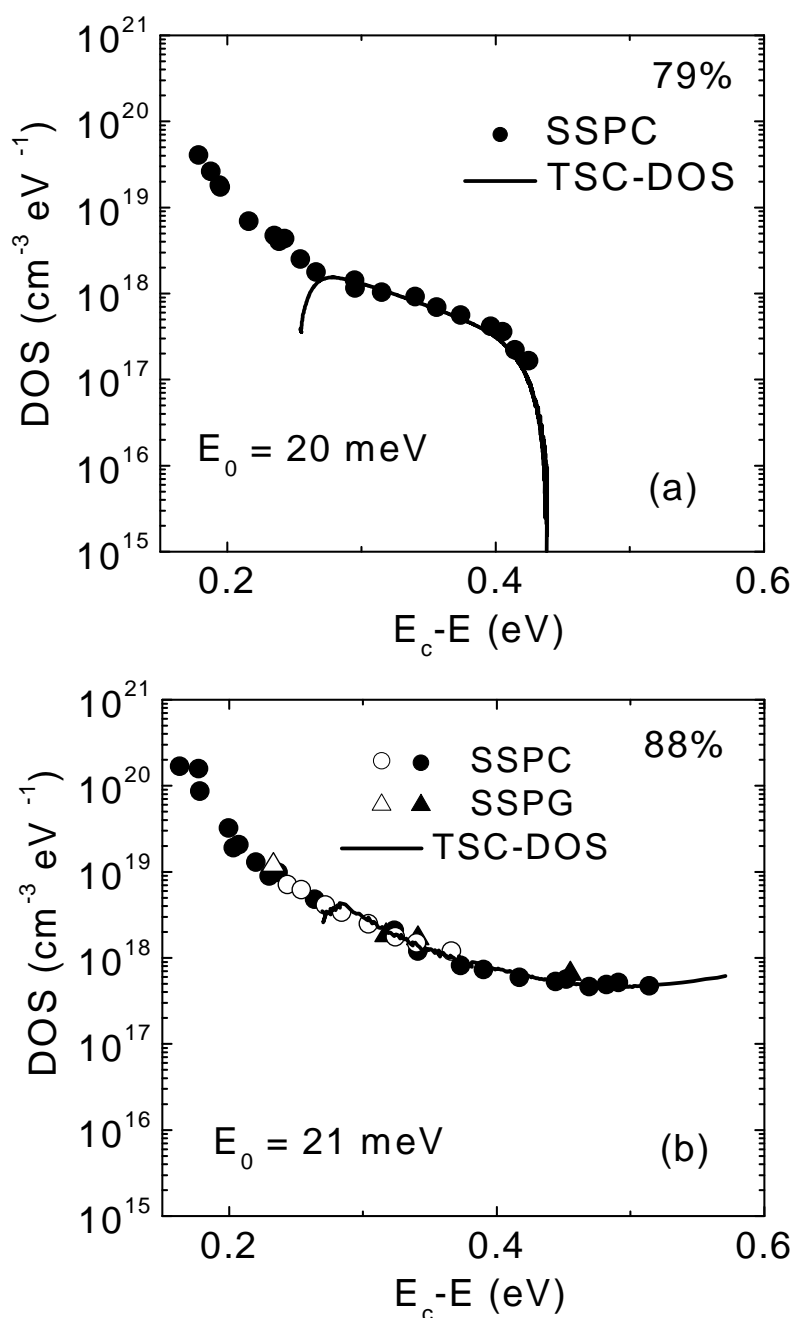


Figure 9.3: Density of states from TSC (full line), and SSPC (symbols) measurements for the sample with $R_c = 79\%$. SSPC is performed at temperature between 96 K and 296 K. The conduction band tail parameter $E_0 = 20$ meV (a). DOS from TSC (full line), SSPC and SSPG (symbols) measurements performed on the sample with $R_c = 88\%$ at the temperatures between 90 K and 296 K. Open symbols represent DOS data at $T = 140$ K. The band tail parameter $E_0 = 21$ meV (b).

Figure 9.3(a) displays the experimental DOS from TSC (full line) and SSPC (symbols) of the sample with $R_c = 79\%$. We recall that for this sample, described with strong retrapping regime, the simulation of experimental data is invariant when c_n (or ν_0) varies between $10^{-9} \text{ cm}^3 \text{ s}^{-1}$ and $10^{-8} \text{ cm}^3 \text{ s}^{-1}$ (see chapter 8). The calibration of SSPC data with TSC measurements is a good method to get the value of c_n for this sample. In this case we found a value of c_n which is around $1.5 \times 10^{-9} \text{ cm}^3 \text{ s}^{-1}$.

Figure 9.3(b) shows the experimental DOS from TSC (full line), SSPC and SSPG (symbols) of the sample with $R_c = 88\%$. Data of DOS from SSPC and SSPG measurements are adjusted here also with the DOS data from TSC for a capture coefficient c_n is obtained around $1.5 \times 10^{-9} \text{ cm}^3 \text{ s}^{-1}$.

9.2.1 Discussion

The first important observation of the results is that, for samples with $R_c = 34\%$, 79% , and 88% , the calibration of DOS data from SSPC and SSPG with the corresponding TSC converge to the same capture coefficient value c_n (or ν_0) which lies in an interval between 1 and $3 \times 10^{-9} \text{ cm}^3 \text{ s}^{-1}$. Consequently, a capture cross section σ_n such that $c_n = \nu_n \sigma_n$ (ν_n represents the electron velocity $\approx 10^7 \text{ cm/s}$) is around 10^{-16} cm^2 .

Figure 9.4 summarizes the results of the DOS from TSC and photoconductivity measurements for all samples.

The Figure reveals a high DOS over the range of energies between $E_c - E = 0.3 \text{ eV}$ and $E_c - E = 0.58 \text{ eV}$ in highly crystalline material (open symbol). However over the range between $E_c - E = 0.15 \text{ eV}$ and $E_c - E = 0.3 \text{ eV}$, the DOS is lower with respect to the samples with lower R_c (full symbol). In addition, for all samples, the profiles of the DOS emerge with a conduction band tail parameter which is between 20 meV and 23 meV .

The high DOS for the samples with high crystalline volume fraction has been reported in the literature by applying ESR measurements on microcrystalline samples [9]. For the samples with low R_c , a decrease of ESR signal is detected. Indeed, the additional amorphous silicon in the sample acts as a passivation layer leading to low defect density [35] (see chapter 2). However a high porosity is attributed to the sample with high R_c .

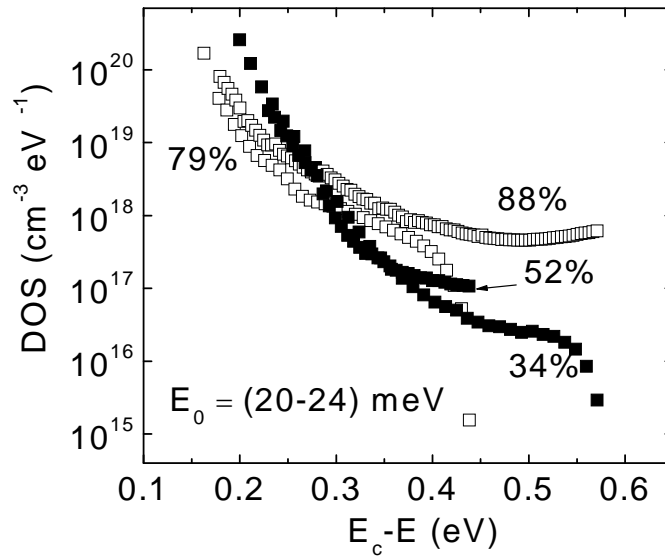


Figure 9.4: DOS for the all samples with different R_c (34%, 52%, 79% and 88%) from TSC and photoconductivity measurements. Open symbol represents the samples with $R_c = 79%$ and 88%, while full symbol represents the samples with $R_c = 34%$ and 52%. A conduction band tail parameter between 20 meV and 24 meV is determined.

9.3 Conclusion

Microcrystalline samples have been extensively investigated by photoconductivity and essentially by TSC measurements upon change of crystalline volume fraction R_c between 34 % and 88 %. A profile of the DOS in the upper half of the gap is determined for different samples. The trap parameters such as capture coefficient and conduction band tail parameter are obtained. In addition a low defect density for $E_c - E > 0.3$ eV is obtained for the sample with low $R_c = 34$ %. However for the sample with high R_c , a high DOS is detected indicating the presence of high porosity.

Chapter 10

Summary and conclusion

This work presents a study of the determination of the density of states (DOS) from experimental and numerically simulated thermally stimulated currents (TSC). Taking into account recombination, thermal emission and trapping, the numerical simulation has been applied in order to analyze the strong and weak retrapping regimes of TSC. The reconstruction of DOS distributions reveals that standard procedures to calculate the DOS from the TSC and mobility-lifetime products are robust in the case of weak retrapping. However in the case of strong retrapping, it has been shown that the quasi Fermi level $E_c - E_q$ is a suitable parameter to establish the energy scale determining the TSC-DOS. The condition $\sigma_{TSC} = \sigma_d$ proposed by Fritzsche to get the effective attempt-to-escape ν_{eff} values has been verified. However, from the simulation the exploitation of the range $\sigma_{TSC} \ll \sigma_d$ has been proposed in order to obtain ν_{eff} values in the case of the weak retrapping regime. Further, ν_{eff} has been quantified, which allows to estimate the retrapping time.

TSC measurements have been applied on microcrystalline silicon ($\mu\text{c-Si:H}$) samples characterised with high and low crystalline volume fraction R_c . The combined experiment - simulation approach allowed to provide evidence of the strong and weak retrapping regimes and also to extract the DOS profile. In this approach, the TSC-DOS is usually calculated with a trial values for ν_{eff} in the equation for $E_c - E_m(T)$. The input DOS is approximated by TSC-DOS for the simulation, which results in $\sigma_{TSC, sim}$. In a final step the TSC-DOS from $\sigma_{TSC, sim}$ is compared with the TSC-DOS from $\sigma_{TSC, exp}$. The data $\sigma_{TSC, sim}$ are obtained after a number of calculation circles for different values of ν_{eff} and ν_0 . TSC conductivity for the sample with $R_c = 34\%$, is related to the weak retrapping regime, while for the sample with $R_c = 79\%$ a strong retrapping regime is obtained.

Taking into account the results of DOS from TSC and also from additional photoconductivity measurements carried out on the samples, profiles of the DOS are determined. These profiles emerge with a conduction band tail parameter varying between 20 meV and 24 meV. A capture coefficient of the samples is between 1 and $3 \times 10^{-9} \text{ cm}^3 \text{ s}^{-1}$. A high DOS, over the range $E_c - E > 0.3 \text{ eV}$, is observed for highly crystalline samples with respect to the samples with low crystalline volume fraction, while over the range $E_c - E < 0.3$

eV, the DOS is lower.

Interesting results have been obtained from the variation of experimental parameters. It has been shown that the DOS does not reveal any variation in the exploited experimental parameter space. This result is consistent because the TSC-DOS must not be change against the experimental parameters. In addition, TSC measurements show that the peak of the TSC-DOS at low energy is not a real image of the DOS. Further, the initial rise of TSC at low temperature has been examined. It has been demonstrated that the origin of this peak is related to the shallow states in the conduction band tail distribution, which are partly occupied.

Furthermore, the photoconductivity measurements indicate that the mobility lifetime product $(\mu\tau)_n$ at room temperature changes with increasing R_c . The Fermi level shifts toward the conduction band edge. This has been related to the change of the occupancy of defect in the gap. Because of the high $(\mu\tau)_n$ values of the sample with $R_c = 79\%$, one expects better electronics properties. The TSC measurements show that this is not always true via the TSC-DOS determination because, as has been mentioned, a high density of states is measured for $E_c - E > 0.3$ eV. The high DOS in this range is attributed to a high porosity of the sample.

In conclusion the profiles of DOS for samples with different crystalline volume fraction have been determined. The evidence of strong and weak retrapping regime has been provided using a combined experiment - simulation approach of TSC. Also the features of TSC at low temperature have been examined.

Acknowledgments

I would like to thank Prof. G. H. Bauer, who accepted me in his research group and gave me the opportunity to effectuate my thesis. His advises and comments greatly helped me in my scientific life.

My particular thanks go to my supervisor Dr. R. Brüggemann, for his attention and patience. I learned various things from him especially in the beginning of this work. I gratefully acknowledge his support in the discussion of ideas and results, which largely contributed to the success of this work.

I would like to thank Prof. Dr. W. Tuszynski, who accepted to read and comment the manuscript.

I am grateful to Prof. C. Main who allowed me to use his TSC simulation. I really appreciated the numerous discussions we had together in Dundee (Scotland) about TSC simulation.

I wish to thank L. Gütay for reading and correcting the abstract in German language. I also think him for the good time we had together and for his good sense of humour.

I would like to thank Dr. F. Voigt for reading and correcting the manuscript. I found very interesting discussions with him, either about thermally stimulated current or about steady state photocurrier grating or also about photoluminescence.

I especially thank E. Bakenhus for her contribution to solve various administrative problems. I also thank her for offering her friendship to me. I would like to extent my thanks to P. Pargmann to solve various technique problems when I was doing the measurements.

I thank all my colleagues from GRECO: S. Meier, S. Burdorf, J. Behrends, T. Jürgens, M. Struß and R. Fuhrmann.

References

- [1] M. A. Green *et al.*, Progress in Photovoltaics Research and Applications **10**, 55 (2002).
- [2] R.E.I. Schropp, Thin Solid Films **451-452**, 455 (2004).
- [3] H. Keppner *et al.*, Appl. Phys. A **69**, 169 (1999).
- [4] D. L. Staebler and C. R. Wronski, Appl. Phys. Lett. **31(4)**, L292 (1977).
- [5] M. Faraji, S. Gokhale, S. M. Choudari, and M. G. Takwale, Appl. Phys. Lett. **60**, 3289 (1992).
- [6] J. Meier, R. Flückiger, H. Keppner, and A. Sah, Appl. Phys. Lett. **65**, 860 (1994).
- [7] J. Meier *et al.*, Thin Solid Films **451-452**, 518 (2004).
- [8] A. Shah *et al.*, Thin Solid Films **403-404**, 179 (2002).
- [9] F. Finger *et al.*, Appl. Phys. Lett. **65**, 2588 (1994).
- [10] S. Klein, F. Finger, and R. Carius, J. Appl. Phys. **98**, 024905 (2005).
- [11] T. Takagi, M. Ueda, N. Ito, Y. Watabe and M. Kondo, Jpn. J. Appl. Phys. **45**, 5A 4003 (2006).
- [12] S. Veprek and V. Marecek, Solid-State Electron. **11**, 683 (1986).
- [13] S. Veprek *et al.*, J. Phys. C: Solid State Phys. **16**, 6241 (1983).
- [14] J. E. Gerbi and J. R. Abelson, J. Appl. Phys. **89**, 1463 (2000).
- [15] J. Guillet *et al.*, Mat. Sc. Ener. B **69**, 284 (2000).
- [16] J. Kocka *et al.*, Solar energy Materials and solar cells **66**, 61 (2000).
- [17] T. Matsui, M. Kondo and A. Matsuda, Mater. Res. Soc. Symp. Proc. **A. 4** 8.1 (2004)
- [18] M. Kondo *et al.*, J. Non-Cryst. Solids, **269-302**, 108 (2002).
- [19] J. Kocka *et al.*, Phys. Stat. Sol. (c) **1**, 1097 (2004).
- [20] P. Torres *et al.*, Appl. Phys. Lett **69**, 13738 (1996)
- [21] F. Liu *et al.*, Thin Solid Films **395**, 97 (2001).
- [22] F. Finger *et al.*, IEE Proc. Circ. Devices Syst. **150**, 300 (2003).
- [23] T. Dylla *et al.*, Mater. Res. Soc. Symp. Proc. **762**, A2.5.1 (2003).
- [24] F. Finger *et al.*, J. Optoelectron. Adv. Mater. **7**, 83 (2005).
- [25] S. Reynolds *et al.*, Mater. Res. Soc. Symp. Proc. **762**, A4.3.1 (2003).
- [26] S. Reynolds *et al.*, Mater. Res. Soc. Symp. Proc. **861**, A5.6.1 (2005).
- [27] S. K. Persheyev *et al.*, Mater. Res. Soc. Symp. Proc. **808**, A9.10.1 (2004).
- [28] N. Souffi, G.H. Bauer, and R. Brüggemann, Thin Solid Films **501**, 129 (2006).
- [29] F. Finger, J. Müller, C. Malten, R. Carius and H. Wagner, J. Non-Cryst. Solids **266-269** 511 (2000).

- [30] J.G. Simmons, G.W. Taylor, and M.C. Tam, Phys. Rev. B. **7**, 3714 (1973).
- [31] H. Fritzsche and N. Ibaraki, Philos. Mag. B **52**, 299 (1985).
- [32] M. Zhu and H. Fritzsche, Philos. Mag. B **53**, 41 (1986).
- [33] N. Souffi, G.H. Bauer, and R. Brüggemann, J. Non-Cryst. Solids **352**, 1109 (2006).
- [34] C. Main, Z. Aneva, S. Reynolds, N. Souffi, D. Nesheva and R. Brüggemann, J. Optoelectron. Adv. Mater. **9**, 114 (2007).
- [35] F. Finger, S. Klein, T. Dylla, A. L. Baia Neto, O. Vetterel and R. Carius, Mater. Res. Soc. Symp. Proc. **715**, A16.3.1 (2002).
- [36] N. Wyrsh *et al.*, J. Non-Cryst. Solids **299-302**, 390 (2002).
- [37] F. Liu *et al.*, J. Non-Cryst. Solids, **299-302**, 385 (2002).
- [38] M. Vanecek *et al.*, J. Non-Cryst. Solids, **227-230**, 967 (1998).
- [39] V. Svrcek *et al.*, J. Appl. Phys. **89**, 1800 (2001).
- [40] S. Okur, M. Günes and O. Göktas, J. Material science **15**, 187 (2004).
- [41] R. Brüggemann *et al.*, Thin Solid Films **403-404**, 30 (2002).
- [42] M. Goerlitzer *et al.*, J. Appl. Phys. **80**, 5111 (1996).
- [43] C. Droz *et al.*, J. Non-Cryst. Solids **266-269**, 319 (2000).
- [44] C. Droz, „Thin film microcrystalline silicon layers and solar cells: Microstructure and electrical perforamnces”, PhD thesis, Université de Neuchâtel p. 35 (2003).
- [45] R. A. Street, ‘Hydrogenated amorphous silicon’, Cambridge University Press, Cambridge chapter 2 p. 42 (1991).
- [46] C. Smit *et al.*, J. Appl. Phys. **94**, 5111 (1996).
- [47] L. Houben, M. Luysberg, P. Hapke, R. Carius, F. Finger, and H. Wagner, Philos. Mag. A **77**, 1447 (1998).
- [48] R. Carius *et al.*, Mater. Res. Soc. Symp. Proc. **467**, 283 (1997).
- [49] R. Carius *et al.*, J. Material science: Materials in Electronics **14**, 625 (2003).
- [50] Z. Iqbal *et al.*, J. Phys. C: Solid State Phys. **16**, 2005 (1983)
- [51] F. Diehl *et al.*, J. Appl. Phys. **84**, 3416 (1998).
- [52] Warren B. Jackson, N. M. Johnson and D. K. Biegelsen, Appl. Phys. Lett. **43**, 195 (1983).
- [53] A. K. Sinha and S. C. Agarwal, Philos. Mag. B **77**, 945-957 (1998).
- [54] B. T. Tiedje, J. M. Cebulka, D. L. Morel and B. Abeles, Phys. Rev. Lett. **46**, 1425 (1981).
- [55] F. Finger *et al.*, J. Materials Science: Materials in Electronics **14**, 621 (2003).

- [56] T. Merdzhanova, „Microcrystalline silicon films and solar cells investigated by photoluminescence spectroscopy”, PhD thesis, Forschungszentrum Jülich (2005).
- [57] R. Brüggemann, *J. Appl. Phys.* **92**, 2540 (2002).
- [58] J. Werner and M. Peisl, *Phys. Rev.* **31**, 6881 (1985).
- [59] R. Brüggemann and O. Kunz, *Phys. Stat. Sol. (b)* **234**, R16 (2002).
- [60] T. Dylla and F. Finger, *Appl. Phys. Lett.* **87**, 032103 (2005).
- [61] D. Azulay, I. Balberg, V. Chu, J. P. Conde and O. Millo, *Phys. Rev. B* **71**, 113304 (2005).
- [62] R. Brüggemann, J. P. Kleider, C. Longeaud, D. Mancaraglia, J. Guillet, J. E. Bourée and C. Niikura, *J. Non-Cryst. Solids* **266-269**, 3582 (2003).
- [63] D. Ritter, E. Zeldov and K. Weiser, *Appl. Phys. Lett.* **49**, 791 (1986).
- [64] D. Ritter, E. Zeldov and K. Weiser, *J. Appl. Phys.* **62**, 4563 (1987).
- [65] D. Ritter, E. Zeldov and K. Weiser, *Phys. Rev. B* **38**, 8296 (1988).
- [66] I. Balberg, K. A. Epstein and D. Ritter, *Appl. Phys. Lett.* **54**, 2461 (1989).
- [67] C. D. Abel and G. H. Bauer, *Prog. Photovoltaics* **1**, 269 (1993).
- [68] M. Hack, S. Guha and M. Shur, *Phys. Rev. B* **30**, 6991 (1984).
- [69] C. Main *et al.*, *J. Non-Cryst. Solids* **198-200**, 263 (1996).
- [70] R. Brüggemann and C. Main, *Phys. Rev. B* **57**, R 15080 (1998).
- [71] A. Vomvas and H. Fritzsche, *J. Non-Cryst. Solids* **97-98**, 823 (1987).
- [72] R.R. Haering and E.N. Adams, *Phys. Rev* **117**, 451 (1960).
- [73] K.H. Nicholas and J. Woods, *J. Appl. Phys.* **15**, 783 (1964).
- [74] P.S. Pickard and M.V. Davis, *J. Appl. Phys.* **41**, 2636 (1970).
- [75] P. Bräunlich and P. Kelly, *Phys. Rev. B* **1**, 1596 (1970).
- [76] G.A. Dussel and R.H. Bube, *Phys. Rev.* **155**, 764 (1967).
- [77] R. Chen, *J. Appl. Phys.* **40**, 570 (1968).
- [78] R. Chen, *Brit. J. Appl. Phys.* **2**, 371 (1969).
- [79] P. Kelly, M. Laubitz and P. Bräunlich, *Phys. Rev. B* **4**, 1960 (1971).
- [80] T. A. T. Cowell and J. Woods, *Brit. J. Appl. Phys.* **18**, 1045 (1967).
- [81] P. Bräunlich, *Thermally Stimulated Relaxation in Solids* (Springer, Berlin); (1979).
- [82] J.G. Simmons and G.W. Taylor, *Phys. Rev. B.* **4**, 502 (1971).
- [83] J.G. Simmons and M.C. Tam, *Phys. Rev. B* **7**, 3706 (1973).
- [84] J.G. Simmons, G.W. Taylor, *Phys. Rev. B* **5**, 1619 (1972).
- [85] J.G. Simmons, G.W. Taylor, *Phys. Rev. B.* **5**, 553 (1972).
- [86] N. Ibaraki and H. Fritzsche *J. Non-Cryst. Solids* **66**, 231 (1984).

-
- [87] M. Zhu, *Appl. Phys. A* **52**, 285 (1991).
- [88] M. Zhu *et al.*, *J. Non-Cryst. Solids* **137-138**, 355 (1991).
- [89] M. Zhu *et al.*, *Mater. Res. Soc. Symp. Proc.* **336**, 449 (1994).
- [90] S. C. Agarwal and H. Fritzsche, *Phys. Rev. B.* **10**, 4351 (1974).
- [91] J.H. Zhou and S.R. Elliott, *Phys. Rev. B* **46**, 9792 (1992).
- [92] S. Özdemir *et al.*, *Meas. Sci. Technol.* **4**, 293 (1992)
- [93] A. Tabata *et al.*, *Appl. Phys.* **22**, 794 (1989).
- [94] X. Zhengyi *et al.*, *Commun. In Theor. Phys.* **10**, 281 (1988) .
- [95] S. W. S. McKeever *et al.*, *Appl. Phys.* **8**, 1520 (1975).
- [96] D.S. Misra, V.A. Singh, and S.C. Agarwal, *Phys. Rev.* **B 32**, 1047 (1985).
- [97] D.S. Misra, V.A. Singh, and S.C. Agarwal, *Phys. Rev.* **B 32**, 4052 (1985).
- [98] G. Landweer, and J. Bezemer, in *Amorphous silicon and related materials*, edited by H. Fritzsche, (World Scientific, Singapore, 1989) Vol. A, p. 525.
- [99] B. Gu, Z. Xu, and B. Dong, *J. Non-Cryst. Solids* **97-98**, 479 (1987).
- [100] S.D. Baranovskii, M. Zhu, T. Faber, F. Hansel, P. Thomas, and G. J. Adriaenssens, *Phys. Status Solidi (b)* **205**, 91 (1998).
- [101] S.D. Baranovskii, M. Zhu, and P. Thomas, *Phys. Rev.* **B 55**, 16226 (1997).
- [102] T. Smail, M. Aoucher, and T. Mohammed-Brahim, *J. Non-Cryst. Solids* **266-269**, 376 (2000).
- [103] J. A. Schmidt, R.R. Koropecski, R. Arce, A. Dussan, and R.H. Buitrago, *J. Non-Cryst. Solids* **338-340**, 322 (2004).
- [104] C. Main, N. Souffi, S. Reynolds, and R. Brüggemann, *J. Non-Cryst. Solids* **352**, 1028 (2006).
- [105] C. Main, N. Souffi, S. Reynolds, Z. Aneva, R. Brüggemann, and M. J. Rose, *Mater. Res. Soc. Symp. Proc.* **910**, A9.2 (2006).
- [106] J. Z. Liu and S. Wagner, *Phys. Rev. B* **39**, 11156 (1989).
- [107] J. A. Schmidt and C. Longeaud, *Appl. Phys. Lett.* **85**, 4412 (2004).
- [108] J. P. Kleider, C. Longeaud and M. E. Gueunier, *Phys. Status Solidi C* **1**, 1208 (2004).

Publications related to the PhD Thesis

1. "Density of states in the gap of microcrystalline silicon determined from thermally stimulated currents"
N. Souffi, G.H. Bauer, C. Main, S. Reynolds, and R. Brüggemann. It has been accepted by Thin Solid Films.
2. "Density of states in microcrystalline silicon from thermally stimulated conductivity"
N. Souffi, G.H. Bauer, and R. Brüggemann, **J. Non-Cryst. Solids** 352, 1109 (2006).
3. "Study of metastabilities in microcrystalline silicon films by photoconductivity techniques"
N. Souffi, G.H. Bauer, and R. Brüggemann, **Thin Solid Films** 501, 129 (2006).
4. "Metastable dark and photoconductivity properties of microcrystalline silicon"
R. Brüggemann and N. Souffi, **J. Non-Cryst. Solids** 352, 1079 (2006).
5. "Numerical modeling of thermally-stimulated currents for the density-of-states determination in thin-film semiconductors"
C. Main, N. Souffi, S. Reynolds, and R. Brüggemann, **J. Non-Cryst. Solids** 352, 1028 (2006).
6. "Thermally-stimulated currents in thin-film semiconductors: Analysis and Modeling"
C. Main, N. Souffi, S. Reynolds, Z. Aneva, R. Brüggemann, and M. J. Rose, **Mater. Res. Soc. Symp. Proc.** 910, A9.2 (2006).

LEBENS LAUF

Name : SOUFFI

Vorname: Nacéra

Geburtsdatum: 25. 03. 1969

Geburtsort: Oran, Algerien

Schulische Ausbildung

09/1975-07/1982 Oran; Algerie, Grundschule

09/1982-07/1988 Lycée Maraval Oran, Gymnasium, **Option:** Mathematik

Abschluss : **Abitur**

Hochschulstudium

09/1988-06/1994 Universität Oran, Fächer: Physik, Mathematik, Chemie

Abschluss: **Diploma of Higher Studies (DES)**. **Option:**Theoretische Physik

09/1994-07/1995 Dozentin an der Universität Oran, Fächer: Optik und Mechanik

09/1995-07/1996 Universität Oran, Algerien

Abschluss: **Postgraduierung: Qualifikation für Zulassung zum Magister**

09/1996-09/1998 Universität Oran, Algerie

Vorbereitung **Magister Diplom (als Diplom Arbeit in deutscher skala)** mit dem Titel
„**Effet de la Metastabilité sur les propriétés optoelectroniques du silicium amorphe Hydrogéné**“

10/1998-12/1999 Universität: **Picardie Jules Verne France (Amiens) Laboratoire de la Matière Condensée, wissenschaftlicher Aufenthalt.**

Abschluss: **A Master Diplom (als Diplom Arbeit in deutscher Skala)** in Physik: **Sehr gut**

12/1999-07/2001 Dozentin an der Universität Oran

01/2002-05/2003 Dozentin an der Universität Oran, Fach: Optik

1/06/2003-30/09/2003: **Sprachkurs (Intensivkurs)**, Carl Duisberg Zentrum, **Dortmund (Deutschland)**

1/10/2003-bis heute Universität Oldenburg Deutschland

Doktorandin in Oldenburg, Arbeitstitel der geplanten Doktorarbeit

„**Thermally stimulated currents and photoconductivity in microcrystalline silicon**“

Hiermit bestätige ich, dass ich die vorliegende Arbeit selbständig verfasst habe und nur die angegebenen Hilfsmittel verwendet habe.